DTU Wind

Modelling of floating wind turbine for model predictive control applications to investigate turbine performance and aero-servo-hydro-elastic instabilities

Carlos Pérez Moreno

DTU Wind-M-0612

August 2023

Author: Carlos Pérez Moreno

Title:
Modelling of floating wind turbine for model predictive control applications to investigate turbine performance and aero-servo-hydro-elastic instabilities

DTU Wind-M-0612
August 2023

Project period:
November 2022 - August 2023

ECTS: 45

Education: Master of Science

Supervisor(s):

Fanzhong Meng
Alan Wai Hou Lio
DTU Wind and Energy Systems

Jan-Willem van Wingerden
Atindriyo Pamososuryo
TU Delft

Remarks:
This report is submitted as partial fulfillment of the requirements for graduation in the above education at the Technical University of Denmark.

Technical University of Denmark
Department of Wind and Energy
Systems Frederiksborgvej 399
DK-4000 Roskilde
www.wind.dtu.dk

Technical University of Denmark
DTU Wind and Energy Systems

DTU Lyngby Campus
Nils Koppels Alle
Building 403
2800 Kgs. Lyngby, Denmark
Phone +45 45 25 25 25
reception@windenergy.dtu.dk
www.windenergy.dtu.dk

Delft University of Technology
Faculty of Aerospace Engineering

TUD Campus
Kluyverweg 1
2629 HS Delft, Netherlands
+31 (0)15 27 85170
DUWIND@tudelft.nl
https://www.tudelft.nl/duwind/

Abstract

FOWTs pose several control challenges. This work addresses reduced order modelling of FOWT to develop an MPC. They key objective is tackle the platform pitch instability while improving the performance in other KPIs. An existing reduced order model, which considers platform pitch and surge, and rotor speed DOFs is adapted and extended, with tower flexibility. The models are validated with open and closed-loop simulations in HAWC2, using the IEA-15MW RWT and the WindCrete spar-buoy floater. Based on these models, an ADKF is designed to estimate several unmeasured states and the wind speed. The MPC aims at reducing the platform pitch motion and tracking the reference rotor speed utilising collective blade pitch angle. The proposed holistic weight tuning procedure conveys the use of Pareto fronts and metrics from several relevant KPIs to guarantee an effective trade-off. Results show a major effects of the simulated wind conditions on the optimal tuning, therefore the process should account for realistic met-ocean conditions. The final tuning is compared to the baseline PI controller with torque compensation. Significant improvements are observed in terms of platform motion reduction in surge, pitch and roll, improved power quality, and greatly reduced fatigue and extreme loads on the tower base and shaft, under all simulated wind conditions. Limitations on rotor speed tracking near rated wind speed show that further development could lead to increase performance.

Acknowledgements

I would like to first thank my supervisors for their guidance and support over the course of the thesis. From the Technical University of Denmark, I would like to thank senior researcher Fanzhong Meng and researcher Alan Wai Hou Lio. From Delft University of Technology, I would like to thank Professor Jan-Willem van Wingerden, PhD Candidate Atindriyo Pamososuryo and PhD Candidate Amr Hegazy.

I would like to thank the EWEM programme for the opportunity to pursue this double master degree.

Thank you to Assistant Professor Fabio Pierella, former DTU Assistant Professor Antonio Pegalajar-Jurado, I have learnt a lot about floating wind energy from you.

Thank you to Associate Professor Jenni Rinker, one of the best professors I had.

Thank you to my PEAK Wind colleagues.

I would like to deeply thank all the good friends I made throughout this master programme. Especially Gabi, Josh, Mateo, Sofus and Sowmya.

Finally, I would like to deeply thank my family, who has been always supportive and encouraging throughout my studies. To my sisters Ana and Lara, and to my parents, Miguel-Angel and Carmen.

Nomenclature

The next list describes several symbols that will be later used within the body of the document

Acronyms

ADKF	Augmented Dynamic Kalman Filter
AEP	Annual Energy Production
BRM	Blade-Root Moment
DARE	Discrete Algebraic Riccati Equation
DKF	Dynamic Kalman Filter
DOF	Degree of Freedom
DTU	Denmark Technical University
DTUWEC	DTU Wind Energy Controller
FOWT	Floating Offshore Wind Turbine
FSI	Fluid Structure Interaction
IPBES	Intergovernmental Science-Policy Platform on Biodiversity and Ecosystem Services
IPCC	Intergovernmental Panel on Climate Change
LCoE	Levelised Cost of Energy
LiDAR	Light Detection and Ranging
LTI	Linear-Time Invariant
MIMO	Multiple-Input Multiple-Output controller
MSL	Mean Sea Level (equivalent to Still Water Level)
NREL	National Renewable Energy Laboratory
O&M	Operation and Maintenance
OCP	Optimal Control Problem
OCP	Optimal Control Problem
ODE	Ordinary Differential Equation
QP	Quadratic Program
RHPZ	Right Half Plane Zero
SCADA	Supervisory Control And Data Acquisition
SISO	Single-Input Single-Output controller
SP	Spar-buoy platform
SWL	Still Water Level
TI	Turbulence Intensity
TLP	Tension-Leg Platform

Controller parameters and variables

$\bar{z}$	Reference set-point for output variables
ϕ	Objective function
N	Number of time steps of the receding horizon
Q_z	Weight matrix on reference deviation
z	Output variable

Wind turbine parameters and variables

$\zeta_{t,1}$	Damping tower FA motion 1st mode
α	Generator viscous friction
λ	Tip-speed ratio
ρ_w	Water density

ζ_θ	Damping platform pitch motion 1st mode
a_k	Nacelle motion contribution from pitch and tower FA modes
C_h	Hydrodynamic damping matrix
c_Q	Aerodynamic torque coefficient
d	Disturbances of the system
$D_{p,O}$	Diameter of the spar-buoy platform at the flotation level
f_θ	Natural frequency platform pitch motion 1st mode
$f_{t,1}$	Natural frequency tower FA motion 1st mode
H_h	Hub height
I_{dr}	Drive-train moment of inertia around its rotation axis
$I_{O,p}$	Moment of inertia of the platform around the centre of flotation
k_{moor}	Mooring line linear stiffness constant
M_k	Structural mass matrix of k body
Q_a	Aerodynamic torque
Q_g	Generator torque
u	Inputs of the system
V_∞	Undisturbed wind speed
x	States of the system
x_r	Fore-aft displacement of the rotor (at hub-height)
x_{tt}	Fore-aft displacement of the tower top
y	Measured variables of the system
z	Output variables of the system
z_{cb}	Center of buoyancy
$z_{cg,k}$	Centre of gravity of body k
z_{moor}	Mooring line fairlead vertical position

Contents

List of Figures

List of Tables

CHAPTER 1
Introduction and literature review

> *Human activities, principally through emissions of greenhouse gases, have unequivocally caused global warming, with global surface temperature reaching 1.1°C above 1850-1900 in 2011-2020. Global greenhouse gas emissions have continued to increase, with unequal historical and ongoing contributions arising from unsustainable energy use, land use and land-use change, lifestyles and patterns of consumption and production across regions, between and within countries, and among individuals (high confidence).*, IPCC, 2023 [1]

Climate change, biodiversity loss, and global warming effects are already noticeable worldwide. The primary cause of temperature increase is the emission of greenhouse gases, like carbon dioxide and methane, which change the atmospheric composition and thus affect the global air temperature, as discovered by Eunice Foote back in 1856 [2]. The global economy heavily relies on burning fossil fuels, massive extraction of natural resources, expanding farming and croplands, as well as exploiting the ocean environment through fisheries and shipping routes, as reported by the Intergovernmental Science-Policy Platform on Biodiversity and Ecosystem Services (IPBES) in [3].

The IPBES report reveals concerning findings: 75% of the land surface is significantly altered, 66% of the ocean area experiences increasing cumulative impacts, and over 85% of the wetland areas have been lost. Human activities pose an unprecedented threat to species, pushing them towards global extinction. Without transformative change, negative trends in nature, ecosystem functions, and the contributions of nature to human well-being are projected to persist beyond 2050. The main drivers behind these negative trends are increasing land and sea use changes, exploitation of organisms, and climate change. The last finding mentioned is probably one of the most insightful, as it highlights the need to radically transform our societies, especially the way wealthy populations live and consume resources, to tackle climate change.

Figure 1.1 shows the increase in global annual average temperature during the last century, particularly in the last and current decades. According to the 2018 Special Report by the Intergovernmental Panel on Climate Change (IPCC) [4], the Paris Agreement's 1.5ºC limit for global warming was predicted to be likely reached within the 2030-2050 period based on policies implemented up to that year. However, the current global average temperature increase has already reached about 1.15ºC, according to the World Meteorological Organisation [5], and 1.26ºC according to [6] and the likelihood of surpassing the 1.5ºC limit within the current decade is rapidly increasing [5] due to the lack of necessary policies and actions to reduce global CO2 emissions.

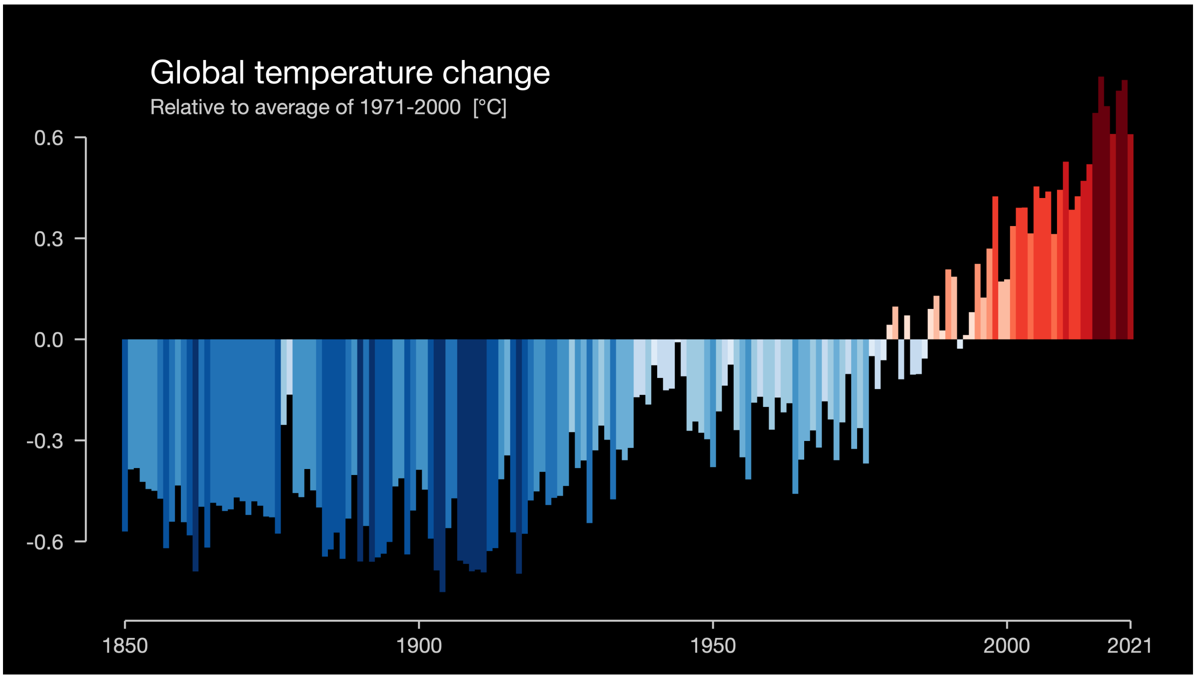

Figure 1.1: Climate stripes representing the global increase in temperature from 1850 to 2021. Reprinted from #ShowYourStripes (`https://showyourstripes.info/s/globe`).

To achieve the transformative change recommended by the IPBES and IPCC reports, society must reduce consumption and transition to renewable energy sources. Significant strides have already been made in addressing electricity generation by increasing the adoption of solar and wind energy.

The global deployment of wind energy has witnessed exponential growth in recent decades. In 2019, the cumulative installed capacity reached 60GW [7], and by 2020, it soared to 93GW despite the challenges posed by the COVID-19 pandemic [8]. The same capacity of 93GW was reported in the IEA Wind TCP Report for 2021, bringing the total global installed capacity to 837GW [9]. Governments worldwide have set even more ambitious targets for wind energy installation, aiming to more than double these numbers by the end of the decade.

As indicated in [7–9], the majority of installed wind capacity is onshore, exceeding 700GW, while offshore capacity reached 57GW in 2021. However, the offshore sector is expected to experience a larger expansion in the coming years due to the maturity of the technology and the availability of vast areas with better wind resource, lower turbulence levels, and reduced environmental and social impact.

The floating wind energy technology review by Ørsted [10] indicates that most European sea areas are ideally suited for floating technology. Countries and regions like France, Spain, Portugal, and Scotland could experience significant development in the near future. For instance, in the Scottish auction of 25GW of offshore wind energy, 14GW were allocated to floating wind farms, making the United Kingdom the leader in floating capacity, with just over 100MW at the time of writing. This illustrates the pressing challenge of rapidly advancing floating wind energy to meet governments' ambitious targets.

Numerous floating wind turbines have been successfully installed since the debut of the first installation, Blue-H (80kW) [11], in 2008. Operating small wind farms include HyWind Scotland, the first floating offshore wind farm with a capacity of 30MW, and WindFloat Atlantic, installed in 2020, with a capacity of 25.2MW. Additionally, HyWind Tampen, being installed in 2022 and 2023, has become the largest floating offshore wind farm, with an 88MW capacity.

Several floater prototypes are currently being tested in both experimental facilities and the ocean. An overview of the most relevant concepts is shown in Figure 1.2a. In Spain, two floating wind facilities, the Biscay Marine Energy Platform (BiMEP) and Oceanic Platform of the Canary Islands (PLOCAN) test facilities. The former is being utilised to test Saitec's semi-submersible 2MW prototype, whereas X1 is testing a novel concept using a single-point mooring line and a wind turbine in a downwind configuration at the Canary Islands test site. Another semi-submersible concept, SAIPEM's HexaFloat, will be first demonstrated at the Site d'Expérimentation en Mer (SEM) pour la Récupération de l'Energie des Vagues (REV) on the French Atlantic coast, where BW Ideol is already testing a barge-type floater. A scaled version of HexaFloat is currently being tested in MaRELab, Italy. These developments showcase the concerted efforts by research institutions and the industry to scale the floating wind industry to meet targets rapidly. However, several challenges remain to be overcome.

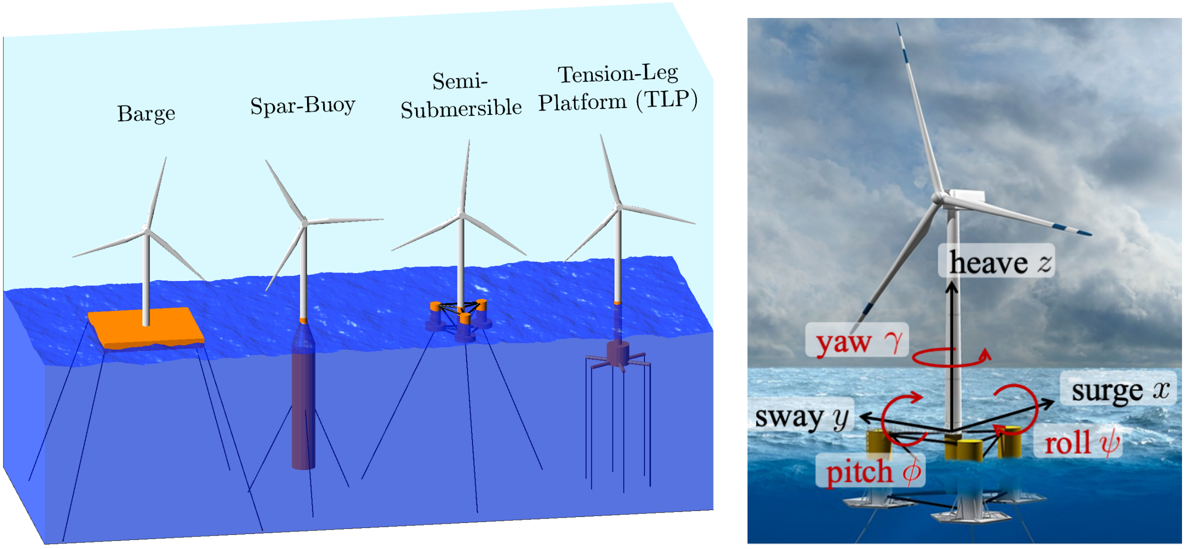

(a) FOWT platform types

(b) FOWT six DOFs

Figure 1.2: Floating offshore wind turbines. In (a), the DOFs of the floating platform are shown and (b) depicts general types of FOWT. Both images reprinted from [12]

1.1 Challenges of floating wind energy

Floating offshore wind turbines (FOWTs) generally face larger extreme loads due to their longer distance from the shore, which exposes them to harsher wind and wave conditions. The uncertainty in met-ocean conditions and their impact on the floating substructure, installation and decommissioning, coupled with the limited technology maturity and the added complexity of the substructure design compared to bottom-fixed solutions, results in an increased Levelised Cost of Energy (LCoE) [13, 14].

Furthermore, generating electricity far from the customers adds challenges to the export system, which is also subject to dynamic loads, in contrast to bottom-fixed offshore cables. Additionally, challenges arise regarding the installation method and the Operation and Maintenance (O&M) strategy.

There exist important challenges, especially regarding the stability of the platform, due to the added degrees of freedom to the system, depicted in Figure 1.2b. Shown in Figure 1.3 is one of the well-known instabilities in floating wind energy affecting the pitch motion of the platform/fore-aft motion of the wind turbine, namely the pitch instability [15, 16]. The source of this instability is the control strategy above rated wind speed, that is, the blade pitching to maintain the rated power level while minimising aerodynamic loads, as it can be seen in the thrust curve Figure 1.3b.

The pitch instability can be visualised intuitively considering a pitch-towards-feather control strategy, Figure 1.3. In this strategy, the blades are pitched in such a way that the angle of attack along the blade decreases. When the wind speed increases, the controller will pitch the blades to keep the rated power level and reduce the thrust. However, this reduction in thrust causes the nacelle to move forward, resulting in an increase in the effective wind speed at the rotor. This, in turn, leads to further pitching and thrust reduction, causing instability in the system.

Furthermore, the platform pitch natural frequency falls within the controller bandwidth for offshore wind turbines, and thus the controller could potentially excite this mode. Especially if the controller is tuned too aggressively. The existence of Right Half Plane Zeros (RHPZs) limits the controller bandwidth, since the poles will migrate towards them as the controller gains increase, and the system will become unstable [16]. To address this issue, a series of solutions have been considered in the literature.

The first approach is to reduce the controller bandwidth [15], this is generally called controller de-tuning, and its main advantage is simplicity, minimising the changes performed in the controller. Another popular method is the use of parallel compensation has been explored in several publications, for instance, [18]. This technique is based on measuring the tower-top motion to reduce it by an additional loop in the controller. Alternatively, adding a control DOF [19] could further reduce the system's motions by means of an active damping system or active ballast control. Switching to pitch-to-stall operation has also been proposed [15], such that the thrust decreases at a slower pace or even increases with the wind speed thanks to the added drag force in the rotor. A summary of these approaches is given in [16].

Most of these solutions present certain limitations. For instance, reducing the controller bandwidth would worsen the power quality, as there would be larger oscillations

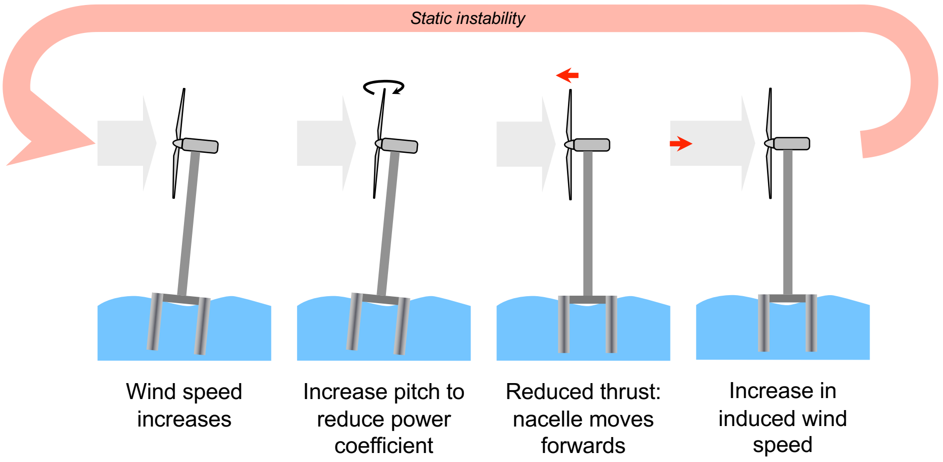

(a) Pitch instability

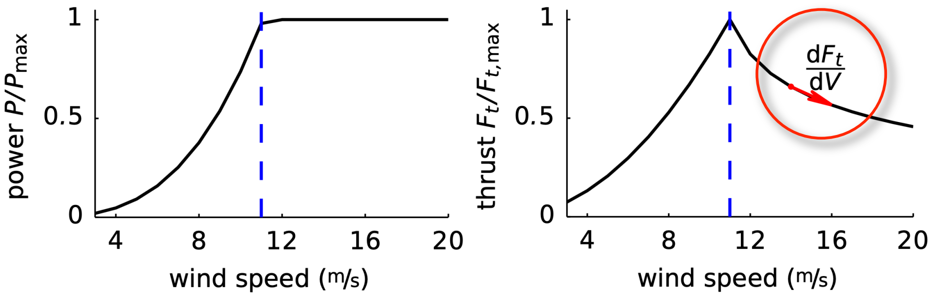

(b) Power and thrust curve of variable-speed pitch-regulated wind turbine

Figure 1.3: Static pitch instability, (a) shows the effect of blade pitch angle in the pitching motion of the platform (b) The negative slope of the thrust curve above rated wind speed is the driver of the pitch-control-induced instability. Reprinted from [17].

in the rotor speed. The gains from parallel compensation are limited, as the system potentially becomes unstable with an increasing gain. The use of an additional degree of freedom means adding extra actuators and, therefore, maintenance complexity, risks and costs. Using pitch-to-stall would increase the loads dramatically due to the large increase of aerodynamic drag on the blades for the above rated operation. Given the constraints associated with each approach, alternative solutions by considering advanced control techniques, such as Model Predictive Control (MPC), are shown in the literature.

Although pitch instability is the most treated in the literature, other aerodynamic instabilities can arise and must be addressed, that is the case of the roll-yaw lock, recently discovered and shown in [20]. This instability occurs at large thrust forces due to the coupling between roll and yaw, it was first observed with hydro-aero-servo-elastic simulations, and it can be captured with low-order models.

These instabilities could be reduced or mitigated both by means of actively considering them during the component design phase (as in the case of roll-yaw lock), generally known as *control co-design*, or by designing a controller able to increase the stability margin. This, as mentioned in [20], could have negative side effects, as the use of pitch control below rated would reduce the power harvested or affect the loads experienced by the system. Thus it is important to consider the trade-offs.

1.2 Model predictive control for wind energy applications

Control strategies for individual wind turbines have significantly evolved over the last years. Originally, simple Proportional-Integral (PI) controllers were used in a Single-Input Single-Output (SISO) manner. This approach assumes the inputs and outputs are not fully coupled. For the full-load region, the rotor speed is controlled using the blade pitch while keeping the generator torque or the power constant. On the other hand, in the partial-load region, the rotor speed is controlled using the generator torque and keeping the pitch angle constant [21]. Over the years, more attention has been given to more robust and model-based control strategies since the wind turbine system would benefit from a Multiple-Input Multiple-Output (MIMO) approach. From this perspective, MPC can play a major role in coupling several objectives, constraints, and the simultaneous control of blade pitch and generator torque, through the definition of an optimization problem. The main principle behind MPC is to solve such an optimization problem over a finite prediction horizon, often referred to as receding horizon, in order to find the optimal control actions that satisfy the constraints and minimise the proposed objective function [22].

Historically, MPC was developed in the process industry. However, it is becoming more popular in other fields, including wind energy. According to [22], the main reasons for the success of MPC as an advanced control technique are (i) its ease in handling multivariable systems, (ii) direct incorporation of constraint definitions, and (iii) the ability to operate close to the aforementioned constraints without violating them, leading to optimum operation. Additionally, the constant increase of computing power allows for the deployment of these control systems.

To design an MPC, it is necessary to have a model capable of representing the system accurately enough while being efficient computationally, such that the trajectory optimisation can be computed in real-time. Additionally, the performance of MPC is dictated by the available information on the disturbances affecting the system, that is, for a FOWT, wind field, wave and, in some cases, sea current.

Therefore, one of the main steps is to develop a low-order model. A number of low-order models have been developed for onshore and bottom-fixed applications; however, developing a low-order model for floating wind turbines represents extra challenges due to the degrees of freedom added by the floating platform, the strong coupling of the platform motions with the rotor response, and the inclusion of the mooring lines. Existing literature in the modelling of FOWT is outlined in subsection 1.2.2.

Compared to the classic PI controller, the application of MPC allows to set certain constraints through the optimisation step, as well as new targets, by including weighted reference terms in the cost function of the controller. Some of these goals can be increasing power quality, reducing fatigue loads, or minimising actuator aggressiveness [23,24]. Such constraints can be set both on inputs and outputs.

The use of these constraints potentially yields significant benefits with respect to the classic PI control, where only the magnitude and rate of change of the inputs could be limited through the addition of saturation outside the PI controller, originating the need for anti-wind-up techniques. With MPC, surpassing the defined thresholds can either be penalised by means of the objective function, generally referred to as soft constraints, or directly limited as a hard constraint when implementing the optimisation algorithm. For instance, it is mentioned in [25] the possible use of constraints on the platform motion to limit loads on the mooring lines or dynamic cables.

The application of MPC presents, however, a number of challenges and requirements, as expressed in the literature,

- an accurate reduced order model of the turbine is needed [23],
- accurate estimation of the states [26],
- low computational effort needed [27],
- accurate estimation of the states or knowledge of the disturbances.

Some of the challenges are clearly coupled. On one hand, a model too simple would likely result in model mismatches, which will affect the controller capabilities, reducing the energy production or not being able to handle instabilities. On the other hand, a model with a large number of degrees of freedom cannot be used in real-time optimisation with the current computation power.

The use of MPC for wind energy applications has been gaining attention over the last few years [28]. In [24], a multiple MPC-based control strategy for the above rated region is presented based on several models for the rotor and generator that are obtained from linearising the low-order non-linear representation of the rotor, shaft and generator using five states. The results showed an improvement regarding the smoothness of the power signal and reduced variations in the pitch angle and shaft torsion, indicating potential gains in the fatigue loads.

In [29], a performance comparison between linear and non-linear MPC (NMPC) is presented, where the controllers are tested alongside with simulated LiDAR measurements to explore the benefits of disturbance preview. NMPC is demonstrated to outperform linear MPC at the expense of higher computation time. The linear MPC algorithm implemented in the comparison considers a single linearised model, whereas the non-linear model is linearised at each prediction step, that is, the optimisation is done using the Local Linearisation on the Trajectory algorithm. This algorithm linearises a non-linear model at each time step of the prediction horizon, enhancing accuracy with respect to linear MPC, at the expense of higher computation effort. Nonetheless, both controllers perform better than the baseline PI controller and show partial improvement due to the provided LiDAR measurements.

While these findings hold significance within the realm of MPC's application to wind turbines, it is important to note that they stem from an onshore wind turbine model. As previously discussed, the complexities inherent to floating offshore wind turbines

(FOWTs) arise from the introduction of extra degrees of freedom and the inherent instability in platform pitch. These factors necessitate their inclusion in the control design process.

1.2.1 FOWT control by MPC

Early work done by Schlipf et al. [30] showed great potential for NMPC applied to FOWTs. The fatigue loads are reduced, as well as the rotor over-speed and power fluctuations, at the expense of significantly larger pitch actuation — a characteristic consistently observed in the literature. Further work was performed in [31], augmenting the NMPC with Individual Pitch Control (IPC) for blade load reduction. However, this addition demonstrates only little to no role in terms of platform motion minimisation.

Enhancements in minimising platform motion are highlighted in [32]. The study utilises a linear MPC formulation with a non-linear model that is linearised based on the operating point prior to solving the optimisation problem. In this investigation, reductions were observed not only in pitch platform motion compared to a baseline PI controller but also in improved power quality and a decrease in the standard deviation of fairlead tension. However, it is important to note that the tower's short-term fatigue load in the fore-aft direction exhibited an increase. Additionally, it's worth mentioning that the newly developed controller was assessed solely under a single combination of wind and sea state: an average wind speed of 18 m/s, 15% turbulence intensity, significant wave height of 6.9 m and peak wave period 7.8 s.

Using the same wind conditions but a reduced significant wave height as [32], [33] showed deteriorating power error when compared to a de-tuned baseline PI controller, while using constant torque approach in the MPC formulation. The generator power overshoots reached 30% of the rated value. On the other hand, significant improvements in tower-base fatigue loads are attained, and only a slight reduction of the flapwise blade-root moment (BRM), despite its inclusion in the objective function, which may indicate the need of IPC for a significant blade load reduction.

The blade load reduction using IPC is explored in [34], showing great improvements thanks to the employment of non-linear MPC together with IPC. However, the rotor speed tracking worsened as compared to a baseline PI controller, and the results presented are limited by not including an state estimator. This example showcases the importance of a holistic trade-off analysis.

In [35], the potential of linear MPC as an integral part of a control co-design process is highlighted. Since the controller plays a major role in the dynamics of FOWTs, consideration during the design process can lead to substantial gains. The linear MPC is developed based on a set of linear systems linearised at different wind speeds. The objectives are set through a cost function considering rotor speed tracking, electrical power maximisation and structural loads minimisation.

The question on the level of disturbance knowledge required to improve the MPC performance for FOWT is addressed in [36]. In this study, a comparison between the use of LiDAR preview with high-frequency SCADA data is shown, concluding that high-frequency SCADA data offers better performance while being more accessible and cost-effective.

The use of MPC for motion reduction has continuously been considered in the literature. The performance has been compared in [37] with a baseline (Gain-Scheduled PI) and an Linear Quadratic Regulator (LQR) controller, showing that especially surge and pitch can be reduced at above rated wind speeds using advanced control techniques, but a further reduction is attained with MPC as compared to LQR. However, this work only considered a single wind speed, 18 m/s.

Significant improvements in rotor speed stabilisation are presented in [38], where a full set of wind conditions covering the operation range were studied. Simulations conducted above the rated wind speed displayed substantial oscillations when governed by a PI baseline controller, which were significantly reduced with the use of MPC. The incorporation of a disturbance previewer, based on a more complex 10-state model, contributed to these outcomes. Additionally, some improvements were observed around rated wind speeds in terms of rotor speed oscillations. These observations suggest that certain limitations inherent to the system design might impose constraints that the controller cannot entirely overcome.

In [25], an economic non-linear MPC is devised to enhance the power production of a floating offshore wind turbine. Economic MPC offers the advantage of formulating the optimization problem in economic objectives, potentially yielding more cost-effective operation. The study introduces constraints not solely in the inputs, such as blade pitch and generator torque, but also in the thrust to alleviate loads on the rotor and tower. Constraints are further applied to power levels to prevent excessive strain on electronic components, the generator temperature, and both surge and pitch velocities, which also mitigates loads on mooring lines and dynamic cables. This formulation yields a modest enhancement in power production below rated power (approximately 1%). Furthermore, it establishes a more stable generator temperature and platform pitch. Notably, the formulation demonstrates a substantial improvement (around 4%) under conditions surpassing the rated capacity.

The explored literature shows great potential for improving the platform motion response, output electrical power and structural loads by using MPC. However, in most cases the disturbance previewers are used, which are not yet in a maturity level that justifies their cost, and the tuning process is not presented. Additionally, comprehensive load analysis for the presented MPC formulations are seldom available, and the performance tends to be explored at a narrow range of wind speeds. This aspect limits the insights regarding the necessary trade-offs when designing and tuning the objective function used by the controller.

1.2.2 Low-order modelling of floating wind turbines

The development of low-order models is a necessary step for the application of MPC, as will be seen in the following sections. However, this is not the only reason to develop such models. As noted in [27,39], simple first-principles-based models can be used for

- achieving an understanding of the physical phenomena,

- implementing novel modifications in the design and perform a quick analysis of their impact,
- testing a controller version or design before validation and verification with higher fidelity models and tools.

Alternatively, higher-order models, such as those that can be obtained from high-fidelity wind turbine aeroelastic analysis tools, such as HAWCStab2 [40] or OpenFAST [41], can be reduced for control design using different techniques, like Hankel singular value decomposition [42], balanced realisation [43], or modal truncation [44].

In [44], modal analysis is applied to a fully flexible wind turbine, including unsteady aerodynamics. The method used contains two steps, first modal basis projection followed by modal truncation of the main states of the system. Balanced truncation is also used and compared with modal truncation. This work highlights the applicability of the order reduction methods used to design gain-scheduled controllers.

In [27], the requirements of a low-order model that can be used both for control design and design optimisation are summarised. The model should capture the system's holistic dynamics without delving into specific mechanic parts (components), ensuring computational efficiency. Furthermore, it should be represented with non-linear equations of motion (EOM) that can be linearised and include only scalar disturbance inputs.

For onshore applications, the control design process has usually been performed using a simple drive-train model equation. However, the development of more advanced control techniques requires the use of more complex models. For instance, in [29], a 3-DOF model is used to design MPC considering the drive-train rotational motion, the tower fore-aft flexibility and the blade pitch actuator dynamics.

Throughout the last few decades, a series of low-order models for floating wind turbines have been presented. A summary is given in Table 1.1. As can be seen, all the models are limited to a number of DOFs below 10 and tend to use the assumption of rigid rotor and tower. This assumption is being challenged by the development of longer blades and taller towers, with increased flexibility and deformations.

Table 1.1: Summary of already developed floating offshore wind turbine models.

Author	**Published year**	**DOFs**	**Main assumptions**	**Novelties**	**Comments**
Henriksen et al. [45]	2010	8	Rigid rotor with dynamic inflow	Aerodynamics with dynamic inflow model	Spar buoy platform
Betti et al. [46]	2012	4	Fully Rigid body	Control-oriented model	Spar buoy platform
Karimirad et al. [47]	2012	-	-	Great reduction in computation time	Validated for spar-buoy type
Sandner F. [23]	2012	9	Rigid rotor	Tower bending in two directions	Spar buoy platform
Betti et al. [39]	2014	4	Fully Rigid body	Control-oriented model	Tension leg platform
Sandner F. [27]	2018	5	Rigid rotor, elastic tower	Applied to optimisation	-
Pustina et al. [25]	2022	6	Rigid rotor with dynamic inflow	Inclusion of generator thermal model	Validated using OpenFAST for the OC3 SparBuoy

The FOWT system can be divided into the following elements,

- Floating substructure, or platform, modelled as a rigid body, ranging from 2 to 6 DOFs. Surge and pitch are consistently used, heave is added to some models, and more extended models use the 6 DOFs. To capture instabilities such as roll-yaw lock, it is necessary to include such DOFs,
- Mooring lines, which are typically considered through a linearised stiffness matrix,
- Tower, included by most publications as part of the floating platform by means of adding its weight and consider it as a rigid body; however, some models take into account its flexibility [23, 27, 35]
- Nacelle, not considered in most cases, however in [23], it is considered through tower top DOFs; additionally, there is drag caused by it,
- Generator, generally coupled using the drive train equation with the rotor aerodynamics by means of the rotor speed DOF,
- Blades, which are considered rigid in the simple models studied, and thus no states associated with them are considered other than the rotor speed, however, blade load alleviation requires the development of a higher accuracy model considering blade flexibility.

In [48], the platform model is developed using 6 degrees-of-freedom, coupled with a Blade Element Momentum (BEM) representation of the rotor, and the model is analysed in order to understand the fatigue load drivers in the different elements of the systems. Although several assumptions are considered, leading to a simplified model not being coupled with the controller, and the stochastic wind component being neglected, it presents a first step in the development of simple accurate models for floating wind turbines.

Following this first work on coupling the hydrodynamic, aerodynamic and structural response of floating wind turbines, important developments are presented in [49, 50]. Further, in [51], a simulation tool for floating wind turbines is presented and validated, which extends the capabilities of NREL aero-servo-elastic code, FAST, by including a hydrodynamics module, HydroDyn. However, the model used is not simple enough for control-oriented purposes, since a very large number of states are considered. Henriksen [45] presents a compendium of papers covering the modelling and estimation of wind and wave-induced loads in his PhD thesis. Amongst them, he developed a simplified linear dynamic inflow model that can be applied in model derivations for control design purposes.

Later on, models were developed to enable fast simulation of floating wind turbines, in [47], a simplified aerodynamic model is applied and coupled with Simo-Riflex, with a relatively accurate response of a Spar-type floating wind turbine system as compared to HAWC2 [40].

Similarly, in [46], a model for control design for a spar-buoy platform (SP) is shown. The model is based on a first-principles approach, considering three DOFs for the platform: surge, heave and pitch, and the rotor speed for the aerodynamic forces on the blades. With the rotor speed, the thrust and power can be calculated as a function of tip-speed ratio, λ, and the collective pitch angle, β, using the rotor performance curves, that is, the thrust coefficient, $c_T(\lambda, \beta)$, and power coefficient, $c_P(\lambda, \beta)$, curves. Then, the forces acting on the tower, nacelle, mooring lines and platform are modelled and combined using Lagrange equations to reach a system of equations. The model is validated against FAST simulations with satisfactory results. The same methodology is applied in [39] for a Tension Leg Platform, with the main changes appearing in the tension mooring line modelling, as compared to the catenary mooring lines of the spar buoy platform.

Slightly earlier, [23] developed a more sophisticated model with 9 degrees of freedom, using the Newton-Euler formalism for a spar buoy platform. In this case, all the degrees of freedom are considered for the platform motion, and two degrees of freedom are added to the tower top in the fore-aft and side-side directions. Finally, a single degree of freedom is used for the rotor, namely the rotor speed. The text covers all the modelling details both for the aerodynamic and hydrodynamic forces and how these are coupled to the structural model.

The same author developed other models to be applied for a semi-submersible platform, with fewer degrees of freedom, in [35] and [27]. This work builds upon the linearisation techniques shown in [52, 53]; however, the work from Lupton is done in the frequency domain, which, as stated in [48], requires linearisation of the important phenomena to be included in the model and less accuracy is achieved. Other examples of frequency-domain models include [54].

A similar model to [23] is presented in [55], with 6 DOFs for the platform and 2 DOFs for the drive train, validated against FAST simulations. This work includes a wave-disturbance matrix, showing great improvements regarding disturbance rejection. This model is applied to a semi-submersible platform.

A simple 3-DOF model is presented in [56], with only the rotor speed, surge and pitch of the platform being considered. This work is a great starting point to understand the modelling process for floating offshore wind turbines, thanks to the simplicity of the presentation, as well as the use of linearisation techniques to obtain the linear system representation.

More recently, in [20], 2-DOF and 6-DOF models are developed to include the roll-yaw lock instability and obtain an analytical equation to calculate such stability margin.

In [56], a 3-DOF model is developed for control applications. Another interesting model is developed in [57], with 6 DOFs and the novel inclusion of a wave disturbance matrix.

Many more first-principles-based models are discussed in the literature, generally with a low number of states. In conclusion, regarding the modelling of floating wind turbines, there is already a great amount of work done to obtain the response of the system and be able to design controllers. However, these models can be further improved by the inclusion of non-linear aerodynamic and hydrodynamic effects while keeping the simplicity and the fast computation time needed for these applications.

1.3 Objectives of the Master thesis

Numerous challenges lie ahead of the wind energy industry, as presented in [58]. This thesis project aims to tackle two of them, within the field of floating offshore wind energy. First, the need for accurate models capable of capturing the complex dynamics impacting power production and loading of the system. Secondly, the development of optimisation-based control systems capable of adapting to energy market fluctuations.

The abundance of existing models in the literature underscores the need to discern the requisite level of fidelity for control design purposes, particularly for MPC synthesis, rather than delving into further, more intricate developments from a control design perspective. Specifically, enhancing the comprehension of how the complexity of the reduced-order model should be adjusted in accordance with the controller's objectives could potentially lead to cost-effective designs.

Furthermore, model developments are frequently presented without the definitive set of equations, and their accuracy often hinges on the specific floating offshore wind turbine (FOWT) under study. Consequently, they require tuning to align the behaviour with the desired level of accuracy. For that purpose, a tool is to be developed facilitating design, implementation and validation of reduced order models.

Moreover, to the knowledge of the author, research outlining the MPC tuning procedure adopted for FOWT applications does not exist, as well as the type of simulations used to optimise the weights and penalties of the objective function. Within the tuning process, numerous research questions emerge, including:

- Which atmospheric conditions should be considered in the tuning process? Does the tuning depend on the wind inflow considered?
- Should the weights and penalties be scheduled with the met-ocean conditions and, consequently, the operating conditions?
- How should an objective function be designed to tackle platform instabilities?

Lastly, the performance evaluation of the MPC rarely encompasses a broad range of wind speeds and the complete spectrum of relevant Key Performance Indicators (KPIs) involved in the design phase, necessary for conducting comprehensive trade-offs. Therefore, the project aims at developing a tool capable of implementation, tuning and load analysis of MPC controllers.

Therefore, the main objectives of the master thesis, as a result of the literature review and the existing gaps of knowledge, are

1. Provide an overview of the existing modelling approaches for each of the elements of the floating offshore wind turbine system,
2. Further develop a reduced order model based on first principles,
3. Validate and verify the model by running simulation experiments using a high-fidelity aero-hydro-servo-elastic tool,
4. Develop an MPC algorithm for tackling the platform pitch instability of a floating wind turbine,

5. Provide a convenient tuning considering the trade-offs between different KPIs.

1.4 Thesis report structure

The thesis report commences by considering the background and context of floating offshore wind turbines. Subsequently, a literature review of the control of FOWTs is provided, with a distinct focus on MPC applications. The subsequent section enumerates the thesis goals.

Chapter 2 offers a concise overview of the modelling of floating wind turbines and introduces three reduced order models. The first model considers a single platform degree of freedom, followed by a model that incorporates both platform pitch and surge degrees of freedom. Lastly, the second model is expanded to include tower fore-aft flexibility. These models are initially presented as a set of non-linear equations, necessitated by the aerodynamic forces. Consequently, a linearisation approach is employed, and the subsequent state-space formulation is presented.

Chapter 3 outlines the FOWT under analysis, featuring the WindCrete Spar-buoy concept coupled with a 15MW reference wind turbine. Various approaches for obtaining the model parameters are examined. Additionally, a sensitivity analysis on the linearised aerodynamic forces is provided. Finally, the linear models derived in the preceding chapter are validated against HAWC2 simulations using the computed model parameters. The accuracy of the models is assessed through modal analysis, open-loop and closed-loop (feedback PI control) simulations.

In chapter 4, the design of classic PI controllers for wind turbine applications is reviewed in the context of FOWT. The parallel compensation approach is outlined, and the tuning procedure is presented.

Subsequently, chapter 5, delves into the implementation of the linear model predictive controller, encompassing observer design and validation, as well as the formulation of the regulation problem. The mathematical formulation is followed by an in-depth exploration of the tuning procedure, with detailed explanations of the considered trade-offs.

Chapter 6 presents the most pertinent outcomes of a load analysis comparison between the linear MPC developed in the preceding chapter and the baseline PI controller. The focus is directed towards operational parameters, platform motions, and selected load channels, to investigate fluctuations, fatigue, and extreme loads.

Finally, chapter 7 engages in a comprehensive discussion of the thesis findings, delving into both the achievements and potential limitations of the linear MPC approach.

CHAPTER 2

Modelling of Floating Offshore Wind Turbines

A number of models are available to study the hydro-aero-servo-elastic response of floating offshore wind turbines. Some of the first work was developed at the National Renewable Energy Laboratory (NREL) in the United States and is presented in [49–51], currently available as OpenFAST [41]. Other simulation tools can be used to analyse FOWT, such as HAWC2 [40, 59], developed at Technical University of Denmark (DTU). These tools constitute mid-fidelity tools, as they present a large number of degrees of freedom of the system. Higher fidelity simulations can be obtained using Computational Fluid Dynamics coupled with Fluid-Structure Interaction, as done in [60], where HAWC2 was coupled with Ellypsis3D [61–64].

For the present work, such a high level of complexity is deemed unnecessary for the current control design purposes. In order to overcome these difficulties, reduced-order models of wind turbine generators have been derived in the literature. In this chapter, two reduced-order models for a floating wind turbine are shown, and an extension is derived.

2.1 On the necessary model fidelity

Most of the models typically used for control design purposes in wind energy present few degrees of freedom, mainly the generator model with steady aerodynamics, which, according to [25], is not able to capture accurately certain phenomena, such as the unsteady aerodynamic loads.

According to [44], *the transfer function from collective pitch to the generator speed is affected by two low-frequency non-minimum phase zeros. To correctly predict the non-minimum phase zeros, it is shown to be essential to include lateral tower (side-side) and blade flap degrees of freedom.* Therefore, these DOFs should be included in the model when dealing with side-side motions. They might not be important, however, when dealing with fore-aft motions and the platform pitch instability explored later on.

Regarding the platform, it is mentioned in [50] that all six DOFs should be included, including the yaw motion, due to the coupling of this motion with the aerodynamic loading when the rotor is not aligned with the wind direction and the induced gyroscopic yaw moment (by spinning inertia combined with pitching motion of platform and/or tower deflection).

Therefore, it is common to see the floating substructure being modelled as a rigid body, with six DOFs [20, 23, 27], although some authors used only two or three DOFs with satisfactory results [39]. The rigid body assumption is used in most hydro-aero-elastic codes known by the author, as the materials used for the platform tend to be concrete or steel (presenting a very large stiffness), and no slender elements like braces are included in the model for simplicity.

The work done in [34] showed performance improvements in rotor speed tracking and blade-root and tower-base moments when considering a non-linear model during the control design phase, however, the platform pitch and roll showed larger motions as compared to a linearized model, meaning that a simple linear model may be sufficient to tackle the platform pitch instability consider in this work. Therefore, satisfactory results can be expected by assuming linear aerodynamic forces acting on a simplified rotor.

To summarise, this work consider four DOFs, namely platform pitch and surge, rotor speed, and tower-top fore-aft deflection.

2.2 How to derive a model?

Different techniques can be used to derive a reduced-order model. The model in [20] is derived from the equations of motion of a spring-damper system applied to a floating rigid-body, with a series of assumptions and analytical expressions for the external aerodynamic forces. Notably, these assumptions include the thrust force acting perpendicular to the rotor plane and the platform's angular displacements being sufficiently small to enable the use of the small angle approximation, allowing to represent the aerodynamic forces as an stiffness term in the platform's equations of motion.

On the other hand, the model used in [25] for the platform dynamics is obtained through system identification from mid-fidelity simulations in OpenFAST. System identification is also used in [38] with FAST simulations, showing limitations to the number of states needed regarding the platform pitch natural frequency, not captured with six states, and the model stability, showing instability for large number of states.

Similarly, [42] uses OpenFAST, in this case to generate a model with 53 states. Then, balanced order reduction is applied to reduce the number of states to 13. Order reduction approaches show great promise to be applied for FOWT.

The equations of motion in [39] are developed using Analytical Mechanics, that is, Hamilton and Lagrange principles. The same approach is employed by [65] with added complexity. On the other hand, Lemmer [23, 27, 35] derived reduced order models based on classical mechanics formalisms.

Models can also be derived in the frequency domain, as shown in [52, 54], leading to much faster results for load calculations.

To derive a model using flexible multi-body dynamics, three steps are taken. First, the kinematics of the system are analysed. This step comprises the definition of the reference frames (both inertial and a body fixed frame for each body undergoing relative translations and/or rotations with respect to the other body-fixed frames) and the calculation of the relative displacements, velocities (and accelerations depending on the formulation used to derive the equations of motion) of each reference frame with respect to the inertial.

Secondly, the kinetics have to be analysed, that is, the forces acting on the system. The forces should be formulated as a function of the system's degrees of freedom and their time derivatives.

Finally, a formalism is chosen to derive the equations of motion. If the Newton-Euler is applied (equivalent to Kane's approach), the accelerations of each body are needed, and the conservation of momentum is applied (equivalent to Newton's second law). On the other hand, the Lagrange-Hamilton approach consists of deriving expressions for the kinetic and potential energy, as well as the generalised forces, and then applying energy conservation to obtain the equations of motion.

Based on the aforementioned literature, it has been determined that a high level of accuracy in the model is unnecessary for effective model-based controller design. Consequently, three simplified models are examined in the subsequent sections. The initial model, proposed by van der Veen [16], accounts for a sole DOF in platform motion, surge, rendering it relatively straightforward to tune. The subsequent model, originally formulated in [66], encompasses two DOFs for platform motion—surge and pitch—promising a heightened level of accuracy. Lastly, this model is adapted to streamline the control design process, incorporating an additional DOF: tower flexibility.

2.3 Simplified model

In [16], a reduced order model is presented, with four degrees of freedom, namely the tower fore-aft bending displacement, $x_{t,b}$, the platform pitch angle, θ_p, the rotor speed, Ω, the tower-top/hub displacement in the fore-aft direction, x_r, which involves a simple geometrical relationship between the tower-top deformation and the platform pitch angular displacement. The only forces considered for this model are the aerodynamic forces. The full set of equations is then,

$$\begin{cases} \ddot{x}_{t,b} + 4\pi\zeta_{tb,1} f_{tb,1}\dot{x}_{t,b} + 4\pi^2 f_{tb,1}^2 x_{t,b} = T(\Omega, V_\infty - \dot{x}_r, \beta)/\tilde{M}_t, \\ \ddot{\theta}_p + 4\pi\zeta_\theta f_\theta \dot{\theta}_p + 4\pi^2 f_\theta^2 \theta_p = H_h T(\Omega, V_\infty - \dot{x}_r, \beta)/\tilde{I}_0, \\ x_r = a_1 x_{t,b} + a_2\theta_p, \\ I_{dr}\dot{\Omega} + R_g Q_g + \alpha\Omega = Q_a(\Omega, V_\infty - \dot{x}_r, \beta)\,. \end{cases} \tag{2.1}$$

Note that the original equations presented in [16] are missing the force normalisation with the corresponding modal inertial terms and the moment-arm of the thrust with respect to the platform pitch motion. The modal tower mass and modal platform pitch inertia are defined as $\tilde{M}_t$ and $\tilde{I}_0$, respectively.

The tower fore-aft bending and platform pitch motions are represented by the first modal contribution, with natural frequency $f_{tb,1}$ and f_θ, and damping $\zeta_{tb,1}$ and ζ_θ, respectively. $a_1 = 1$ and $a_2 = H_h$ are the geometrical constants relating to the tower-top displacement in the fore-aft direction, where the small angle approximation has been used for the platform pitch.

The rotor inertia is defined as I_{dr}, whereas R_g is the gearbox ratio to transform the generator torque from the high-speed shaft (HSS) to the low-speed shaft (LSS). A friction coefficient, α, can be used to better represent the shaft dynamics.

This model's non-linearity originates from the aerodynamic forces, namely the aerodynamic torque and thrust. The aerodynamic torque, Q_a, is given by the aerodynamic torque coefficient,

$$Q_a = \frac{1}{2}\rho\pi R^3 \left(V_\infty - \dot{x}_r\right)^2 c_Q(\Omega, V_\infty - \dot{x}_r, \beta)\,, \tag{2.2}$$

whereas the aerodynamic thrust force, T, is

$$T = \frac{1}{2}\rho\pi R^2 \left(V_\infty - \dot{x}_r\right)^2 c_T(\Omega, V_\infty - \dot{x}_r, \beta)\,, \tag{2.3}$$

and the power extracted by the turbine, dependent on the generator efficiency, η_g, is

$$P_g = \eta_g R_g Q_g \Omega\,. \tag{2.4}$$

The aerodynamic torque and thrust coefficients have been defined by three variables, in agreement with [25], the rotor speed, Ω, the effective *undisturbed* wind speed at the hub, $V_\infty - \dot{x}_r$, and the collective blade pitch angle β, in contrast to the typical two-parameter definition by mean of the tip-speed ratio.

The model derived by Zhang [66], presents differences with van der Veen's model [16]. In this case, the states of the platform are surge and pitch, and the tower is assumed to be fully rigid. The rotor speed state is maintained.

As depicted in Figure 2.1, the reference frame for the surge, x_p, and pitch, θ_p, platform motions is located at the flotation center. Another reference frame can be used in the tower-top to evaluate the fore-aft motion of the tower-top, x_r as a function of the platform motion.

The platform motions are represented as a second-order system, yielding tower-top motion in the fore-aft direction. The drive-train is modelled as a first-order system. The model equations are as follows

$$\begin{cases} (M_s + M_a)\begin{bmatrix} \ddot{x}_p \\ \ddot{\theta}_p \end{bmatrix} + K_s \begin{bmatrix} x_p \\ \theta_p \end{bmatrix} = \begin{bmatrix} \bar{F}_{\text{Hydro}} + T\left(\Omega, V_\infty - \dot{x}_r, \beta\right)\ , \\ \bar{\tau}_{\text{Hydro}} + H_h T\left(\Omega, V_\infty - \dot{x}_r, \beta\right) \end{bmatrix}, \\ x_r = x_p + H_h \theta_p\,, \\ I_{dr}\dot{\Omega} = Q_a\left(V_\infty - \dot{x}_r, \Omega, \beta\right) - Q_g\,, \end{cases} \tag{2.5}$$

where the structural mass matrix of the platform DOFs, M_s, is calculated with respect to the centre of flotation,

$$M_s = \begin{bmatrix} m_{FOWT} & m_{FOWT} z_{CM} \\ m_{FOWT} z_{cg,FOWT} & I_{O,FOWT} \end{bmatrix}. \tag{2.6}$$

The hydrodynamic forces introduce wave-profile-dependent forces and moments $\bar{F}_{hydro}$ and $\bar{\tau}_{hydro}$, as well as an added mass, M_a. The following equations define the hydrodynamic forces and moments

$$\begin{cases} F_{hydro} = & F_{\text{added mass}} + \bar{F}_{\text{Hydro}} = F_{\text{added mass}} + F_{\text{drag}} + F_{\text{inertia}} \\ \tau_{hydro} = & \tau_{\text{added mass}} + \bar{\tau}_{\text{Hydro}} = \tau_{\text{added mass}} + \tau_{\text{drag}} + \tau_{\text{inertia}} \end{cases}, \tag{2.7}$$

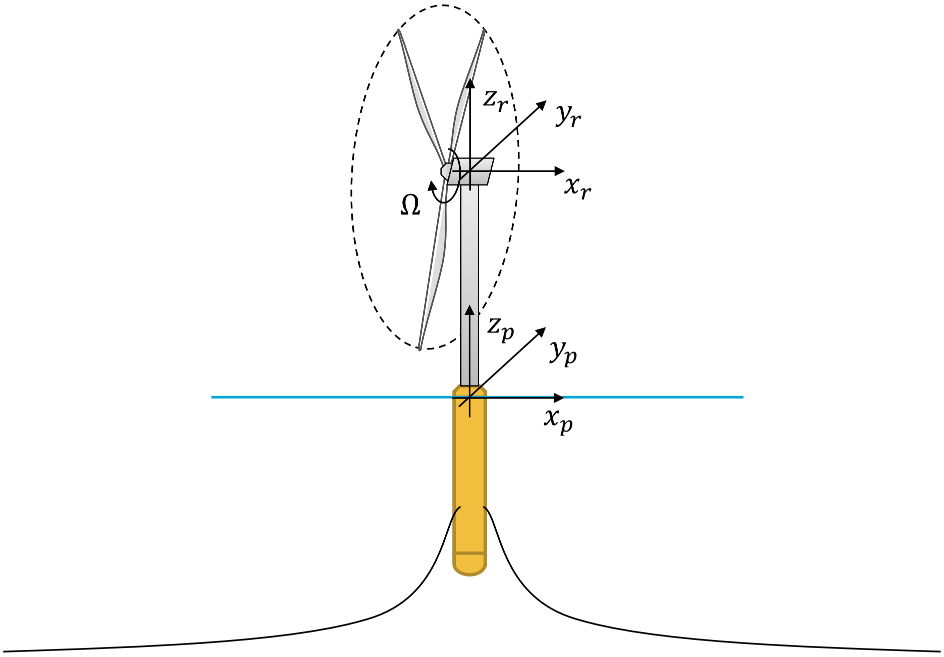

Figure 2.1: Reference frames and states for the simplified model

where the first two terms in both relations correspond to added mass and viscous damping, whereas the last term corresponds to the wave loading and should be considered as an external disturbance effect. It can be noticed that the equation terms are analogous the the Morison equation as presented in [67],

$$F(t) = F_{\text{inertia}}(t) + F_{\text{drag}} = \frac{\pi}{4}\rho_w C_m D_{p,O}^2 \dot{u}(t) + \frac{1}{2}\rho_w C_D D_{p,O} u(t)\|u(t)\| \,, \tag{2.8}$$

where C_m and C_D are the inertia and drag coefficients, respectively, ρ_w is the water density, and $D_{p,O}$ is the diameter of the platform at the flotation level. This equation is generally valid for a slender body.

The added mass matrix is calculated in the model from the application of the Morison equation, leading to

$$M_a = \begin{bmatrix} -\rho_w C_m \frac{\pi}{4} D_{p,O}^2 z_{bot} & -\frac{1}{2}\rho_w C_m \frac{\pi}{4} D_{p,O}^2 z_{bot}^2 \\ -\frac{1}{2}\rho_w C_m \frac{\pi}{4} D_{p,O}^2 z_{bot}^2 & -\frac{1}{3}\rho_w C_m \frac{\pi}{4} D_{p,O}^2 z_{bot}^3 \end{bmatrix} \,, \tag{2.9}$$

where z_{bot} is the vertical position of the keel, measured from the Still Water Level (SWL). The inertia coefficient should be tuned depending on several parameters, although the use of typical values is suggested in [67]. A more detailed derivation of the added mass matrix can be found in [66].

It can be noted that in the equations of motion, no damping term is present. This is because the radiation damping is assumed to be negligible in this case. Moreover, the damping will originate from the hydrodynamic and aerodynamic loads on the structure.

Considering the drag term of the hydrodynamic forces as expressed in the Morison equation, a linear hydrodynamic-damping matrix, C_h, can be computed,

$$C_h = \begin{bmatrix} \rho_w C_D D_{p,0} U_{out} z_{bot} & \frac{1}{2}\rho_{water} C_D D_{p,0} U_{out} z_{bot}^2 \\ \frac{1}{2}\rho_w C_D D_{p,0} U_{out} z_{bot}^2 & \frac{1}{3}\rho_w C_D D_{p,0} U_{out} z_{bot}^3 \end{bmatrix} \begin{bmatrix} \dot{x}_p \\ \dot{\theta}_p \end{bmatrix}, \tag{2.10}$$

where U_{out} is a parameter defined in [54] and used in [66], to simplify the integration of the wave profile. Similar to the previous matrix, in this case the drag coefficient should be tuned according to the platform shape and flow parameters [67].

The restoring stiffness matrix in the platform motion dynamics in Equation 2.5 K_s represents mooring and hydrostatic stiffness combined,

$$K_s = K_m + K_h, \tag{2.11}$$

where K_m represents the mooring line stiffness, whereas K_h originates from the hydrostatic forces. The mooring stiffness is obtained considering a linear spring system,

$$K_m = \begin{bmatrix} k_{moor} & k_{moor} z_{moor} \\ k_{moor} z_{moor} & k_{moor} z_{moor}^2 \end{bmatrix}, \tag{2.12}$$

where k_{moor} is the stiffness of the spring, and z_{moor} is the mooring line fair-lead vertical position. The hydrostatic stiffness has a single component in the pitch DOF,

$$K_h = \begin{bmatrix} 0 & 0 \\ 0 & m_{tot} g \left(z_{cb} - z_{cg}\right) + \rho_w g \frac{\pi}{64} D_{p,O}^4 \end{bmatrix}, \tag{2.13}$$

where m_{tot} is the total mass of the FOWT, z_{cb} is the vertical location of the center of buoyancy, z_{cg} is the center of gravity of the FOWT.

2.3.1 Linearisation of aerodynamic forces

The aerodynamic forces acting on a wind turbine are highly non-linear; however, for control design purposes, having a linear representation of the system is preferred. Thus, the aerodynamic forces need to be linearised. Using first-order linear expansion,

$$\begin{aligned} T(V_{\text{in,op}} + \Delta V_{\text{in}}, \Omega_{\text{op}} + \Delta\Omega, \beta_{\text{op}} + \Delta\beta) &\approx \\ T(V_{\text{in,op}}, \Omega_{\text{op}}, \beta_{\text{op}}) + \left.\frac{\partial T}{\partial V_{\text{in}}}\right|_{\text{op}} \Delta V_{in} + \left.\frac{\partial T}{\partial \Omega}\right|_{\text{op}} \Delta\Omega + \left.\frac{\partial T}{\partial \beta}\right|_{\text{op}} \Delta\beta + O(\Delta^2) &\approx \\ T(V_{\text{in,op}}, \Omega_{\text{op}}, \beta_{\text{op}}) + C_{T,V_{\text{in}}}\Delta V_{\text{in}} + C_{T,\Omega}\Delta\Omega + C_{T,\beta}\Delta\beta + O(\Delta^2)&, \end{aligned} \tag{2.14}$$

$$\begin{aligned} Q_a(V_{\text{in,op}} + \Delta V_{\text{in}}, \Omega_{\text{op}} + \Delta\Omega, \beta_{\text{op}} + \Delta\beta) &\approx \\ Q_a(V_{\text{in,op}}, \Omega_{\text{op}}, \beta_{\text{op}}) + \left.\frac{\partial Q_a}{\partial V_{\text{in}}}\right|_{\text{op}} \Delta V_{\text{in}} + \left.\frac{\partial Q_a}{\partial \Omega}\right|_{\text{op}} \Delta\Omega + \left.\frac{\partial Q_a}{\partial \beta}\right|_{\text{op}} \Delta\beta + O(\Delta^2) &\approx \\ Q_a(V_{\text{in,op}}, \Omega_{\text{op}}, \beta_{\text{op}}) + C_{Q,V_{\text{in}}}\Delta V_{\text{in}} + C_{Q,\Omega}\Delta\Omega + C_{Q,\beta}\Delta\beta + O(\Delta^2)&. \end{aligned} \tag{2.15}$$

The partial derivatives are manually computed using HAWC2 steady wind simulations and a central first-order finite differences scheme, such that

$$C_{Q,\Omega} = \left.\frac{\partial Q_a}{\partial \Omega}\right|_{\text{op}} \approx \frac{Q_a(V_{in,op}, \Omega_{op} + \Delta\Omega, \beta_{op}) - Q_a(V_{in,op}, \Omega_{op} - \Delta\Omega, \beta_{op})}{2\Delta\Omega} , \tag{2.16}$$

and similarly for all the derivatives previously outlined in Equation 2.14 and Equation 2.15. Clearly, the aerodynamic sensitivities depend on the operating condition and the spacing $\Delta(\cdot)$ used for the calculation. The wind force and moment on the platform surge and pitch degrees of freedom can now be expressed in a linear form as

$$\begin{aligned}\begin{bmatrix} T \\ H_h T \end{bmatrix} \approx \begin{bmatrix} T_{op} \\ H_h T_{op} \end{bmatrix} &+ \underbrace{\begin{bmatrix} C_{T,\Omega} & -C_{T,V_{in}} \\ C_{T,\Omega} H_h & -C_{T,V_{in}} H_h \end{bmatrix}}_{C_a} \begin{bmatrix} \Delta\dot{\Omega} \\ \Delta\dot{x}_r \end{bmatrix} \\ &+ \underbrace{\begin{bmatrix} C_{T,\beta} & 0 \\ C_{T,\beta} H_h & 0 \end{bmatrix}}_{B_a} \begin{bmatrix} \Delta\beta \\ \Delta Q_g \end{bmatrix} + \underbrace{\begin{bmatrix} C_{T,V_{in}} & 0 & 0 \\ C_{T,V_{in}} H_h & 0 & 0 \end{bmatrix}}_{E_a} \begin{bmatrix} \Delta V_\infty \\ \Delta F_{h,inertial} \\ \Delta \tau_{h,inertial} \end{bmatrix} .\end{aligned} \tag{2.17}$$

It is clear that the aerodynamic thrust acts as a damping term in the structure, C_a. Additionally, the effect from the inputs, B_a, can be separated from the effect from the disturbances, E_a, for convenience for the state-space formulation outlined in the following paragraphs.

2.3.2 State space formulation

The linearised model can be expressed in its state-space form, as it will be used for both the open-loop and closed-loop implementation for validation and control design. The objective is to represent the system in the following form

$$\begin{cases} \Delta\dot{x} = & A\Delta x + B\Delta u + E\Delta d \\ \Delta y = & C\Delta x + D\Delta u \\ \Delta z = & C_z\Delta x + D_z\Delta u \end{cases} , \tag{2.18}$$

x comprising the system states, u the controller inputs, d the disturbances, y the measured variables and z the outputs. Only the deviations with respect to the linearisation point are considered; that is, just the deviation variables are included,

$$\Delta x = x - x_{op}, \quad \Delta u = u - u_{op}, \quad \Delta d = d - d_{op}, \quad \Delta y = y - y_{op}, \quad \Delta z = z - z_{op} . \tag{2.19}$$

The first step is to reduce all the Ordinary Differential Equations (ODEs) to first order and to do that the state vector is defined as combining the original states with their first derivatives,

$$\Delta x = \left[\Delta x_p, \Delta\theta_p, \Delta\phi, \Delta x_r, \Delta\dot{x}_p, \Delta\dot{\theta}_p, \Delta\Omega, \Delta\dot{x}_r\right]^T . \tag{2.20}$$

where *phi* corresponds to the rotor azimuth, which is not explicitly modelled in the equations of motion (see Equation 2.5). Thus, the time derivative is represented as

$$\Delta\dot{x} = \left[\Delta\dot{x}_p, \Delta\dot{\theta}_p, \Delta\Omega, \Delta\dot{x}_r, \Delta\ddot{x}_p, \Delta\ddot{\theta}_p, \Delta\dot{\Omega}, \Delta\ddot{x}_r\right]^T . \tag{2.21}$$

The controller inputs are the collective blade pitch and the generator torque,

$$\Delta u = \left[\Delta\beta, \Delta Q_g\right]^T . \tag{2.22}$$

The disturbances are the uncontrolled variables affecting the system's response, that is, the undisturbed wind speed, the hydrodynamic inertial force and moment,

$$\Delta d = \left[\Delta V_\infty, \Delta F_{h,inertial}, \Delta\tau_{h,inertial}\right]^T . \tag{2.23}$$

The states matrix can be built then as

$$A_{8\times 8} = \begin{bmatrix} 0_{4\times 2} & 0_{4\times 2} & I_{4\times 4} \\ \left(M_s + M_a\right)^{-1} K_s & 0_{2\times 2} & \left(M_s + M_a\right)^{-1} C_p \\ 0_{1\times 2} & 0_{1\times 2} & I_{dr}^{-1} C_{dr} \\ K_r & 0_{1\times 2} & C_r \end{bmatrix} , \tag{2.24}$$

where I is an identity matrix. The platform damping matrix is composed of the hydrodynamic and aerodynamic damping as follows

$$C_p = \left[C_h, C_a\right] . \tag{2.25}$$

The drive train damping originates from the aerodynamic torque sensitivities to the rotor speed and inflow speed

$$C_{dr} = \left[0, 0, C_{Q_a,\Omega}, -C_{Q_a,V_{in}}\right] . \tag{2.26}$$

The tower-top stiffness and damping

$$K_r = \left[A_{51} + A_{61} H_h, A_{52} + A_{62} H_h\right] , \tag{2.27}$$

and

$$C_r = \left[A_{55} + A_{65} H_h, A_{56} + A_{66} H_h, A_{57} + A_{67} H_h, A_{58} + A_{68} H_h\right] , \tag{2.28}$$

respectively, are directly related to the surge and pitch motions of the platform due to the rigid body assumption.

The input matrix is defined as

$$B = \begin{bmatrix} 0_{4\times 2} \\ \left(M_s + M_a\right)^{-1} B_a \\ I_{dr}^{-1} B_{dr} \\ B_r \end{bmatrix} , \tag{2.29}$$

where the drive train contribution is given by

$$B_{dr} = \left[C_{Q_a,\beta}, -1 \right] \ . \tag{2.30}$$

The aerodynamic contribution to the platform motion is defined by the following relation

$$B_a = \left[\begin{array}{cc} C_{T,\beta} & 0 \\ C_{T,\beta} H_h & 0 \end{array} \right] , \tag{2.31}$$

and the contribution of the surge and pitch velocity on the tower-top is as follows

$$B_r = \left[B_{51} + B_{61} H_h, B_{52} + B_{62} H_h \right] \ . \tag{2.32}$$

The disturbance matrix collects the contributions from the deviation in the wind speed, hydrodynamic force and moment with respect to the operating/linearisation point, as shown in the below equation

$$E = \left[\begin{array}{c} 0_{4\times 3} \\ \left(M_s + M_a\right)^{-1} E_a \\ I_{dr}^{-1} E_{dr} \\ E_r \end{array} \right] , \tag{2.33}$$

where the drive train contribution is given by

$$E_{dr} = \left[C_{Q_a,V_{in}}, 0, 0 \right] , \tag{2.34}$$

the contribution of the aerodynamic loads to the platform motion is

$$E_a = \left[\begin{array}{ccc} C_{T,V_{in}} & 0 & 0 \\ C_{T,V_{in}} H_h & 0 & 0 \end{array} \right] , \tag{2.35}$$

whereas the tower-top contribution is again dependent on the surge and pitch motion,

$$E_r = \left[E_{51} + E_{61} H_h, E_{52} + E_{62} H_h, E_{53} + E_{63} H_h \right] \ . \tag{2.36}$$

The output matrix is considered an identity matrix in this work, $C = I_{N_m \times 8}$, unless otherwise stated, where N_m is the number of measurements. The feedthrough matrix is is considered a zero matrix $D = 0_{N_m \times 2}$. The output matrix C_z depends on the controller formulation and required outputs, similarly the output feedthrough matrix D_z.

2.4 Extended model

The above derived simplified model can be improved by adding the flexibility aspect of the tower (fore-aft) motion. Thus a second-order approximation of the first tower mode is added as an extension to the model in Equation 2.5. In that case, the equations of motion of the system become

$$
\begin{cases}
(M_s + M_a) \begin{bmatrix} \ddot{x}_p \\ \ddot{\theta}_p \end{bmatrix} + K_s \begin{bmatrix} x_p \\ \theta_p \end{bmatrix} = \begin{bmatrix} \bar{F}_{\text{Hydro}} + T\left(\Omega, V_\infty - \dot{x}_r, \beta\right) \\ \bar{\tau}_{\text{Hydro}} + \tau_{\text{wind}}\ \left(\Omega, V_\infty - \dot{x}_r, \beta\right) \end{bmatrix}, \\
\ddot{x}_{tt} + 4\pi\zeta_{t,1} f_{t,1}\dot{x}_{tt} + 4\pi^2 f_{t,1}^2 x_{tt} = T(\Omega, V_\infty - \dot{x}_r, \beta)/\tilde{M}_t \,, \\
I_{dr}\dot{\Omega} = Q_a\left(\Omega, V_\infty - \dot{x}_r, \beta\right) - Q_g \,, \\
x_r = x_p + H_h\theta_p + x_t \,.
\end{cases}
\tag{2.37}
$$

The states of this model are

$$
\Delta x = \left[\Delta x_p, \Delta\theta_p, \Delta x_t, \Delta\phi, \Delta x_r, \Delta\dot{x}_p, \Delta\dot{\theta}_p, \Delta\dot{x}_t, \Delta\Omega, \Delta\dot{x}_r\right]^T \,. \tag{2.38}
$$

The system matrix is rewritten now as

$$
A_{10\times10} = \begin{bmatrix} 0_{5\times2} & 0_{5\times3} & I_{5\times5} \\ \left(M_s + M_a\right)^{-1} K_s & 0_{2\times3} & \left(M_s + M_a\right)^{-1} C_p \\ 0_{1\times2} & 0_{1\times3} & \tilde{M}_t^{-1} C_{tb} \\ 0_{1\times2} & 0_{1\times3} & I_{dr}^{-1} C_{dr} \\ K_t & 0_{1\times2} & C_r \end{bmatrix} . \tag{2.39}
$$

In this case, aerodynamic damping appears on the tower fore-aft bending DOF, C_{tb},

$$
C_{tb} = \left[0, 0, 0, C_{T,\Omega}, -C_{T,V_{in}}\right] \,, \tag{2.40}
$$

The input matrix is in this case

$$
B = \begin{bmatrix} 0_{5\times2} \\ \left(M_s + M_a\right)^{-1} B_a \\ \tilde{M}_t^{-1} C_{T,\beta} \\ I_{dr}^{-1} B_{dr} \\ B_r \end{bmatrix} , \tag{2.41}
$$

where the rotor fore-aft motion input matrix contribution is given by

$$
B_r = \left[B_{61} + B_{71} H_h + B_{81}, B_{62} + B_{72} H_h + B_{82}\right] \,. \tag{2.42}
$$

The disturbance matrix is

$$
E = \begin{bmatrix} 0_{5\times3} \\ \left(M_s + M_a\right)^{-1} E_a \\ \tilde{M}_t^{-1} C_{T,V_{in}} \\ I_{dr}^{-1} E_{dr} \\ E_r \end{bmatrix} . \tag{2.43}
$$

The aerodynamic disturbance effects on the platform motion, E_a, are as in Equation 2.35, whereas the rotor fore-aft motion disturbance matrix contribution is given, similarly to Equation 2.42,

$$E_r = [E_{61} + E_{71}H_h + E_{81}, E_{62} + E_{72}H_h + E_{82}] \ . \tag{2.44}$$

Note that several matrices have been defined initially in the simplified model, however they should be adapted due to the additional state in the extended model. It is not presented here for conciseness, since it is a trivial exercise.

2.5 Final remarks

The modelling task of wind turbines in general, and floating wind turbines in particular, can be undertaken by several means. Using system identification or order reduction from existing higher order models can provide a fast and high accuracy method. On the other hand, developments based on first principles can lead to a better understanding of the system, at the expense of a more cumbersome process. During the previous sections fairly simple reduced order models have been presented and analysed, with a partial focus on the linearization of the aerodynamic forces, and the inclusion of both hydrodynamic and aerodynamic loads in the state-space formulation of the model. Finally, the matrices needed to implement a linear state-space model are defined for two models, the simplified model, and the extended model, where tower flexibility is added.

CHAPTER 3

Model validation

The model is applied to the IEA-15MW Reference Wind Turbine (IEA-15MW RWT) [68] mounted on the WindCrete Spar-Buoy (SB) [69] floater. This choice allows for assessing the response of what could be expected to be full-scale floating wind turbines over the coming years. Currently, the largest floating wind farm is based on spar-buoy-type floaters. Additionally, the largest wind turbines installed are quickly approaching the 15MW rating in European offshore wind farms.

Originally, the WindCrete SB was designed for a 5MW WTG. The monolithic cylindrical structure has been up-scaled [70] to hold the IEA-15MW RWT. The response has been investigated by Mahfouz et al. [71].

To study the validity of the model, the previously mentioned reference WTG and floater are used. The following sections list the main parameters required for the reduced order model, and the validation of the model is performed compared to HAWC2 simulations.

3.1 WindCrete floater definition

The reference floater used for the present work is the WindCrete floater, upscaled for the 15MW turbine. In the definition report, the structure contains three elements: the spar-buoy, the transition piece, and the tower. For the purpose of this exercise, the tower will be considered a separate part from the floating platform. The main parameters required for the model definition are shown in Table 3.1. A diagram with relevant measurements of the geometry is shown in Figure 3.1.

Table 3.1: Key substructure parameters, both structural and hydrostatic [70].

Parameter	**Value**
Mass including ballast (Not including tower)	$3.655 \cdot 10^7$ kg
Vertical Center of Gravity (with respect to MSL)	-113.08 m
Vertical Center of Buoyancy (with respect to MSL)	-77.29 m
Pitch moment of inertia, $I_{p,yy}$, about CG	$5.590 \cdot 10^{10}$ kg $\cdot$ m^2
Displaced water volume	$4.054 \cdot 10^4$ m^3
Pitch hydrostatic stiffness C_{55} at sea water level	$-3.146 \cdot 10^{10}$ N $\cdot$ m/rad
Surge stiffness, $K_{m,11}$	$5.052 \cdot 10^5$ N/m
Fairleads depth with respect to MSL, z_{frl}	-90 m

The added mass of the platform, M_a, is shown in the *corewind* report [70] and has been calculated using potential flow theory, resulting in the following for infinite frequency, noting that only the surge and pitch values are reproduced,

$$M_{a,PF} = \begin{bmatrix} 3.735 \cdot 10^7 \text{ kg} & -2.964 \cdot 10^9 \text{ kg} \cdot \text{m} \\ -2.964 \cdot 10^9 \text{ kg} \cdot \text{m} & 2.916 \cdot 10^{11} \text{ kg} \cdot \text{m}^2 \end{bmatrix}, \tag{3.1}$$

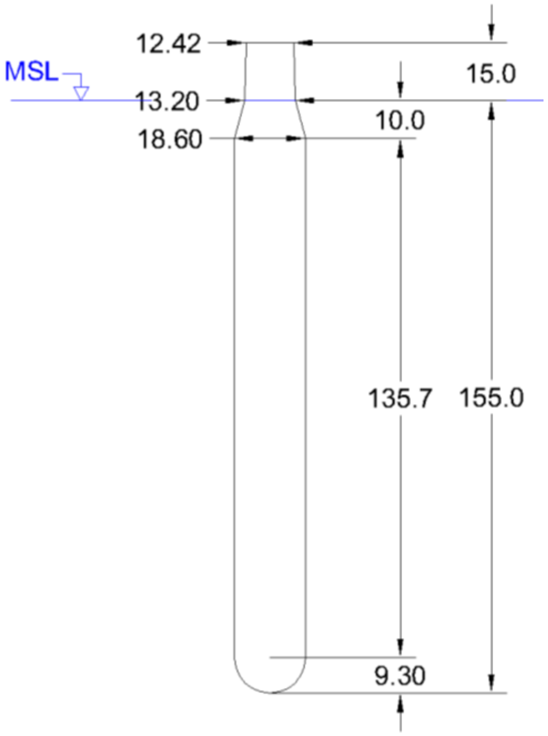

Figure 3.1: Substructure plan. The values are in meters. Mean Sea Level (MSL) is equivalent to SWL. Reprinted from [70]

where the subscript PF stands for potential flow. On the other hand, in [66], the added mass was computed following the Morison equation, leading to

$$M_{a,ME} = \begin{bmatrix} 4.161 \cdot 10^7 \text{ kg} & -3.213 \cdot 10^9 \text{ kg} \cdot \text{m} \\ -3.213 \cdot 10^9 \text{ kg} \cdot \text{m} & 4.164 \cdot 10^{11} \text{ kg} \cdot \text{m}^2 \end{bmatrix} . \tag{3.2}$$

The structural mass matrix can be extracted from HAWC2, which is assumed to generate a higher accuracy result due to the multi-body formulation being able to couple all DOFs, leading to the following

$$M_{s,HAWC2} = \begin{bmatrix} 0.413 \cdot 10^8 \text{ kg} & -0.384 \cdot 10^{10} \text{ kg} \cdot \text{m} \\ -0.384 \cdot 10^{10} \text{ kg} \cdot \text{m} & 0.565 \cdot 10^{12} \text{ kg} \cdot \text{m}^2 \end{bmatrix} . \tag{3.3}$$

If, instead, Equation 2.6 is used, the following values are obtained

$$M_{s,Analytical} = \begin{bmatrix} 0.408 \cdot 10^8 \text{ kg} & -0.378 \cdot 10^{10} \text{ kg} \cdot \text{m} \\ -0.378 \cdot 10^{10} \text{ kg} \cdot \text{m} & 0.559 \cdot 10^{12} \text{ kg} \cdot \text{m}^2 \end{bmatrix} , \tag{3.4}$$

which shows a close match, with less of 1.5% difference for each element with respect to the HAWC2 super-element result. On the other hand, the combination of the structural mass with the added mass from the corewind report shows a significant miss-match when compared to the total mass obtained from HAWC2 Superelement, as shown in [66],

$$M_{tot,SE} = \begin{bmatrix} 8.265 \cdot 10^7 \text{ kg} & -8.060 \cdot 10^9 \text{ kg} \cdot \text{m} \\ -8.060 \cdot 10^9 \text{ kg} \cdot \text{m} & 1.066 \cdot 10^{12} \text{ kg} \cdot \text{m}^2 \end{bmatrix}. \tag{3.5}$$

Finally, the total mass used in the model is the combination of the analytical structural mass, $M_{s,Analytical}$, and Morison equation calculation, $M_{a,ME}$, that is, Equation 3.4 and Equation 3.2.

For the model, the mooring stiffness and vertical position of the fairleads are required in order to compute the linearized stiffness matrix. Considering the surge stiffness and fairleads position with respect to MSL, as given in Table 3.1, that is, $K_{m,11}$ and z_{frl}, Equation 2.12 can be used. The pitch hydrostatic stiffness is listed in Table 3.1. Combining them, the total stiffness is

$$K_{analytical} = \begin{bmatrix} 5.052 \cdot 10^5 \text{ N/m} & -4.547 \cdot 10^7 \text{ N} \\ -4.547 \cdot 10^7 \text{ N} & 1.019 \cdot 10^{10} \text{ N} \cdot \text{m} \end{bmatrix}. \tag{3.6}$$

The stiffness matrix has also been obtained in [66] using the HAWC2 Superelement approach,

$$K_{SE} = \begin{bmatrix} 4.915 \cdot 10^5 \text{ N/m} & -4.890 \cdot 10^7 \text{ N} \\ -5.048 \cdot 10^7 \text{ N} & 1.109 \cdot 10^{10} \text{ N} \cdot \text{m} \end{bmatrix}. \tag{3.7}$$

The values from $K_{analytical}$ and K_{SE} are quite similar, proving the validity of the modelling. However, the mooring line pitch stiffness value was slightly tuned to match the natural frequencies of the floating wind turbine system,

$$K_{model} = \begin{bmatrix} 5.052 \cdot 10^5 \text{ N/m} & -4.547 \cdot 10^7 \text{ N} \\ -4.547 \cdot 10^7 \text{ N} & 1.055 \cdot 10^{10} \text{ N} \cdot \text{m} \end{bmatrix}. \tag{3.8}$$

The hydrodynamic damping matrix, C_h, was obtained in [66] by performing decay tests in HAWC2 simulations, leading to

$$C_h = \begin{bmatrix} -1.971 \cdot 10^5 \text{ N} \cdot \text{s/m} & 4.812 \cdot 10^6 \text{ N} \cdot \text{s} \\ 4.812 \cdot 10^6 \text{ N} \cdot \text{s} & -1.059 \cdot 10^9 \text{ N} \cdot \text{m} \cdot \text{s} \end{bmatrix}. \tag{3.9}$$

The final substructure model values used are

$$M_a = \begin{bmatrix} 3.735 \cdot 10^7 \text{ kg} & -2.964 \cdot 10^9 \text{ kg} \cdot \text{m} \\ -2.964 \cdot 10^9 \text{ kg} \cdot \text{m} & 2.916 \cdot 10^{11} \text{ kg} \cdot \text{m}^2 \end{bmatrix}, \tag{3.10}$$

$$M_s = \begin{bmatrix} 0.413 \cdot 10^8 \text{ kg} & -0.384 \cdot 10^{10} \text{ kg} \cdot \text{m} \\ -0.384 \cdot 10^{10} \text{ kg} \cdot \text{m} & 0.565 \cdot 10^{12} \text{ kg} \cdot \text{m}^2 \end{bmatrix}, \tag{3.11}$$

$$K_s = \begin{bmatrix} 5.052 \cdot 10^5 \text{ N/m} & -4.547 \cdot 10^7 \text{ N} \\ -4.547 \cdot 10^7 \text{ N} & 1.055 \cdot 10^{10} \text{ N} \cdot \text{m} \end{bmatrix}, \tag{3.12}$$

$$C_h = \begin{bmatrix} -1.971 \cdot 10^5 \text{ N} \cdot \text{s/m} & 4.812 \cdot 10^6 \text{ N} \cdot \text{s} \\ 4.812 \cdot 10^6 \text{ N} \cdot \text{s} & -1.059 \cdot 10^9 \text{ N} \cdot \text{m} \cdot \text{s} \end{bmatrix}. \tag{3.13}$$

Finally, the aerodynamic damping, C_a, aerodynamic effect of inputs, B_a, and disturbances, E_a, are computed based on the linearization of aerodynamic forces, as explained in subsection 2.3.1. The values are shown in [66], which depend on the WTG characteristics outlined in the next section, whereas the linearization of aerodynamic loads is described in section 3.3.

3.2 IEA-15MW Reference Wind Turbine

The IEA-15MW RWT was selected for the thesis project. The key parameters are detailed in Table 3.2. Some of them are necessary for the definition of the reduced order model, whereas others are only presented to aid in the analysis. The HAWC2 models are publicly available on GitHub [72].

Table 3.2: Key specifications of IEA-15MW Reference Wind Turbine [68]

Parameter	**Value**
Wind turbine IEC class	1B
Power rating, P_N	15 MW
Rated thrust, T_N	2.4 MN
Hub height (from SWL), H_h^*	135.495 m
Drive train type	Direct drive
Minimum rotor speed, Ω_{min}	5.0 rpm
Maximum rotor speed, Ω_N	7.56 rpm
Maximum tip speed, $V_{tip,max}$	95 m/s
Design tip-speed ratio, λ_{opt}	9.0
Cut-in wind speed, v_{ci}	3 m/s
Cut-out wind speed, v_{co}	25 m/s
Rotor diameter, D_r	240 m
Rated wind speed, V_N	10.59 m/s
Blade mass, m_b	65 t
Mass of Rotor-Nacelle Assembly (RNA), m_{RNA}	1016 t
Drive-train inertia, I_{dr}	$3.1465 \cdot 10^8$ kg $\cdot$ m^2
Tower mass, m_t	860 t
Tower height, L_t	129.582 m

* The hub-height has been adapted to match the HAWC2 model

The IEA-15MW RWT has been originally designed for bottom-fixed offshore configuration, as shown in Figure 3.2, leading to a hub-height of 150 m. The 15-meter transition piece in the WindCrete SB, and shortening of the tower in the HAWC2 model leads to the hub-height being located 135.495 m above MSL.

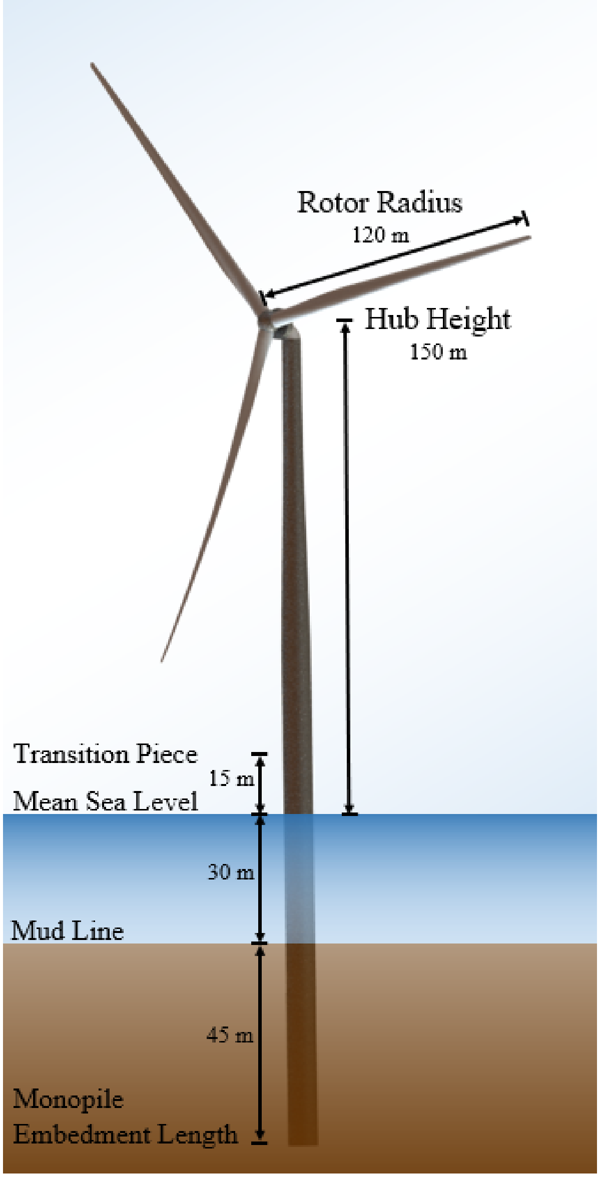

Figure 3.2: IEA-15MW RWT with Monopile configuration. Note that the hub height depicted does not correspond to the model used and evaluated. Reprinted from [68].

3.3 Linearised aerodynamic loads

The model described in section 2.3 relies on the linearised aerodynamics of the IEA-15MW rotor. Although the software HAWCStab2 [40] can compute the aerodynamic gradients of a given rotor, it does not account for the motions of the FOWT, which were found in [66] to significantly affect aerodynamic loads. Thus, steady closed-loop HAWC2 simulations are conducted at various operating points to calculate gradients for the aerodynamic thrust force, T, and torque, Q_a, with respect to the undisturbed wind speed, $\partial\left(\cdot\right)_a/\partial V_\infty \equiv C_{(\cdot)_a,V_\infty}$, rotor speed, $\partial\left(\cdot\right)_a/\partial\Omega \equiv C_{(\cdot)_a,\Omega}$, and demanded pitch angle, $\partial\left(\cdot\right)_a/\partial\beta_d \equiv C_{(\cdot)_a,\beta_d}$.

To determine the operating values of the demanded pitch at each analysed wind speed, a de-tuned controller, outlined in chapter 4, is utilised. The rotor speed is also checked against the rated rotor speed as a validation step. The simulations are run long enough to dampen transients and oscillations, after which the mean value of the remaining time signal is calculated.

The resulting operating points at various wind speeds are depicted in Figure 3.3. Of particular interest are wind speeds above the rated value, as platform pitch instability occurs during full load operation. The original data points were computed by [66], and additional operating points were later calculated, highlighting the linearity between the selected operation points. In the original case, the computed gradients were based on $\Delta V_\infty = 0.5$ m/s, with unknown steps for blade pitch and rotor speed. To assess gradient sensitivity, three different offset values for each variable—$\Delta\Omega$, $\Delta\beta_d$, and ΔV_∞—were considered and depicted with error bars in the figure.

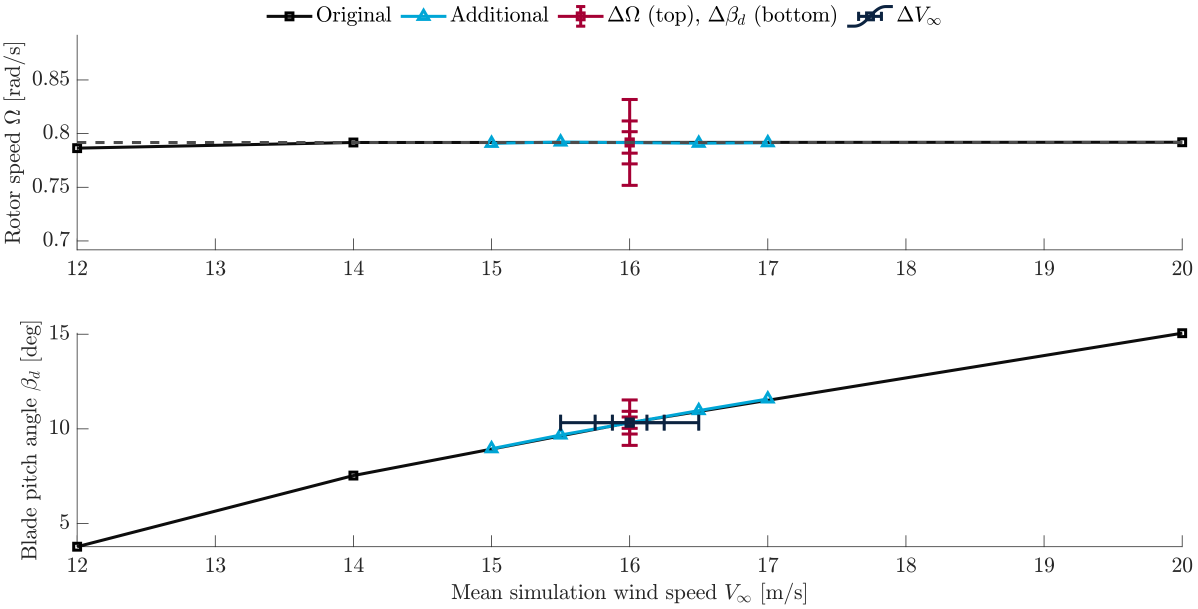

Figure 3.3: Operating points and visual description of aerodynamic gradients' calculation. The original points depict the existing gradients computed in [66], additional points are used to compute the corresponding operating conditions. The error bars represent the deviations imposed in the operation points to compute the aerodynamic gradients.

Following the finite difference approach outlined in subsection 2.3.1, the aerodynamic gradients were computed for all three cases. In Figure 3.4 and Figure 3.5 the resulting aerodynamic torque and thrust gradients are shown respectively.

A mismatch can be observed in the aerodynamic torque derivative with respect to the wind speed. This may be caused by a mismatch in the steady-state blade pitch angle, or by a different transient time considered. The results for all aerodynamic torque calculations seem to be highly insensitive to the step in wind speed, rotor speed and blade pitch angle.

On the other hand, the derivative of the thrust with respect to the blade pitch angle is slightly affected by the step in blade pitch, and overall a marginal mismatch is found with respect to the original calculations. Similarly to the derivative with respect to the wind speed. Furthermore, the thrust gradient is clearly non-linear with respect to the blade pitch, in contrast to the rotor speed and wind speed in the region considered.

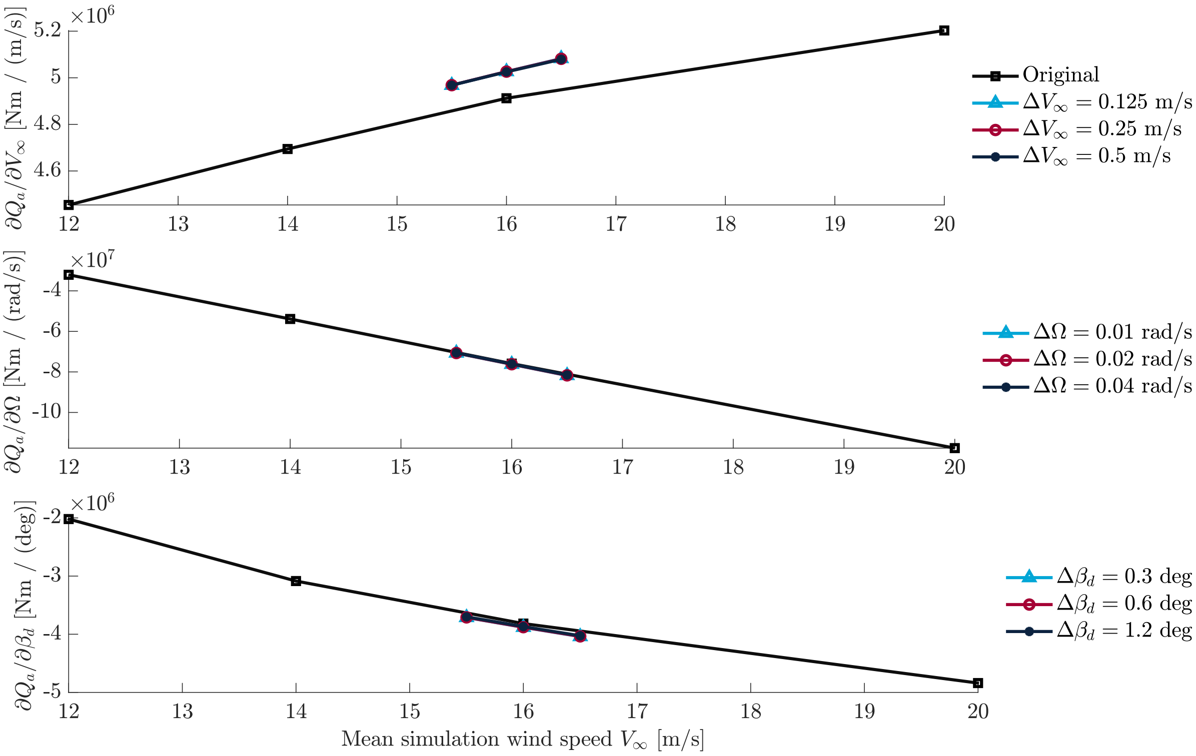

Figure 3.4: Aerodynamic torque gradients' calculation. The original points depict the existing gradients computed in [66], additional points are used to compute the gradients based on different offsets, indicated on the right of the figure.

To gain a deeper understanding of the sensitivity of the aerodynamic forces to the wind speed, the relative value between the aerodynamic torque and thrust gradients is computed at $V_\infty = 16$ m/s and $\Delta V_\infty = \pm 0.5$ m/s. This computation is then illustrated in Figure 3.6. It is evident that variations in the thrust gradients are more pronounced compared to those in the aerodynamic torque.

These observations underscore the need for scheduling the model used during turbulent wind simulations to obtain accurate load predictions, particularly under conditions of higher turbulence. This is important since the gradients are likely to undergo non-negligible variations. However, important limitations are introduced by only considering a steady wind calculation, which neglect unsteady aerodynamic effects.

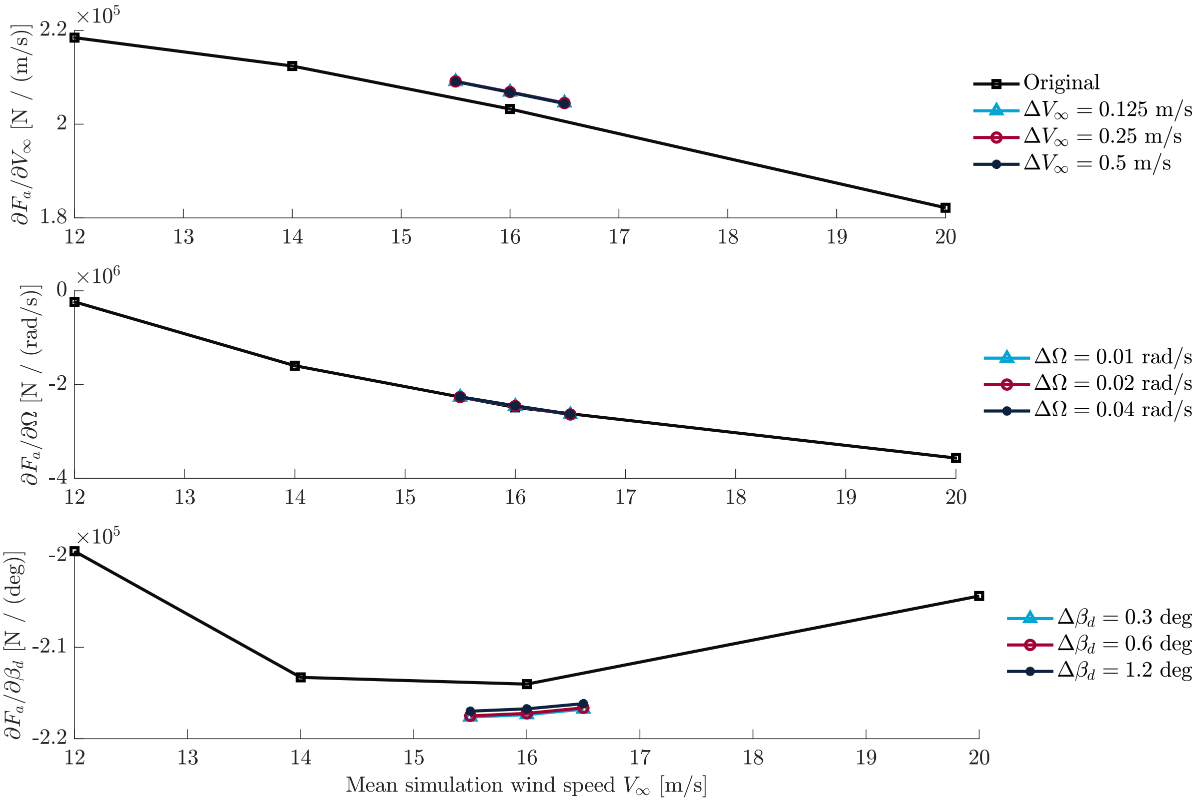

Figure 3.5: Aerodynamic thrust gradients' calculation. The original points depict the existing gradients computed in [66], additional points are used to compute the gradients based on different offsets, indicated on the right of the figure.

3.4 Modal analysis

The floating wind turbine's natural frequencies are detailed in [70]. To validate the model and ensure its capability to capture the dynamic behaviour of the floating wind turbine, the natural frequencies are analysed using various methods, as presented in Table 3.3. The calculation method inherently introduces a degree of error, yet the results exhibit a reasonable level of agreement. Notably, both reduced-order models over-predict the surge natural frequency when compared to HAWC2, considered the baseline as it is employed for coupled simulations. On the other hand, the pitch natural frequencies show a satisfactory match with HAWC2. It's worth noting that certain degrees of freedom are either excluded in the reduced-order models or are not analysed within HAWC2.

Additionally, to better understand the stability of the system, the pole-zero map is plotted in Figure 3.7, based on the simplified model. The results show the poles and zeros for the collective blade pitch to rotor speed. There are RHPZ for the pitch motion for the lower wind speeds, close to rated wind speed, likely due to the large magnitude of the rotor thrust derivative with wind speed. These zeroes move towards the left as the wind speed increases, in a behaviour observed in the literature [56, 73].

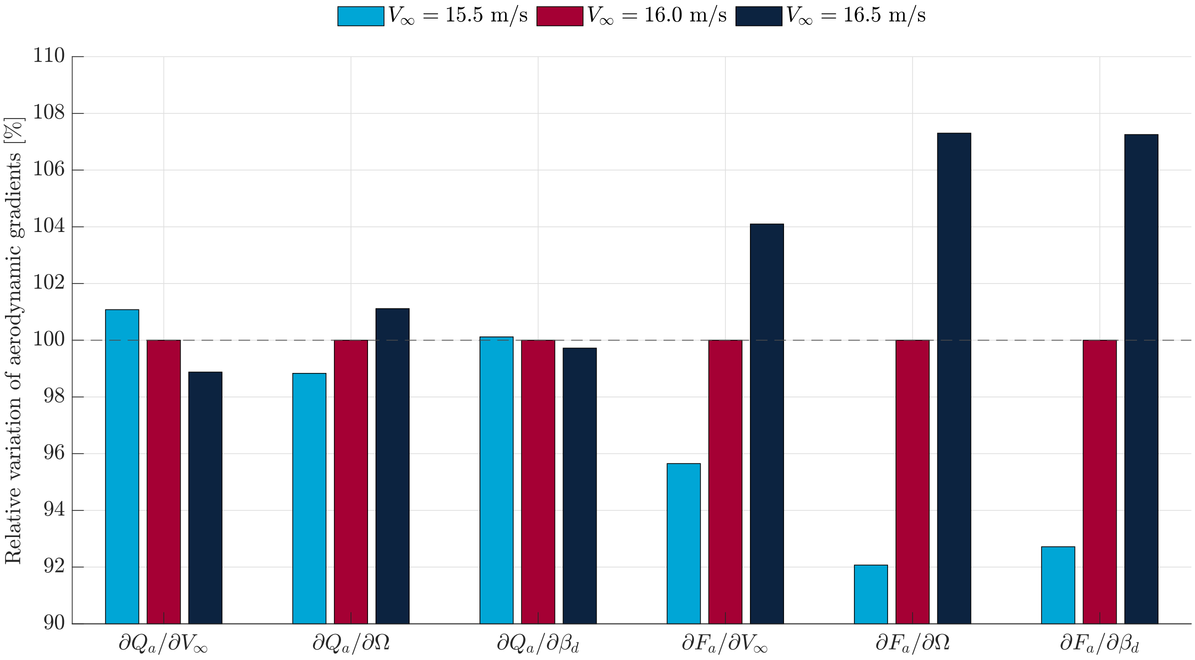

Figure 3.6: Relative normalised aerodynamic gradients around $V_\infty = 16$ m/s.

Table 3.3: Validation of natural frequencies from reduced order linear models.

Natural frequencies in Hz	Surge	Pitch	Heave	Yaw	Tower
Decay test OpenFAST [71]	0.01221	0.02441	0.03052	0.09155	0.5
Signal FFT HAWC2	0.010	0.026	0.033	-	-
Simplified model	0.012	0.023	-	-	-
Extended model	0.013	0.025	-	-	0.498

3.5 Linear model open-loop simulations

The linear simulations are performed by building the Linear Time-Invariant models (LTI) described in subsection 2.3.2 and section 2.4, in continuous time,

$$\begin{cases} \Delta\dot{x}(t) = & A_c\Delta x(t) + B_c\Delta u(t) + E_c\Delta d(t) \\ \Delta y(t) = & C\Delta x(t) + D\Delta u(t) \\ \Delta z(t) = & C_z\Delta x(t) + D_z\Delta u(t) \end{cases}, \tag{3.14}$$

which is further discretized using matricial exponentiation,

$$\begin{bmatrix} A_d & B_d & E_d \\ 0 & I & 0 \\ 0 & 0 & I \end{bmatrix} = \exp\left(\begin{bmatrix} A_c & B_c & E_c \\ 0 & 0 & 0 \\ 0 & 0 & 0 \end{bmatrix} T_s\right), \tag{3.15}$$

where T_s is the sampling time. The sampling time should be chosen such that the sampling frequency, $f_s = 1/T_s$, is higher than the highest model frequency, in order to

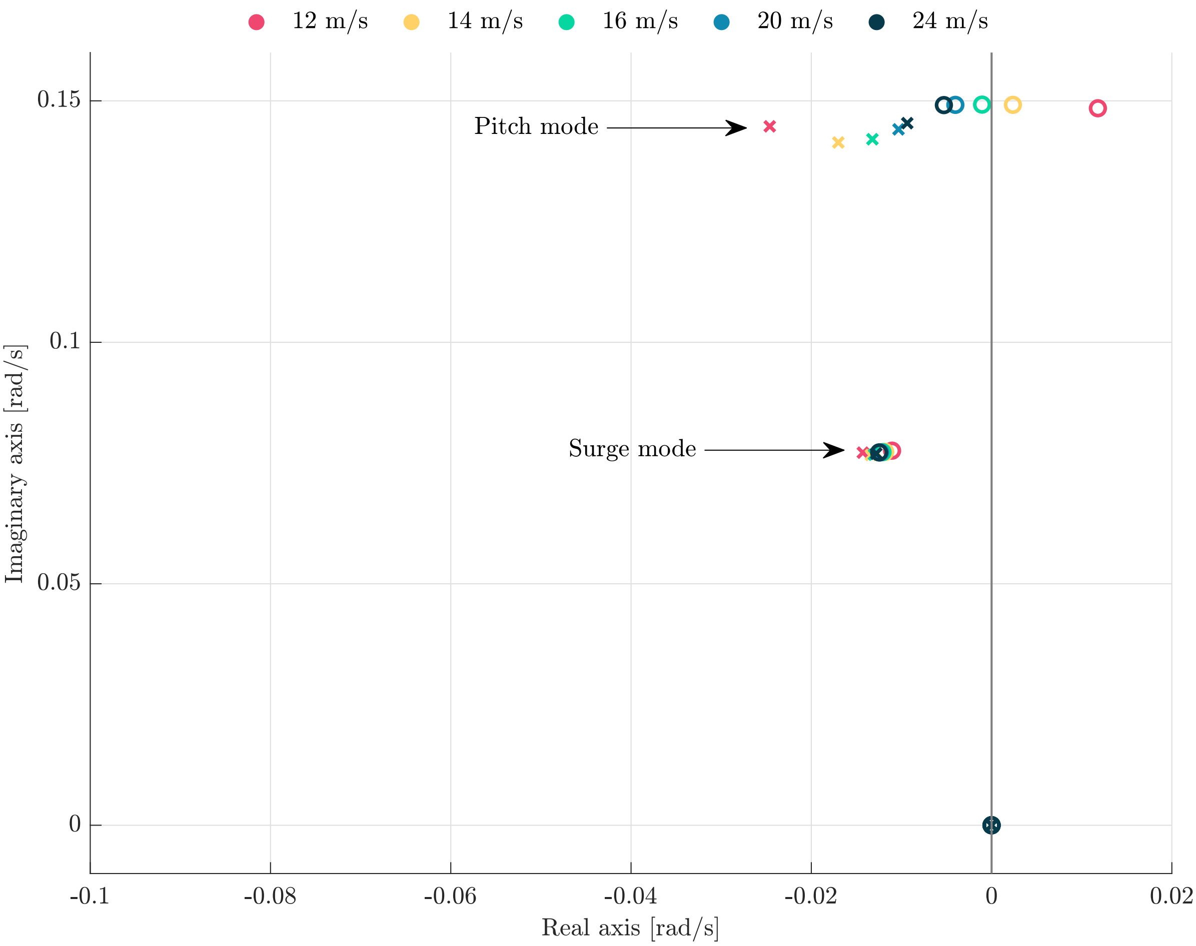

Figure 3.7: Pole-zero map of rotor speed against collective blade pitch, for several wind speeds above rated. The upper set of poles ($\times$) and zeroes (o) correspond to the pitch motion, whereas the lower set to the surge motion.

capture all the relevant modes without aliasing. The LTI discrete state-space system can then be expressed as

$$\begin{cases} \Delta x_{k+1} = & A_d \Delta x_k + B_d \Delta u_k + E_d \Delta d_k \\ \Delta y_k = & C \Delta x_k + D \Delta u_k \\ \Delta z_k = & C_z \Delta x_k + D_z \Delta u_k \end{cases} . \tag{3.16}$$

Note that the output and feedthrough matrices do not need to be discretized. On the other hand, if process noise is modelled, the noise covariance matrix must be discretized too.

Then, the simulation is performed by keeping the generator torque and collective blade pitch at the operating values, that is, $\Delta Q_{g,k} = \Delta \beta_{d,k} = 0 \quad \forall \quad k$, where k represents the current time step.

The collective blade pitch angle is fixed throughout the simulation, to the values shown in Table 3.4. To determine which value to use, a set of closed-loop simulations are performed at constant steady wind speed, and then the mean value of the blade pitch is taken, ignoring the transient part of the simulations.

Table 3.4: Steady-state values of collective blade pitch angle used for open-loop validation of the reduced order models against HAWC2 simulations.

Wind speed	12 m/s	14 m/s	16 m/s	20 m/s	24 m/s
Collective blade pitch angle	3.7346 deg	7.4933 deg	10.2912 deg	14.9627 deg	19.1358 deg

The results of the open-loop validation for the states' displacements and velocities at $V_\infty = 16$ m/s are shown in Figure 3.8 and Figure 3.9. The motions are captured adequately, specially the rotor speed and the platform pitch motion. The amplitude of the response after the step in wind speed is almost exactly the same, although higher frequency oscillations are observed in the surge, pitch and tower-top velocity responses, whereas not such vibrations appear in the simplified model, as they are caused by the tower fore-aft flexibility.

The natural frequencies are slightly different for the simplified model and the higher-fidelity HAWC2 case, which cause the signals to have a shift in frequency. This issue is addressed in subsection 3.5.1. The main reason is the use of a constant linear mooring line stiffness matrix, while the mooring line restoring forces are known to be non-linear. It can also be caused by mismatch in the inertial matrix.

Further analysis can be performed considering the energy content of the velocity signals. In Figure 3.10 the PSD of each velocity state is displayed, with the dashed, dotted and dashed-dotted line corresponding to the surge, pitch and heave natural frequencies respectively, as reported in [71]. The rotor speed shows two main contents, due to surge and pitch motions. The simplified model captures almost exactly the frequency and magnitude of the pitch component, however not so for the surge. This result is consistent with the surge, pitch and tower-top PSDs, where there is always a magnitude mismatch between the HAWC2 simulation and the simplified model. However, it is believed that since the main focus of the controller is to limit the pitch motions and track the rotor speed, the level of accuracy is good for the platform pitch and rotor speed, and sufficient for surge and tower-top.

Similar validation is conducted at various wind speeds, yielding equivalent results; however, these results are not presented here for the sake of conciseness.

3.5.1 Extended model open-loop validation

The extended model developed in section 2.4 is validated following analogously to the simplified model. The inclusion of tower flexibility leads to three new model parameters, the natural frequency and damping for the spring-damper system, and the mass of the DOF. The natural frequency is selected as the first natural frequency in fore-aft bending of the tower, $f_{t,b} = 0.5$ Hz. The damping has been tuned manually to match the open-loop response, leading to $\zeta_{t,b} = 0.1$. The mass is selected as the 75% of the tower mass and RNA.

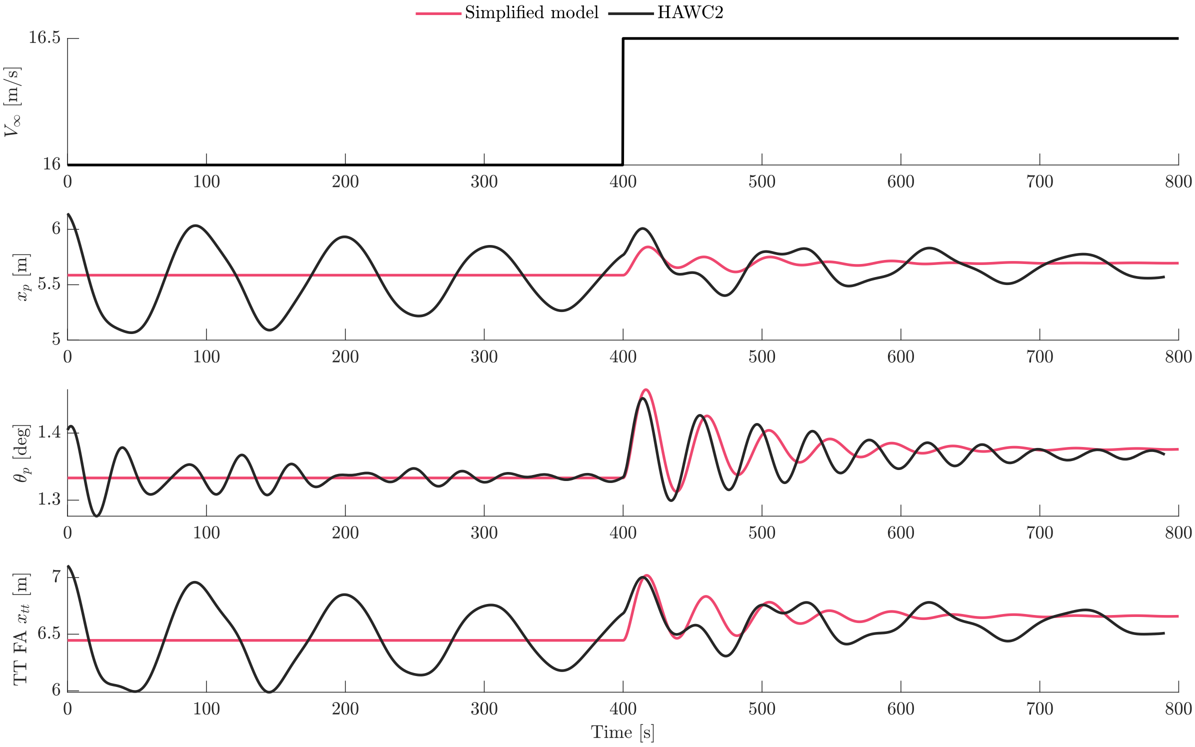

Figure 3.8: Simplified model open-loop validation for a steady wind speed of 16 m/s, and a step of 0.5 m/s. The generator torque is kept constant at the rated value, and the blade pitch angle is set at 10.3 deg. The wind speed and states' displacements are shown. The rotor azimuth is ignored for convenience.

Additionally, the error in the natural frequency of the system and motion damping is addressed by further tuning the mooring line stiffness and the viscous damping of the platform. It was found that an increase of 17% stiffness in all terms of K result in a great match of surge and pitch natural frequencies at $V_\infty = 16$ m/s. The viscous damping has been reduced, such that the settling time of the response is better represented. The drag coefficient from Morison's equation is reduced to a 40% in surge, 70% in pitch, 50% in pitch-to-surge, and 70% in surge-to-pitch.

In Figure 3.11 the extended and simplified model are compared to the HAWC2 simulation. It is clear that tuning the stiffness and the damping coefficients can significantly improve the accuracy of the model in the given conditions. It is also noticeable that the effect of the tower flexibility is very limited, as it can be better observed in Figure 3.12, leading to small oscillations, largest at the oscillation peak, as it could be expected from the resulting higher aerodynamic loads as the effective wind speed at the rotor increases.

Similarly to the previous case, a PSD analysis is performed and displayed in Figure 3.13 to investigate the accuracy of the response in the frequency domain. The response of the extended model is able to match better the magnitude of the platform pitch frequency in all states, thanks to further tuning the damping. Improvements can also be seen in the surge natural frequency. The tower natural frequency is not shown in the figure for

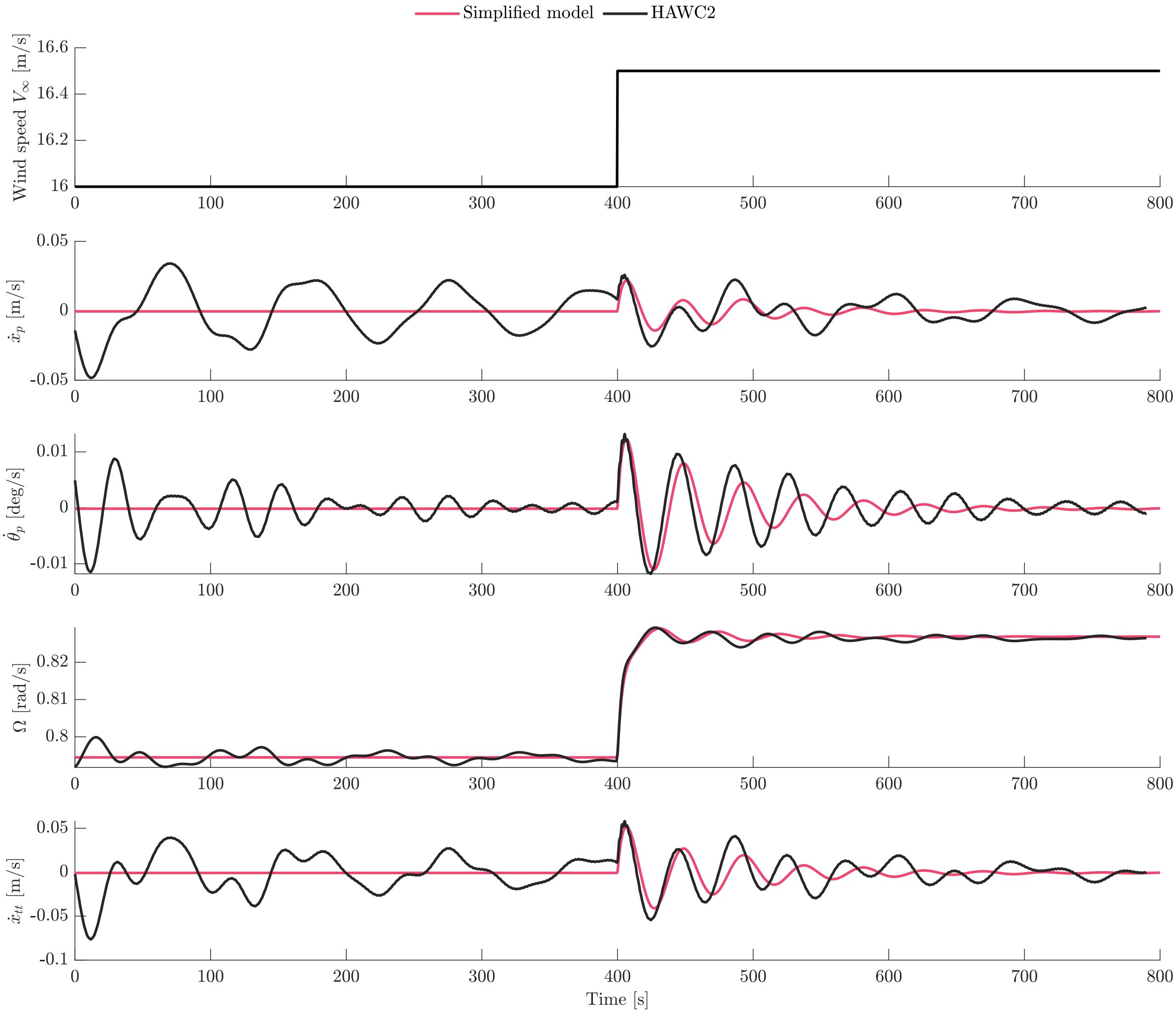

Figure 3.9: Simplified model open-loop validation for a steady wind speed of 16 m/s, and a step of 0.5 m/s. The generator torque is kept constant at the rated value, and the blade pitch angle is set at 10.3 deg. The states' velocities are shown.

readability, since the peak is barely noticeable for either HAWC2 and extended model.

3.6 Linear model closed-loop simulations

To further validate the behaviour of the model, a set of closed loop simulations are performed by coupling a baseline de-tuned PI controller. The controller used is the DTUWEC, partly described in 4.3.1.

The gains are de-tuned to reduce the controller's bandwidth, computed base on pole-placement (see chapter 4) at a frequency of 0.007 Hz (below the lowest platform natural frequency) and 0.7 critical damping. The gain values for the reduced order models are selected to match closely the HAWC2 response in rotor speed.

Figure 3.14 shows the results of a validation simulation for both the simplified and

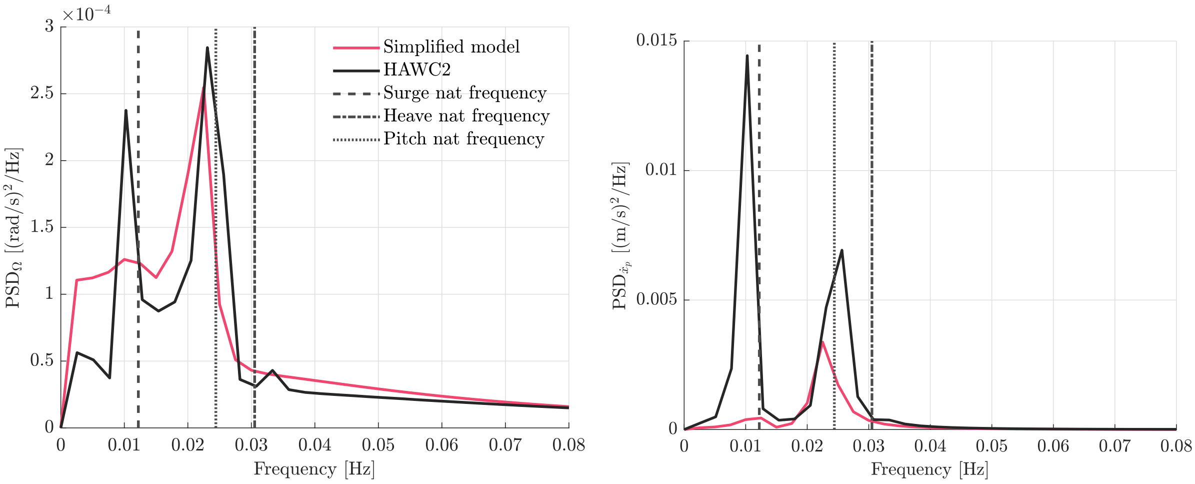

(a) Rotor Speed

(b) Platform surge velocity

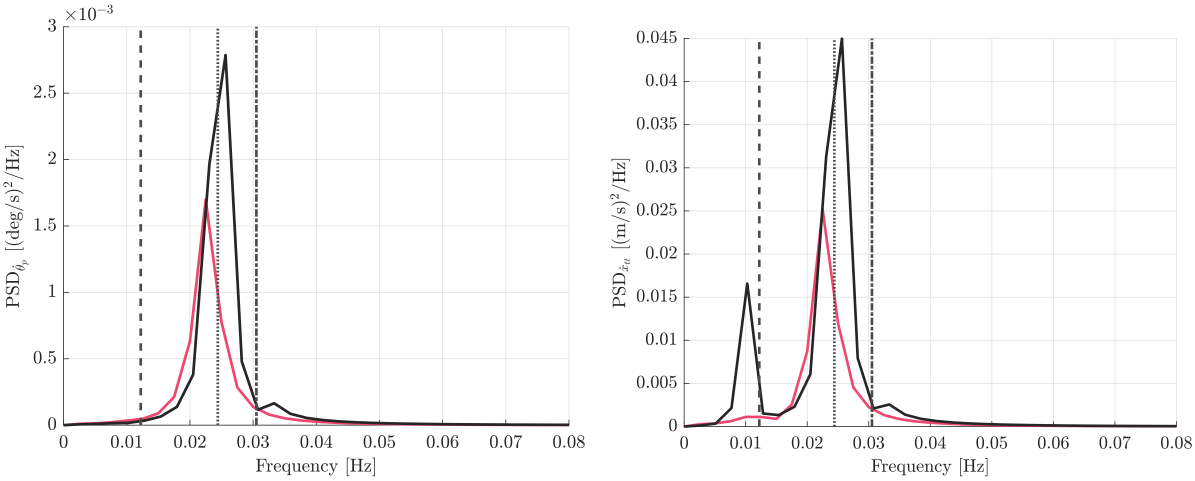

(c) Platform pitch velocity

(d) Tower-top fore-aft velocity

Figure 3.10: PSD of open-loop simulations. Comparison of HAWC2 and simplified model results for the states' velocities, at 16.5 m/s, after a 0.5 m/s step. The natural frequencies of the symmetric rigid body platform modes are plotted for convenience as reported in [71].

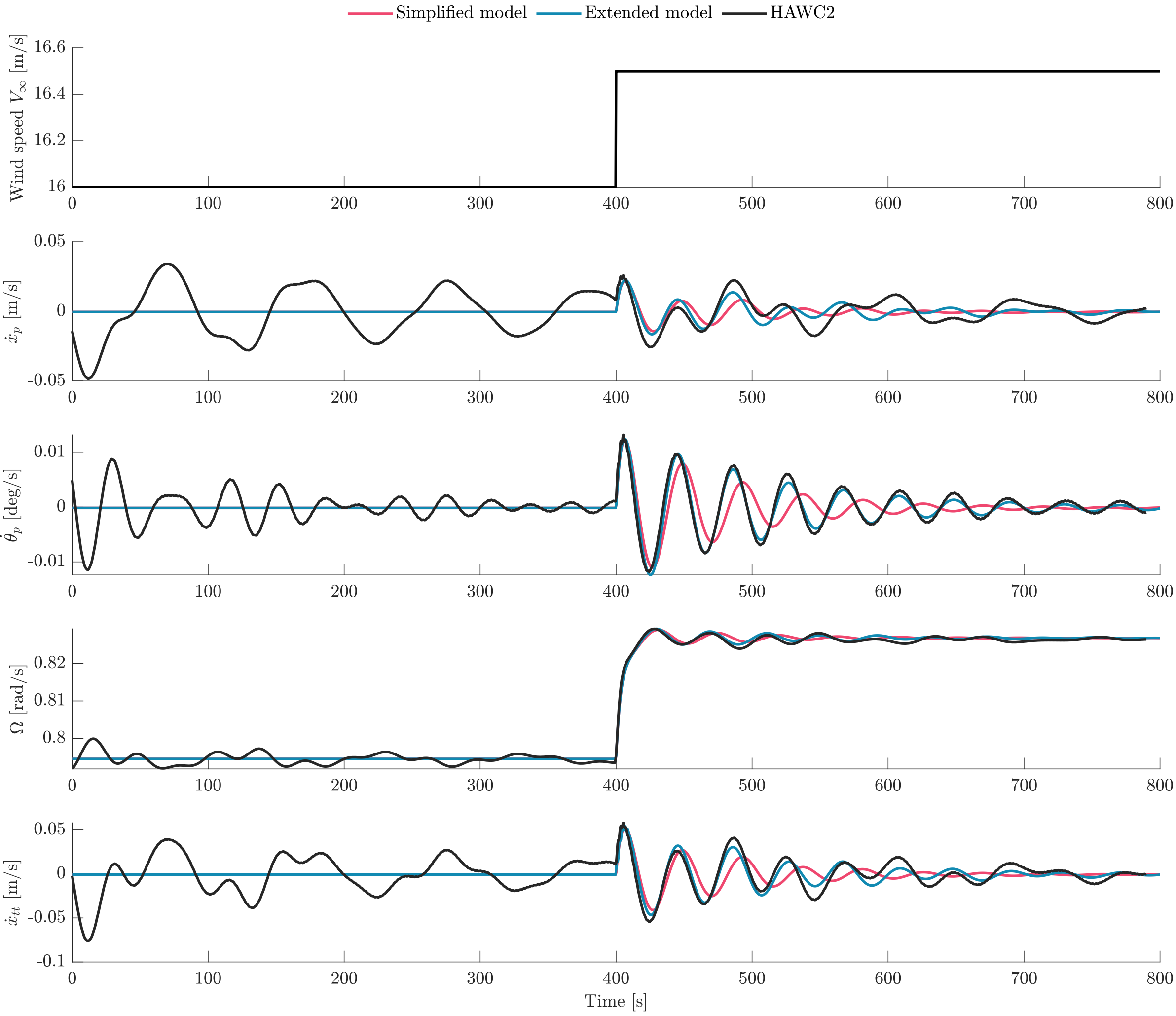

Figure 3.11: Extended model open-loop validation for a steady wind speed of 16 m/s, and a step of 0.5 m/s. The generator torque is kept constant at the rated value, and the blade pitch angle is set at 10.3 deg. The states' velocities are shown.

extended models. The response in the platform DOFs for the HAWC2 simulation shows a resonant behaviour, further inspection of the frequency response showed that the pitch frequency was excited by the controller, thus further de-tuning was clearly needed. This discrepancy in the response arises due to substantial oscillations existing prior to the wind speed step. Conversely, the reduced order models exhibit divergent behaviour, characterised by a significant increase in platform oscillations over time.

The demanded blade pitch for the simple models aligns closely with the mean value of HAWC2. The blade pitch step is more abrupt in these models, attributed to the absence of a low-pass filter in the implementation of the validation code. A better match could be attained with further development, however it falls out of the scope of this work.

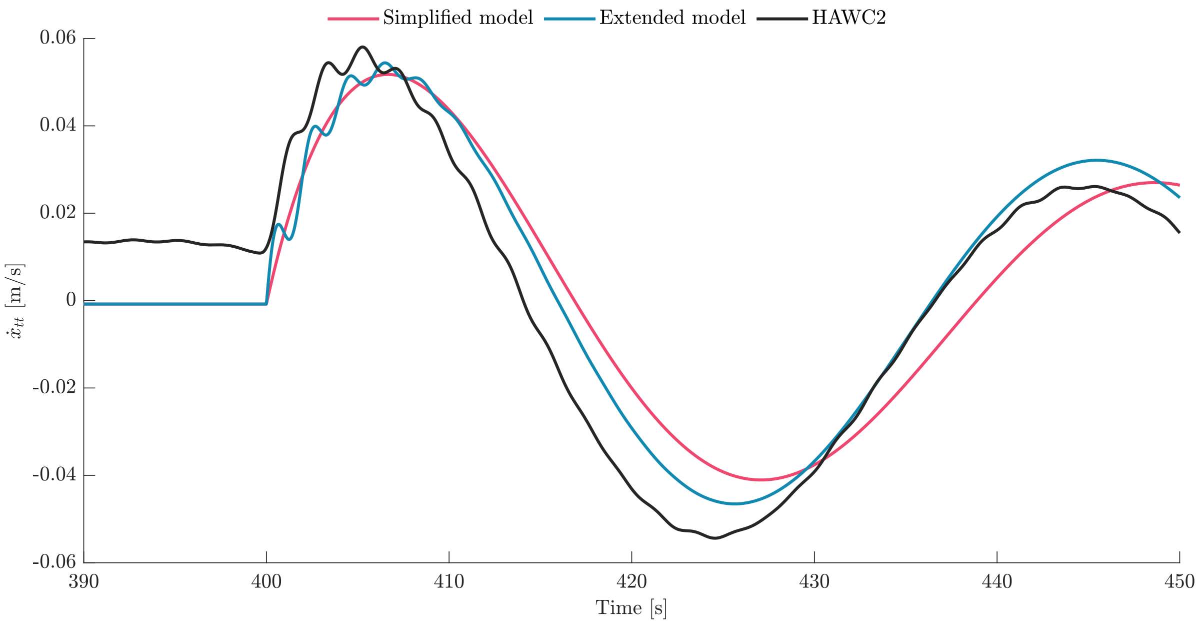

Figure 3.12: Extended model open-loop validation for a steady wind speed of 16 m/s, and a step of 0.5 m/s at $t = 400$ s. Tower-top velocity immediately before and after the step in wind speed.

3.7 Final remarks

Two of the models presented in chapter 2 have been implemented for the WindCrete SB concept with the IEA-15MW RWT. The parameters obtained from such concepts have been used to build the linear state-space model. Validation with HAWC2 simulations show that the reduced order models are able to capture the platform surge and pitch dynamics, as well as the rotor speed. Consideration has been given to the viscous damping, mooring line stiffness and aerodynamic derivatives, since they are highly non-linear, it is expected that the choice of operating points and calculation method will have a significant impact on the accuracy of the model.

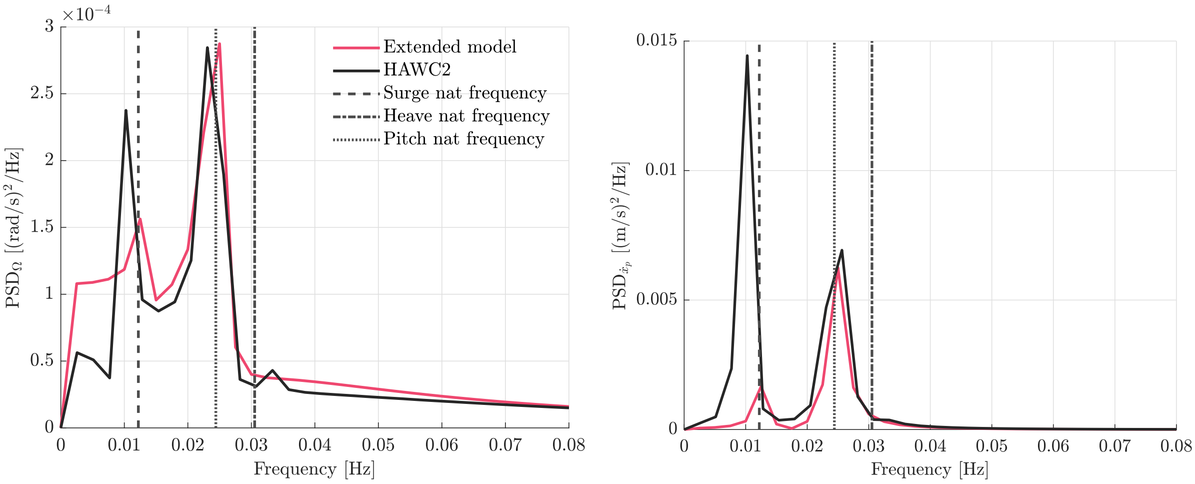

(a) Rotor Speed **(b)** Platform surge velocity

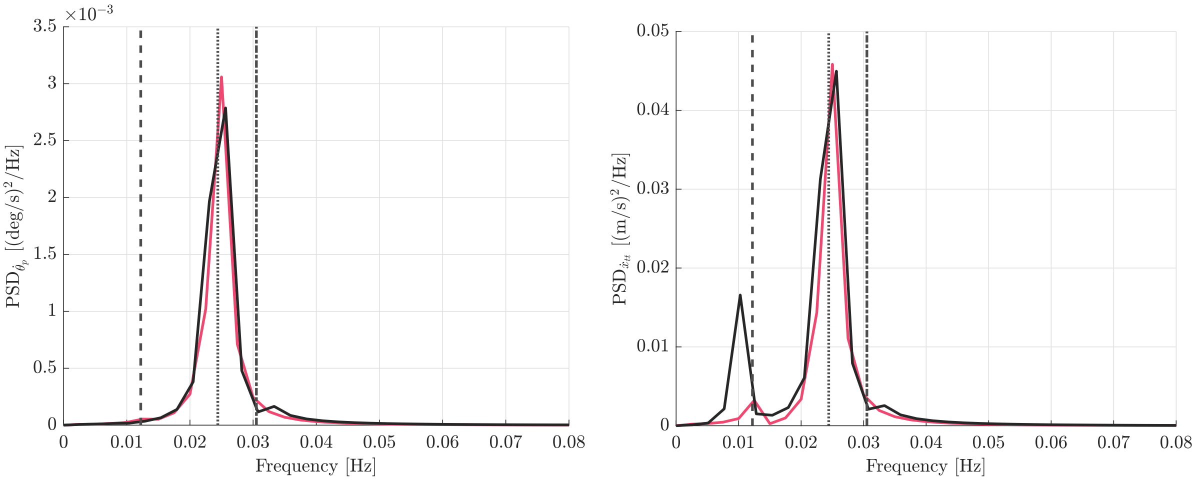

(c) Platform pitch velocity **(d)** Tower-top fore-aft velocity

Figure 3.13: PSD of open-loop simulations. Comparison of HAWC2 and extended model results for the states' velocities, at 16.5 m/s, after a 0.5 m/s step. The natural frequencies of the symmetric rigid body platform modes are plotted for convenience as reported in [71].

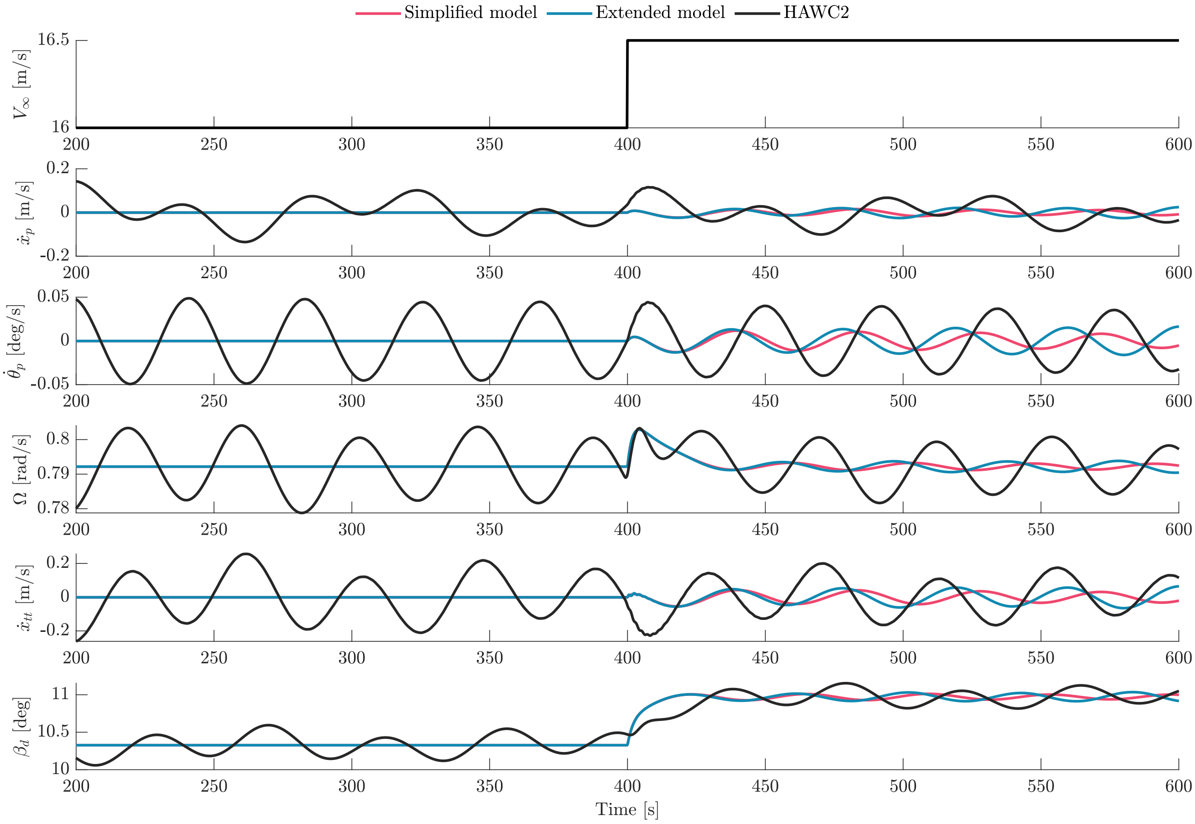

Figure 3.14: Extended and simplified models closed-loop validation for a steady wind speed of 16 m/s, and a step of 0.5 m/s. The generator torque is kept constant at the rated value, and the blade pitch angle is set based on a simple PI controller.

CHAPTER 4

Control design

The use of control techniques in the wind energy field can be divided into two levels, as shown in Figure 4.1. On one side, the wind farm level relates to the use of passive or active flow control within the wind farm to reduce the wake losses, increase the Annual Energy Production (AEP) and achieve load mitigation. Several approaches are being investigated in this field, such as the use of dynamic induction control, wake steering through active yawing of wind turbine rotors, or increasing the wake mixing through Individual Pitch Control in the Helix approach [74, 75]. On the other side, the individual control of wind turbines comprises the operational and the dynamic control.

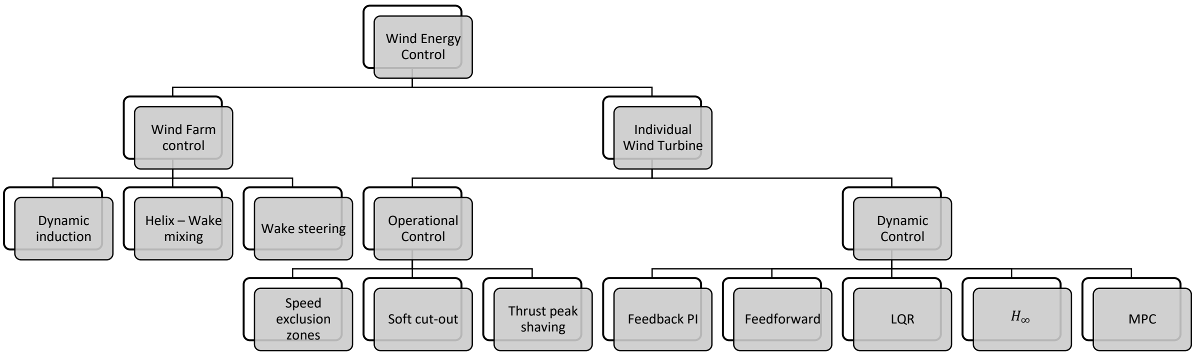

Figure 4.1: Summary of control research fields in wind energy.

The operational control, as defined in [76], manages supervision tasks such as connecting to the grid when conditions for power generation are met. It primarily uses averaged wind field and rotational speed measurements as inputs and makes decisions on transitioning the turbine between states, such as idling, starting up, power production, normal shutdown, and shutting down due to a malfunction.

Operational control plays a major role in the power production and loads of the wind turbine. To mitigate the latter while keeping high levels of energy harvesting, certain strategies have been proposed and studied, such as setting speed exclusion zones and performing soft cut-out or thrust-peak shaving.

The dynamic control part is the focus of the present work. It deals with the dynamic response of the turbine, subject to stochastic wind speed and gusts, waves and currents (in the case of floating wind turbines). The traditional approach consists of using a Proportional-Integral controller (PI) within a feedback loop to act on the rotor speed error. Feed-forward control has been proposed, but it requires measurements of the disturbances, such as the wind speed and wave heights, so that the controller reacts to them. More advanced control techniques have been researched, such as the use of Linear Quadratic Regulators (LQR) or H_∞ synthesis control. Finally, this thesis focuses on Model Predictive Control (MPC), which is covered in chapter 5.

The control design process can be segmented into a series of steps. Firstly, one should decide the objectives of the controller. Then, the control strategy can be set and finally, the algorithm can be developed.

Control challenges arise from the recent developments in the wind energy industry. On the one hand, the wind turbine sizes are rapidly increasing, which, as noted in [44], leads to lower tower and blade frequencies, thus drawing them closer to the controller bandwidth. On the other hand, the development of floating wind energy poses a challenge regarding new degrees of freedom as compared to bottom fixed technology and instabilities, such as the pitch instability explored in the introduction.

4.1 Control objectives

In literature, the operation range of a wind turbine is typically divided into several regions. These regions can be seen in Figure 4.2 for the IEA-15MW RWT. Region 1 corresponds to a fixed minimum rotor speed and non-optimal tip-speed ratio. Region 2 conveys operation at a constant optimum tip-speed ratio. Finally, region 3 extends from rated wind speed up to cut-out wind speed.

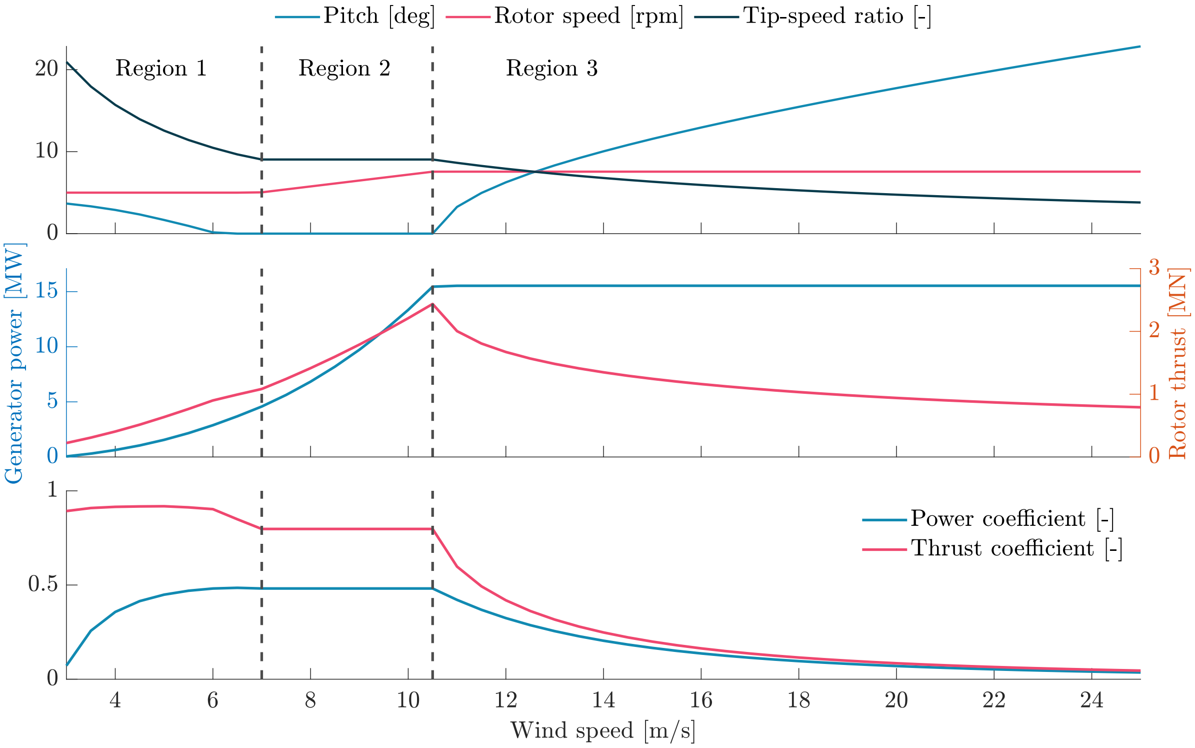

Figure 4.2: Steady-state operation curves of IEA15-MW RWT. The different control regions are delimited by dashed lines.

Generally, the control objectives depend on the operating region. For instance, region 2 is based on power maximisation, whereas region 3 is based on keeping the power or generator torque constant. An important objective common to all regions is load reduction; however, its importance is generally higher in operations near the rated wind speed as the thrust load reach their maximum value.

Furthermore, objectives such as maintaining the generator temperature, the rotor speed, or the tip deflection below a safety value should be considered throughout the controller design and evaluation [25].

4.2 Control of onshore and bottom-fixed offshore wind turbines

The aerodynamic power contained in the wind inflow depends on the rotor radius R, the atmospheric air density ρ and the undisturbed wind speed V_∞ given by the expression

$$P_{in} = \frac{1}{2}\rho\pi R^2 V_\infty^3 \,. \tag{4.1}$$

This power is partly extracted by the rotor, with an efficiency determined by the highly non-linear power coefficient $c_P(\lambda, \beta)$, which is dependent on the tip-speed ratio λ, and the blade pitch angle β. Thus, the generator power is given by

$$P_g = \eta_g c_P(\lambda, \beta) P_{in} \,, \tag{4.2}$$

where η_g represents the generator efficiency. The tip-speed ratio is defined as

$$\lambda = \frac{\Omega R}{V_\infty} \,. \tag{4.3}$$

Its optimum is found by the combination of design tip-speed ratio λ_{opt} and fine blade pitch angle $\beta_{d,opt}$, i.e. $c_{P,opt} = c_P(\lambda_{opt}, \beta_{opt})$. Both the fine pitch and design tip-speed ratio are kept constant throughout the partial load operation to maximise the power, except at low wind speeds. To achieve this, the generator torque is controlled by setting

$$Q_g\Omega = \frac{1}{2}\eta_g\rho\pi R^2 V_\infty^3 c_{P,opt} = \frac{1}{2}\eta_g\rho\pi c_{P,opt} R^5\Omega^3/\lambda_{opt}^3 \,, \tag{4.4}$$

leading to the following simple control law, depending only on the characteristics of the turbine and rotor speed measurements

$$Q_{g,opt} = \underbrace{\frac{\eta_g\rho\pi R^5 c_{P,opt}}{2\lambda_{opt}^3}}_{K_{opt}} \Omega^2 \,, \tag{4.5}$$

where K_{opt} is

$$K_{opt} = \frac{\eta_g\rho\pi R^5 c_{P,opt}}{2\lambda_{opt}^3} \,. \tag{4.6}$$

After the rated wind speed is reached, the blade pitch angle is used to control the wind turbine, with the objectives of keeping the power at its rated value and minimising the loads. A feedback loop is implemented where the rotor speed is measured and an error is computed, on which the PI controller acts. The tuning of the PI-controller gains is performed based on the drive train dynamics, which can be represented as shown in [16],

$$I_{dr}\dot{\Omega} + R_g Q_g + \alpha\Omega = Q_a(\Omega, V_r, \beta)\,, \tag{4.7}$$

where I_{dr} is the drive-train inertia, R_g represents the generator ratio, α is a proportional friction term, and Q_a is the aerodynamic torque. Ignoring the friction and considering no gearbox ratio (direct drive configuration), the equation can be rewritten as

$$I_{dr}\dot{\Omega} = Q_a(\Omega, V_r, \beta) - Q_g\,, \tag{4.8}$$

which was used in the simplified and extended models to represent the rotor (see chapter 2).

The aerodynamic torque can be linearised using a Taylor's first-order expansion, as it was shown in Equation 2.15.

Additionally, the generator torque depends on the rotor speed, therefore

$$Q_g = Q_{g,op} + \left.\frac{\partial Q_g}{\partial \Omega}\right|_{op} \Delta\Omega\,. \tag{4.9}$$

Substituting Equation 2.15 and Equation 4.9 to Equation 4.8, and considering that the operating aerodynamic torque should match the operating generator torque, $Q_{a,op} = Q_{g,op}$,

$$I_{dr}\Delta\dot{\Omega} = \left.\frac{\partial Q_a}{\partial \Omega}\right|_{op} \Delta\Omega + \left.\frac{\partial Q_a}{\partial V_r}\right|_{op} \Delta V_r + \left.\frac{\partial Q_a}{\partial \beta}\right|_{op} \Delta\beta - \left.\frac{\partial Q_g}{\partial \Omega}\right|_{op} \Delta\Omega\,. \tag{4.10}$$

The pitch PI controller operates by modifying the demanded blade pitch proportionally to the error in rotor speed with the reference, $e_\Omega = \Omega - \Omega_{ref} = \Delta\Omega$, and proportional of the integral error, $e_{I,k} = \int_{t_0}^{t} \Delta\Omega dt$, where k indicates discrete time step. Thus, the control action is given by

$$\Delta\beta = k_P \Delta\Omega + k_I \int_{t_0}^{t} \Delta\Omega dt\,. \tag{4.11}$$

By substituting Equation 4.11 into Equation 4.10, and neglecting the aerodynamic torque sensitivities to rotor speed and effective inflow speed, we can simplify the dynamic equation to a second-order ODE. Using this equivalence and employing a common technique called pole placement, we can compute the controller gains. This method allows us to set the desired frequency and damping of the system. The resulting equations for the gains are

$$\begin{cases} k_P = & \dfrac{2\zeta\omega I_{dr} - \left.\frac{\partial Q_g}{\partial \Omega}\right|_{op}}{-\left.\frac{\partial Q_a}{\partial \beta}\right|_{op}}\,, \\ k_I = & \dfrac{\omega^2 I_{dr}}{-\left.\frac{\partial Q_a}{\partial \beta}\right|_{op}}\,. \end{cases} \tag{4.12}$$

It is thus clear that the tuning of the gains depends on the aerodynamic sensitivities; for this reason, the PI gains are scheduled based on an operating variable, for instance, the blade pitch or the effective wind speed.

The selection of the pole's frequency, ω, and damping, ζ, is based on the natural frequencies of the system and the desired response. The frequency ω should be lower than the lowest natural frequency of the system, such that resonance can be avoided. The value of ζ shapes the response and can be tuned to match the requirements.

4.3 Control of floating offshore wind turbines

The main challenge in the control of floating wind turbines is the existing instability when applying traditional feedback control above rated wind speeds. As shown in Figure 1.3, the effect of an increase in wind velocity is the pitching of the blades. The thrust will decrease when the blades pitch towards the feather position as depicted in Figure 1.3b. Thus, the wind turbine tower-top will displace forward and the relative wind speed will increase with further pitching.

Clearly, from the pitch instability (see Figure 1.3), and as explained in [25], an onshore controller cannot be directly used for a floating offshore wind turbine without prior adjustment of the gains. Additionally, to increase the damping and limit platform motions, constant generator torque is employed in the above-rated region [35], leading to poor-quality, highly-varying generated power output.

This instability leads to contradictory control objectives, as stabilising the power leads to a system motion instability [27]. In the literature, a series of solutions have been proposed and outlined in section 1.1. The use of controller de-tuning and parallel compensation (tower-top velocity feedback loop) is considered in this work to provide a baseline controller to which the MPC is compared.

4.3.1 Baseline controller

The baseline controller used throughout the thesis for comparison is the DTU Wind Energy Controller (DTUWEC) [77]. The DTUWEC is an advancement of the Basic DTU Wind Energy Controller [78]. This fully open-source controller allows for the simulation of all IEC load cases. Some of the relevant features for the current work convey the smooth switching between partial and full load regions, which enhances the simulation efficiency by reducing the time duration of transients or the tower-top/drive-train dampers.

The controller implements a maximum power-point tracking strategy in the partial load region. That is, Equation 4.5. When the rated wind speed is achieved, the gain-scheduled blade-pitch PI controller regulates the rotor speed.

The application to FOWT demands that the gains are tuned for a lower frequency as compared to bottom-fixed/onshore applications. For that purpose, the HAWCStab2 pole-placement method is used to obtain the PI gains, resulting in stable operation by selecting the target natural frequency below the lowest system natural frequency at the expense of worsening the rotor speed tracking.

4.4 Parallel compensation

The use of parallel compensation has been analysed in [18, 66]. The baseline controller presented in section 4.3.1 can be further expanded by the addition of a feedback loop to compensate for the tower-top motion.

Two different approaches have been analysed in the literature. In [18], the tower-top velocity is used to compute a compensation collective blade pitch angle. However, this approach only yields improvements in small-scale FOWT, such as the one used for the experimental campaign. On the other hand, [66] uses torque compensation to limit the tower-top motion. The resulting control loop can be seen Figure 4.3.

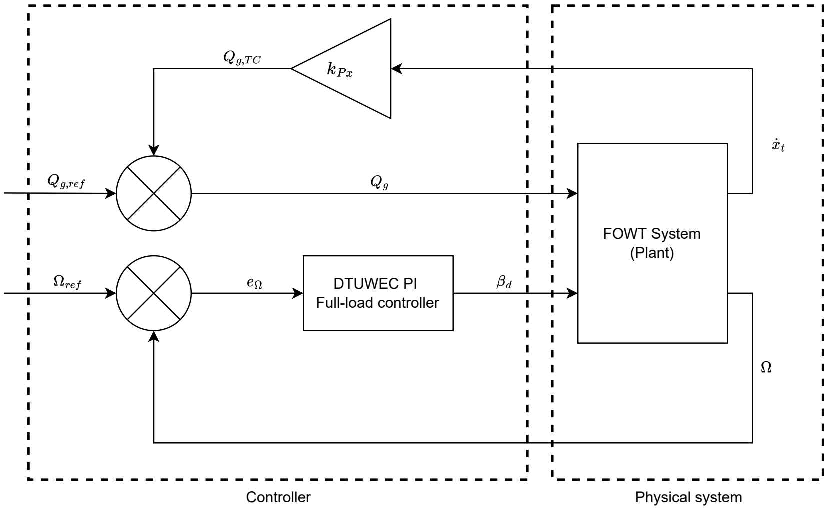

Figure 4.3: Parallel compensation control of FOWT using generator torque. Adapted from [66]

Using torque compensation allows for higher controller frequencies while maintaining stability. In [66], the simplifications made to obtain an expression for the PI gains, Equation 4.12, are revisited. The added degrees of freedom yields significant aerodynamic sensitivities $\partial Q_a/\partial\Omega$ and $\partial Q_a/\partial V_r$. The latter can be neglected since the disturbance does not need to be considered in the pole-placement process. However, the sensitivity to the rotor speed is important, therefore leading to the calculation of the modified gain,

$$\begin{cases} \tilde{k}_P = & \dfrac{2\zeta\omega I_{dr} + \frac{\partial Q_a}{\partial\Omega}\Big|_{op} - \frac{\partial Q_g}{\partial\Omega}\Big|_{op}}{-\frac{\partial Q_a}{\partial\beta}\Big|_{op}} \\ \tilde{k}_I = & \dfrac{\omega^2 I_{dr}}{-\frac{\partial Q_a}{\partial\beta}\Big|_{op}} \end{cases} . \tag{4.13}$$

Similar to the bottom-fixed case, the gains need to be scheduled based on the aerodynamic derivatives at different operating points.

CHAPTER 5

Implementation and tuning of Model Predictive Controllers

The Model Predictive Controller (MPC) implementation can be seen in Figure 5.1. The controller is coupled to a system, which can be divided into the plant and the sensors. The plant reacts to the given controller inputs u, the disturbances d, and the process noise w. These cause a change in the states x and the outputs z. Then, the sensors obtained measured quantities y_k, based on the system states and the sensors' inherent noise v.

The controller consists of the estimator and the regulator. The estimator utilises the measured quantities, and the known past controller input u_{k-1} to compute an estimate of the current state $\hat{x}_k$, associated to a certain probability $P_{k|k}$. The states' estimate is used by the regulator to solve an Optimal Control Problem (OCP), for which a controller input trajectory is found to track the current reference value $\bar{z}_k$ as closely as possible, while complying with the given constraints.

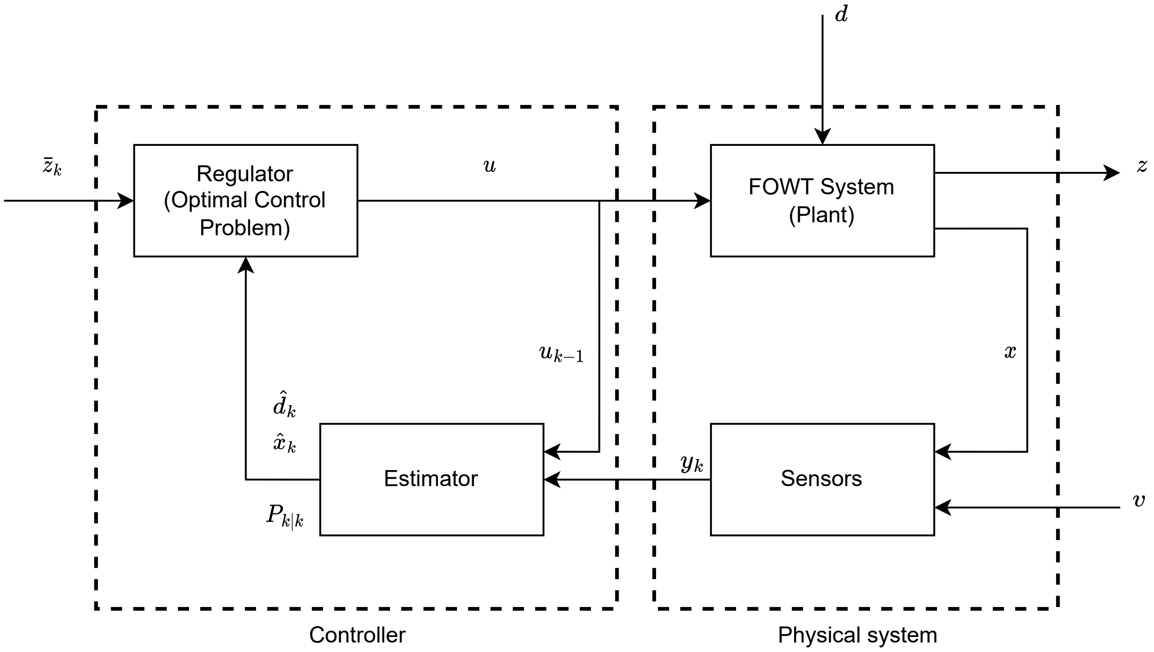

Figure 5.1: Diagram of a Model Predictive Controller coupled with a FOWT system.

5.1 Estimator design

The role of the estimator, sometimes referred to as the observer, is to provide an estimate of the current states $\hat{x}_k$ to the regulator. The estimate is based on the measurements conducted by the sensors y_k and the known controller inputs from the previous time steps u_{k-1}. The most common approach is the implementation of a Kalman filter [79].

The derivation considers the model in state space form

$$\begin{cases} \Delta x_{k+1} = A_d \Delta x_k + B_d \Delta u_k + E_d \Delta d_k + G_d w_k & \text{Process model} \ , \\ \quad \Delta y_k = C_d \Delta x_k + v_k & \text{Sensor function} \ , \\ \quad \Delta z_k = C_{z,d} \Delta x_k & \text{Output function} \ , \end{cases}$$

with the initial

$$\begin{cases} x_0 \sim N\left(0, P_0\right) & \text{Unknown initial state} \ , \\ w_k \sim N_{iid}(0, \bar{Q}) & \text{Process noise} \ , \\ v_k \sim N_{iid}(0, R) & \text{Measurement (sensor) noise} \ , \end{cases}$$

where P_0 is the covariance on the initial position of the states $\bar{Q}$ is the process noise covariance, and R is the sensor noise covariance. The process noise are defined as normally, identically and independently distributed N_{iid}.

5.1.1 Kalman filter

There are several types of Kalman filters that can be applied to estimate the states. The equations for the Kalman filter are derived based on the assumption of normally distributed states, measurements and noise. From that approach, the estimates of the states and the covariance can be computed.

The states and measurements are thus given by,

$$\begin{bmatrix} x \\ y \end{bmatrix} \sim N\left(\begin{bmatrix} \bar{x} \\ \bar{y} \end{bmatrix}, \begin{bmatrix} R_{xx} & R_{xy} \\ R_{yx} & R_{yy} \end{bmatrix} \right) . \tag{5.1}$$

Then, the estimate of x conditioned to the measurement y is denoted

$$\hat{x} = x | (y = y) \, , \tag{5.2}$$

and the variance would be

$$R_{\hat{x}} = R_{xx} - R_{xy} R_{yy}^{-1} R_{yx} \, . \tag{5.3}$$

The covariance of an state estimate can be computed based on the model and the noise covariances, and it is given by

$$\begin{aligned} P_{k+1|k} &= A P_{k|k-1} A' + G Q G' \\ &\quad - \left(A P_{k|k-1} C' + G S \right) \left(C P_{k|k-1} C' + R \right)^{-1} \left(A P_{k|k-1} C' + G S \right)' \, . \end{aligned} \tag{5.4}$$

Assuming that $P_{k+1|k} \to P$ for $k \to \infty$, then

$$P = APA' + GQG' - \left(APC' + GS\right) \left(CPC' + R\right)^{-1} \left(APC' + GS\right)' \, , \tag{5.5}$$

which is the Discrete Algebraic Riccati Equation (DARE). This equation can be solved offline (out of the time loop), and thus the innovation gains can be computed offline too, leading to the following formulation for the stationary Kalman filter,

$$\begin{aligned} R_e &= CPC' + R\,, & R_e &= \lim_{k\to\infty} R_{e,k}\,,\\ K_{fx} &= PC'R_e^{-1}\,, & K_{fx} &= \lim_{k\to\infty} K_{fx,k}\,,\\ K_{fw} &= SR_e^{-1}\,, & K_{fw} &= \lim_{k\to\infty} K_{fw,k}\,,\\ P_f &= P - K_{fx}R_eK'_{fx}\,, & P_f &= \lim_{k\to\infty} P_{k|k}\,,\\ Q_f &= Q - K_{fw}R_eK'_{fw}\,, & Q_f &= \lim_{k\to\infty} Q_{k|k}\,. \end{aligned} \tag{5.6}$$

However, the MATLAB built-in algorithms were not able to solve the equation. The most likely reason is that the system closed-loop eigenvalues are not within the unit circle of the complex plane, and therefore an stabilising solution does not exist. For that reason, the Dynamic Kalman Filter is used instead. Therefore, the Kalman filter gains need to be recomputed every time step.

The Dynamic Kalman Filter (DKF) follows the same principle as the stationary Kalman filter, with the difference that the covariance is updated at every time step $P_{k+1|k}$, and thus the Kalman filter gains as well. This increases the online computation time; however, it ensures a solution for the covariance, regardless of the linear state space model matrices.

In this case, the algorithm is implemented in the following two steps. First, the *measurement update* is computed,

$$\begin{aligned} R_{e,k} &= CP_{k|k-1}C^T + R\,,\\ K_{fx,k} &= P_{k|k-1}C^TR_{e,k}^{-1}\,,\\ K_{fw,k} &= SR_{e,k}^{-1}\,,\\ \hat{y}_{k|k-1} &= C\hat{x}_{k|k-1}\,,\\ e_k &= y_k - \hat{y}_{k|k-1}\,,\\ \hat{x}_{k|k} &= \hat{x}_{k|k-1} + K_{fx,k}e_k\,,\\ \hat{w}_{k|k} &= K_{fw,k}e_k\,. \end{aligned} \tag{5.7}$$

It can be noticed that the Kalman filter gains $K_{fx,k}$ and $K_{fw,k}$, are recomputed for every time step. Additionally, if there is no knowledge of the covariance of process and measurement noise S, it is impossible to estimate the process noise $\hat{w}_{k|k}$. After the estimate is computed, the controller will perform the control action u_k. The knowledge of this control action is used to compute the *one-step prediction (time update)*,

$$\begin{aligned} \hat{x}_{k+1|k} &= A_d\hat{x}_{k|k} + B_du_k + G_d\hat{w}_{k|k}\\ P_{k+1|k} &= A_dP_{k|k}A_d^T + GQ_{k|k}G^T - A_dK_{fx,k}S^TG^T - GSK_{fx,k}^TA_d^T\,. \end{aligned} \tag{5.8}$$

The covariance P is updated at every time step and used to recompute the gains, as shown earlier.

It is important to notice that the disturbances have not been included in the previous algorithm. An advanced formulation of the Kalman filter, the augmented Kalman filter, should be used to estimate the disturbances. Knowledge of the disturbances is crucial for the MPC implementation in any process, and especially in stochastic systems, such as a FOWT, due to the wind speed and wave load variations over time.

The formulation of the Augmented Dynamic Kalman Filter (ADKF) is based on extending the linear state-space formulation by including the disturbances as states, that is,

$$x_a = [x, d]^T \ , \tag{5.9}$$

leading to augmented system matrices,

$$\begin{aligned} A_a &= \begin{bmatrix} A_d & E_d \\ 0 & I \end{bmatrix}, & B_a &= \begin{bmatrix} B_d \\ 0 \end{bmatrix}, & C_a &= \begin{bmatrix} C_d \\ 0 \end{bmatrix}, \\ G_a &= \begin{bmatrix} G_d & 0 \\ 0 & I \end{bmatrix}, & S_a &= \begin{bmatrix} S \\ 0 \end{bmatrix}, & Q_a &= \begin{bmatrix} Q_d & 0 \\ 0 & I \end{bmatrix}. \end{aligned}$$

Using the previous augmented matrices, the measurement update provides an estimate of the augmented states for the current time step,

$$\begin{aligned} R_{e,k} &= C_a P_{k|k-1} C'_a + R \, , \\ K_{fx,k} &= P_{k|k-1} C'_k R_{e,k}^{-1} \, , \\ K_{fw,k} &= S R_{e,k}^{-1} \, , \\ \hat{y}_{k|k-1} &= C \hat{x}_{k|k-1} \, , \\ e_k &= y_k - \hat{y}_{k|k-1} \, , \\ \hat{x}_{k|k} &= \hat{x}_{k|k-1} + K_{fx,k} e_k \, , \\ \hat{w}_{k|k} &= K_{fw,k} e_k \, . \end{aligned} \tag{5.10}$$

The time update is performed using the augmented matrices and the augmented states' estimate,

$$\begin{aligned} \hat{x}_{a,k+1|k} &= A_a \hat{x}_{k|k} + B_a u_k + G_a \hat{w}_{k|k} \, , \\ P_{k+1|k} &= A_a P_{k|k} A_a^T + G_a Q_{a,k|k} G_a^T - A_a K_{fx,k} S_a^T G_a^T - G_a S_a K_{fx,k}^T A_a^T \, . \end{aligned} \tag{5.11}$$

5.1.2 Observer validation

The DKF and ADKF are tested against a closed-loop turbulent wind simulation performed with HAWC2 in order to understand whether it can be applied to the current case. In this case, the measurements assumed are the rotor speed Ω, the platform pitch velocity $\dot{\theta}_p$, and platform pitch displacement θ_p. This assumption aligns with [42], where an Inertial Measurement Unit is considered to be able to track the platform motions, whereas the rotor speed is commonly measured for variable-speed WTGs. To each measurement sample, white noise v_k is added.

The results can be seen in Figure 5.2 and Figure 5.3, for the displacements and velocities, respectively. No wind speed prediction is performed for the wind speed with the DKF; however, it is predicted when using ADKF. The result matches fairly well the trends, but it is unable to capture the high-frequency fluctuations. The model used considers the rotor forces under steady conditions without any dynamic effects. Additionally, the rotor is assumed as the point force acting on the hub, therefore causing a filtering effect on the turbulent wind field. Future improvements could be achieved by increasing the number of degrees of freedom of the rotor, such as including a model for the blades or considering a dynamic inflow model.

The surge displacement prediction using DKF contains a pitch frequency caused by the error in capturing the platform pitch displacement, leading to a poor estimation of the platform motions. Augmenting the Kalman filter clearly improves the performance, especially regarding the platform pitch, and marginally for the surge, which contains only an error matching the surge natural frequency. This error is propagated to the tower-top displacement since it is modelled as a linear relation between surge and pitch.

The velocity predictions using ADKF are significantly better than DKF, with marginal error on the surge velocity and sensor noise for the rotor speed and platform pitch velocity. On the other hand, the DKF is not able to capture correctly the velocities of any state.

5.2 Regulation problem

The regulator task is to compute an optimal controller input based on the state's knowledge, the reference set-point, the previous inputs and the disturbance, if it has been estimated. Since not all states are generally measurable, the Kalman filter is needed to provide an estimate, as it has been shown in section 5.1. Additionally, knowledge of the disturbances is necessary to achieve offset-free control; therefore, the need to extend the Kalman filter to estimate the incoming wind speed since accurate measurements are rarely available.

The objective of the regulator is to solve an optimal control problem over a finite time horizon, usually known as the prediction or receding horizon. Additionally, a control horizon shorter than the prediction horizon can be defined, such that the optimal control actions u_{k+i} are computed for a shorter period of time, and the remaining period they are assumed constant, as it can be seen in Figure 5.4. This could be beneficial to reduce computational effort or if the model is not able to provide accurate predictions over long time periods. However, the control horizon is defined as the same length as the prediction horizon for the current work for simplicity.

5.2.1 Unconstrained MPC

The first step in designing an MPC regulator is to define the optimization problem. For simplicity, this can be considered to minimise an objective function defined by the

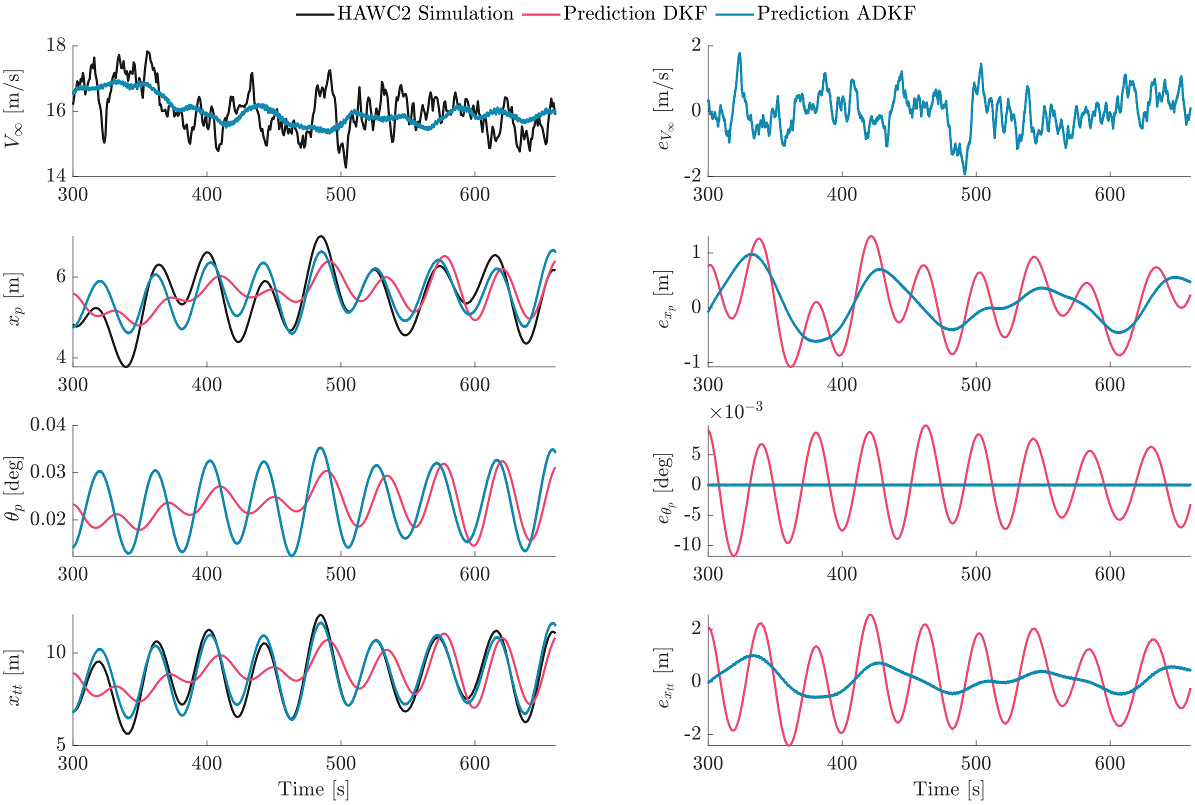

Figure 5.2: DKF and ADKF validation for a turbulent wind simulation in HAWC2, with $\bar{V}_\infty = 16$ m/s and $TI = 4\%$. Comparison of simulation wind speed and displacements with both DKF and ADKF prediction. The left-hand side corresponds to the displacements' estimation, whereas the right-hand side is the absolute error computed between the prediction and the HAWC2 simulation.

least-squares of the outputs with respect to the reference set points. In mathematical terms, it is formulated as

$$\min_u \phi = \frac{1}{2} \sum_{k=1}^{N} \|z_k - \bar{z}_k\|^2_{Q_z} \,, \tag{5.12}$$

where ϕ is the objective function, formulated as a least-squares problem. The set-point at each time step $\bar{z}_k$ is compared with the output variable z_k over the receding horizon of length N. A weight is given for each computed error at each time step $z_k - \bar{z}_k$, by a matrix Q_z. The objective function is evaluated over the length of the horizon N to compute the optimum trajectory of the controller inputs u. Note that no terminal cost is added for simplicity.

Considering the LTI discretized state-space representation shown in Equation 3.16, the output variable for the following time steps $k + i$ can be written as

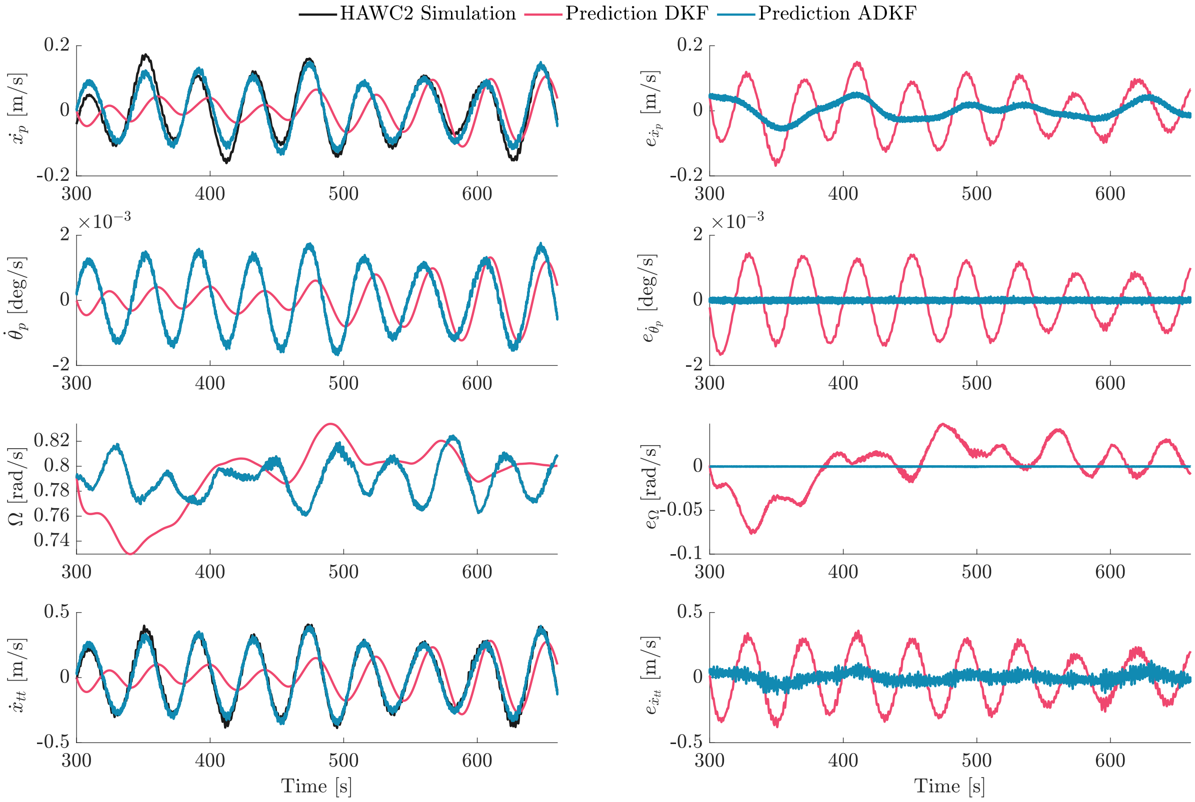

Figure 5.3: DKF and ADKF validation for a turbulent wind simulation in HAWC2, with $\bar{V}_\infty = 16$ m/s and $TI = 4\%$. Comparison of states' velocities with both DKF and ADKF prediction. The left-hand side corresponds to the displacements' estimation, whereas the right-hand side is the absolute error computed between the prediction and the HAWC2 simulation.

$$
\begin{aligned}
\Delta z_{k+1} = C_z \Delta x_{k+1} &= C_z \left(A_d \Delta x_k + B_d \Delta u_k + E_d \Delta d_k \right) , \\
\Delta z_{k+2} = C_z \Delta x_{k+2} &= C_z \left(A_d \Delta x_{k+1} + B_d \Delta u_{k+1} + E_d \Delta d_{k+1} \right) , \\
&\vdots \\
\Delta z_{k+i} = C_z \Delta x_{k+i} &= C_z \left(A_d \Delta x_{k+i-1} + B_d \Delta u_{k+i-1} + E_d \Delta d_{k+i-1} \right) , \\
&\vdots \\
\Delta z_{k+N} = C_z \Delta x_{k+N} &= C_z \left(A_d \Delta x_{k+N-1} + B_d \Delta u_{k+N-1} + E_d \Delta d_{k+N-1} \right) .
\end{aligned}
\tag{5.13}
$$

Introducing recursively the value of Δx_{k+i-1} will result in an expression for the output variable across the receding horizon dependent on the initial states, and both the chosen controller inputs and the disturbances at each time step, with the form

$$
\Delta z_{k+i} = C_z A_d^i \Delta x_k + \sum_{j=0}^{i-1} \underbrace{C_z A_d^{i-1-j} B_d}_{H_i} \Delta u_{k+j} + \sum_{j=0}^{i-1} \underbrace{C_z A_d^{i-1-j} E_d}_{H_{d,i}} \Delta d_{k+j} , \tag{5.14}
$$

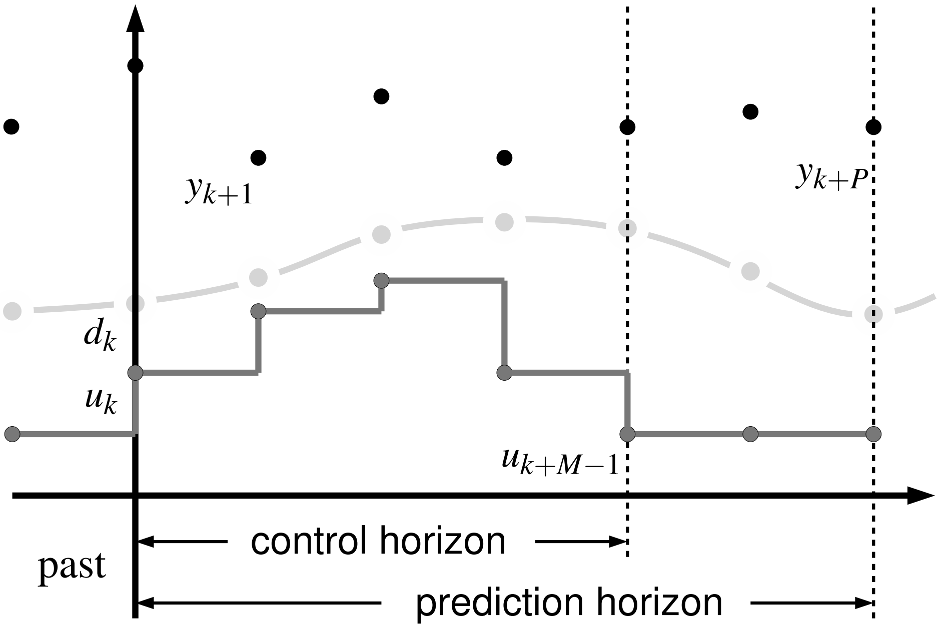

Figure 5.4: MPC optimization over a finite horizon. Reprinted from [29].

where the matrices H_i are known as the impulse response coefficients, or Markov parameters, whereas $H_{d,i}$ are their disturbance counterpart. Equation 5.14 can be generalised for all time steps in the receding horizon as

$$\begin{aligned} \underbrace{\begin{bmatrix} z_1 \\ z_2 \\ z_3 \\ \vdots \\ z_N \end{bmatrix}}_{Z} = \underbrace{\begin{bmatrix} C_zA \\ C_zA^2 \\ C_zA^3 \\ \vdots \\ C_zA^N \end{bmatrix}}_{\Phi} x_k &+ \underbrace{\begin{bmatrix} H_1 & 0 & 0 & \dots & 0 \\ H_2 & H_1 & 0 & \dots & 0 \\ H_3 & H_2 & H_1 & & 0 \\ \vdots & \vdots & \vdots & & \vdots \\ H_N & H_{N-1} & H_{N-2} & \dots & H_1 \end{bmatrix}}_{\Gamma} \underbrace{\begin{bmatrix} u_0 \\ u_1 \\ u_2 \\ \vdots \\ u_{N-1} \end{bmatrix}}_{U} \\ &+ \underbrace{\begin{bmatrix} H_{d,1} & 0 & 0 & \dots & 0 \\ H_{d,2} & H_{d,1} & 0 & \dots & 0 \\ H_{d,3} & H_{d,2} & H_{d,1} & & 0 \\ \vdots & \vdots & \vdots & & \vdots \\ H_{d,N} & H_{d,N-1} & H_{d,N-2} & \dots & H_{d,1} \end{bmatrix}}_{\Gamma_d} \underbrace{\begin{bmatrix} d_0 \\ d_1 \\ d_2 \\ \vdots \\ d_{N-1} \end{bmatrix}}_{D}, \end{aligned} \tag{5.15}$$

which in a more compact form,

$$Z = \Phi x_k + \Gamma U + \Gamma_d D\,, \tag{5.16}$$

where Z contains the outputs at each time step Φ is a matrix coming from the first element at the right-hand side of Equation 5.14, x_k is the *initial* state for the current evaluation of the receding horizon. Then Γ is a lower-diagonal matrix containing the

Markov parameters; similarly, Γ_d contains the disturbance Markov parameters. U and D contain the controller inputs and disturbances for all steps within the receding horizon.

The objective function can now be expressed as

$$\phi = \frac{1}{2}\sum_{k=1}^{N} \|z_k - \bar{z}_k\|_{Q_z}^2 = \|\Gamma U + \underbrace{(\Phi x_k + \Gamma_d D - \bar{Z})}_{-b}\|_{Q_z}^2 \,. \tag{5.17}$$

The optimization of such objective function can be performed using the gradient, as long as H and H_d are positive definite, that is

$$\nabla\phi = 0, \quad \text{and} \quad \nabla^2\phi \geq 0 \,. \tag{5.18}$$

The objective function can be expressed as a Quadratic Program (QP)

$$\phi = \frac{1}{2}U^T H U + g^T U + \rho \,, \tag{5.19}$$

where the Hessian and the g and ρ terms are defined as

$$\begin{aligned} H = &\ \Gamma^T Q_z \Gamma \,, \\ g = &\ -\Gamma^T Q_z b \,, \\ \rho = &\ \tfrac{1}{2} b^T Q_z b \,. \end{aligned} \tag{5.20}$$

Considering no constraints, the solution to the optimization problem is directly given by

$$\nabla\phi = HU + g = 0 \,, \tag{5.21}$$

and solving for U,

$$U = -H^{-1} g \,. \tag{5.22}$$

The vector U contains the optimal trajectory, computed based on the model, the current estimate of the states, the previous controller input, and the estimate or knowledge of the disturbances, if any. From this vector, only the first element is used u, and it is recomputed at each time step, as shown in Figure 5.1. Note that the inverse of the Hessian should only be used with QP algorithms; for an analytical solution, the Cholesky decomposition should be used, such as to avoid wrong solutions due to an ill-posed problem [22].

5.2.2 Input penalties

A penalty can be added on the rate of change of blade pitch demand $\Delta\beta_d$, and on the generator torque $\Delta\beta_d$, by defining the following objective function term,

$$\phi_{\Delta u} = \frac{1}{2}\sum_{k=1}^{N} \|\Delta u_k\|_{S_{\Delta u}}^2 \,, \tag{5.23}$$

where $S_{\Delta u}$ is the penalty weight. The rate of change of the input is defined as $\Delta u_k = u_k - u_{k-1}$, thus, the objective function $\phi_{\Delta u}$ can be rewritten as

$$
\begin{aligned}
\phi_{\Delta u} = & \frac{1}{2}\begin{bmatrix} u_0 \\ u_1 \\ \vdots \\ u_N \end{bmatrix}^T \underbrace{\begin{bmatrix} 2S_{\Delta u} & -S_{\Delta u} & & & \\ -S_{\Delta u} & 2S_{\Delta u} & -S_{\Delta u} & & \\ & -S_{\Delta u} & \ddots & \ddots & \\ & & \ddots & 2S_{\Delta u} & -S_{\Delta u} \\ & & & -S_{\Delta u} & S_{\Delta u} \end{bmatrix}}_{H_S} \begin{bmatrix} u_0 \\ u_1 \\ \vdots \\ u_N \end{bmatrix} + \\
& \left(- \begin{bmatrix} S_{\Delta u} \\ 0 \\ \vdots \\ 0 \end{bmatrix} u_{-1} \right)^T \begin{bmatrix} u_0 \\ u_1 \\ \vdots \\ u_N \end{bmatrix} + \frac{1}{2} u_{-1} S_{\Delta u} u_{-1} \, .
\end{aligned}
\tag{5.24}
$$

In this work, the generator torque is generally assumed constant and, thus, $S_{\Delta u} = S_{\Delta \beta_d}$, that is, a single parameter is used to tune the penalty term of the objective function. Augmenting the controlled variables to include the generator torque leads to a new tuning parameter, that is, the penalty to the rate of change of Q_g, thus

$$
S_{\Delta u} = \begin{bmatrix} S_{\Delta \beta_d} & 0 \\ 0 & S_{\Delta Q_g} \end{bmatrix} . \tag{5.25}
$$

The tuning of the penalty $S_{\Delta Q_g}$ is slightly more challenging due to the great difference in orders of magnitude between the demanded blade pitch $o(\Delta \beta_d) \sim 10^0$ deg, and the generator torque $o(\Delta Q_g) \sim 10^7$ $\mathrm{N \cdot m}$. To account for that fact, the ratio between penalties should be $S_{\Delta Q_g} / S_{\Delta \beta_d} \sim 10^{-8}$, such that the resulting controller is able to combine both actions with a significant impact. The tuning of this penalty is explored later on.

5.3 MPC tuning

The MPC tuning process for onshore and bottom-fixed wind turbines is discussed in [80, 81]. The first approach involves determining sensitivity tables between changes in weights and their impact on the KPIs explicitly specified in the objective function. While this approach is valuable, it's constrained by system non-linearities, as the selected points for sensitivity calculation can significantly influence the outcomes. This becomes clearer upon reviewing the findings of this study.

In contrast, [81] introduces a tuning method that constructs Pareto fronts by varying a set of weights based on a tuning parameter that defines their proportions. The chosen KPIs are then standardised using a baseline controller. The Pareto fronts allow for the trade-offs to be presented in an accessible manner, facilitating the comparison of affected parameters. This strategy permits the selection of desired weight values by considering explicit trade-offs and visualising non-linearities that emerge across the range of analysed weights. However, this method demands greater computational effort due to the need for numerous weight combinations to create meaningful Pareto fronts.

Regarding floating offshore wind turbines (FOWT), the rationale behind tuning choices is often undisclosed. In [34], weight adjustments are made to align controller performance with rotor speed tracking and motion minimisation. For other works cited in this thesis, there is no mention of the trade-offs taken into account.

To the author's knowledge, no specific methodology for tuning MPC tailored to FOWT wind turbines has been proposed. Consequently, this study adopts the approach outlined by [81] as a foundation, expanding it to include several pertinent parameters affecting FOWT performance. The utilisation of Pareto fronts is combined with the examination of time-series and power-spectral density (PSD) plots to foster a deeper comprehension of the interplay between KPIs.

5.3.1 Receding horizon length

The receding horizon length N must be tuned such that the predictions used to optimize the controller action capture the relevant phenomena. In this case, since the pitch platform motion is to be minimised, and its natural frequency is significantly low, the receding horizon should be as long as the platform pitch motion. However, increasing N will inevitably lead to higher computation time, and therefore, a trade-off must be found between performance and computation effort. It is noted that the control horizon and prediction horizon have the same length, such as to simplify the implementation.

Figure 5.5 shows the effect on steady simulations of N values between 50 and 500, corresponding to between 5 s and 50 s duration. It is evident that a low receding horizon length $N = 50, 100$ leads to undesired oscillations at the platform pitch natural frequency. These frequencies disappear partly for $N = 250$, and practically completely for $N = 500$. One of the possible reasons is that the horizon length does not cover a significant portion of the platform pitch motion. Furthermore, the use of terminal cost in the objective function could potentially improve the controller performance by adding a larger weight at the last time step in order to ensure the optimal solution eliminates the error, however, this aspect falls out of the scope of the current work. It is, therefore, chosen to proceed with the value of $N = 500$ for the following tuning steps.

5.3.2 Objective function weights

The weights in the objective function should be tuned according to the controller's priorities. One of the advantages of MPC is its intuitive tuning procedure compared to a PI controller, as the weights directly correspond to controller objectives.

Three distinct simulation approaches have been employed to fine-tune the weights and penalties. These approaches include simulations involving steady wind conditions, a step change in wind speed, and turbulent wind scenarios, each leading to different tuning solutions. In the steady wind simulations, oscillations stem from the wind speed ramp-up, utilising the DTUWEC PI detuned controller. This is followed by an abrupt transition to Unconstrained MPC (UMPC) operation at $t = 250$ s. In the step wind simulations, the

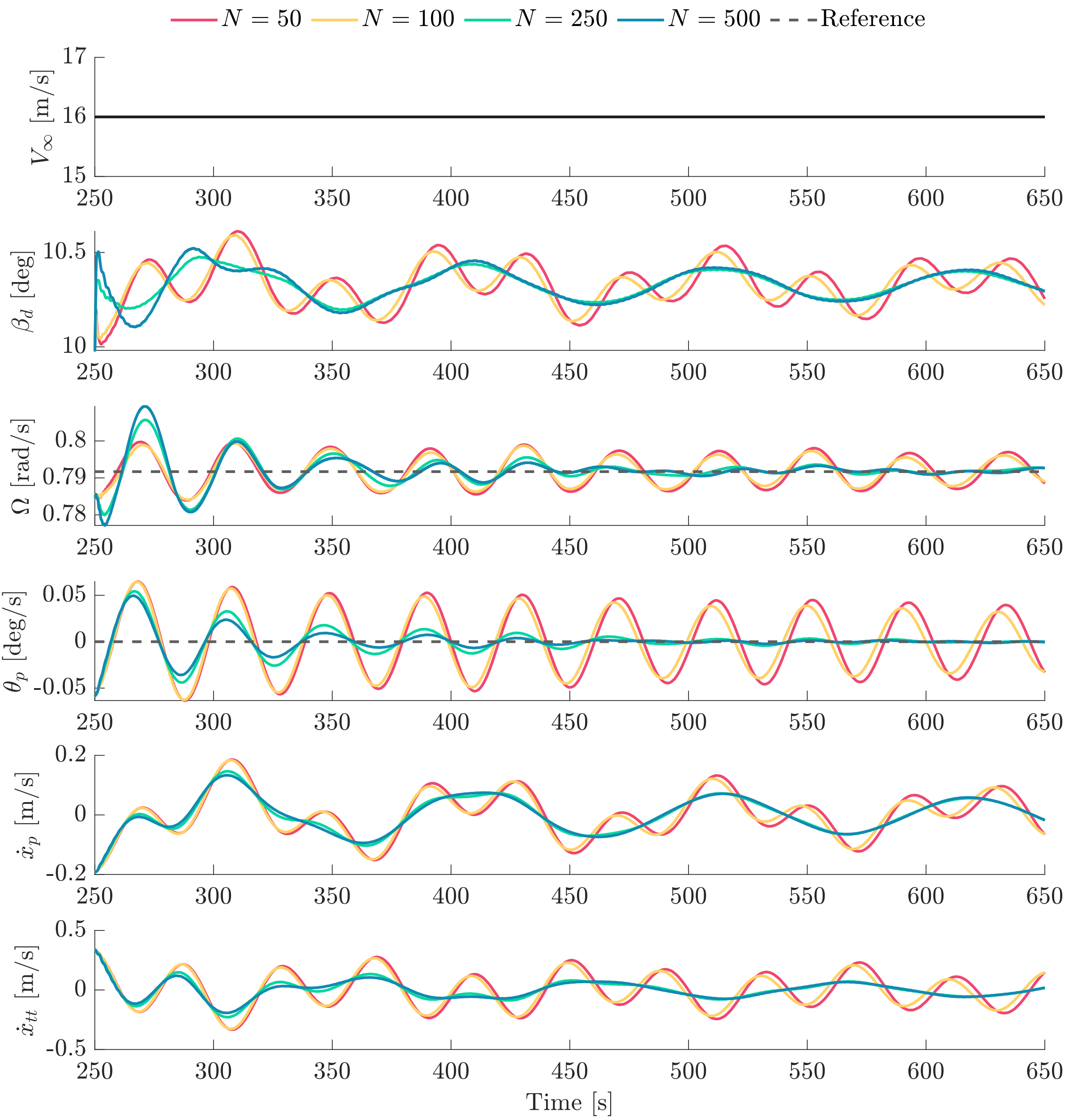

Figure 5.5: Overview of the receding horizon length effect on the demanded blade pitch, the output variables (rotor speed and platform pitch velocity), and platform surge and tower-top velocities. Simulation performed with steady wind at 16 m/s.

transition occurs notably before the wind speed shift, ensuring that the effects primarily arise from this specific change. The initial tuning steps assume perfect knowledge of the state and current disturbances; in other words, the Kalman filter remains inactive, and only the regulatory effects come into play.

The results of adjusting the weights under steady wind conditions for a simple objective function, where the outputs to control are the platform pitch velocity $\dot{\theta}_p$, and the rotor speed Ω, including a penalty to the rate of change of blade pitch Δu, are shown in Figure 5.6. The figure shows clearly that increasing the weight of the platform pitch motion minimisation results in a higher overshoot of the rotor speed during the transition from PI control to MPC since the blade pitch angle is adjusted with the objective of limiting the pitch motion rather than tracking the rated wind speed. The states' displacements and velocities show a similar effect in the frequency of the response to what was seen by adjusting the receding horizon length. Decreasing the weight yields significantly less damping in the platform pitch motion. This effect is also translated to the rotor speed since the platform pitch motion affects the tower-top velocity, which is directly coupled with the rotor speed.

The tuning of the blade pitch rate penalty is shown with a step wind simulation in Figure 5.7. The effect of increasing the penalty to the pitch rate is a reduction in the blade pitch demanded at the step in wind speed, resulting in larger rotor over-speed. Another consequence of modifying the weights is a marginal shift in the frequencies, which may be driven by the ratio between weights and penalties.

Additionally, larger amplitude oscillations and settling time are observed for the platform pitch motion, indicating that reducing or even eliminating the penalty for this case would contribute to better control at the expense of higher pitch activity and, thus, actuator wear. It is, however, noted that, under turbulent wind conditions, a reduced penalty will inherently result in undesired oscillations.

The limitations of fine-tuning the MPC controller's weights via step wind simulations become evident through turbulent simulations, as depicted in Figure 5.8. A Mann turbulent box is employed in this context, characterised by 4% Turbulence Intensity (TI) and three-dimensional turbulent components. To mitigate erratic responses to brief gusts and only act on the platform's low-frequency motions, the wind speed is presumed to be known at hub height and smoothed using a first-order low-pass filter before inputting it into the regulator. A baseline PI controller with parallel compensation (baseline PI - TC) is subjected to the same wind inflow conditions for a meaningful performance comparison.

Substantial penalties are applied to the blade pitch rate to avert unstable controller behaviour. The blade pitch angle closely tracks wind speed trends, as depicted in Figure 5.8a. Additionally, the states, assumed to be perfectly known, introduce considerable noise into the blade pitch signal, thereby diminishing controller performance. While a slight enhancement in platform response is attained by incrementally raising the penalty, thereby constraining blade pitch action, oscillations in rotor speed amplify, leading to a decline in power quality.

To conduct a more comprehensive analysis of the response, a normalised standard deviation metric is introduced, as showcased in Figure 5.8b. In this instance, the standard deviation of the most relevant variables is computed and subsequently normalised with respect to the baseline controller. While this method does indeed result in enhanced platform motion performance, it is important to note that in practical scenarios, the states and wind speed are seldom known directly; they are typically estimated. Therefore, to align with real-world conditions, an augmented Kalman filter is incorporated. This extension aims to yield a more realistic and effective set of weights and penalties for the

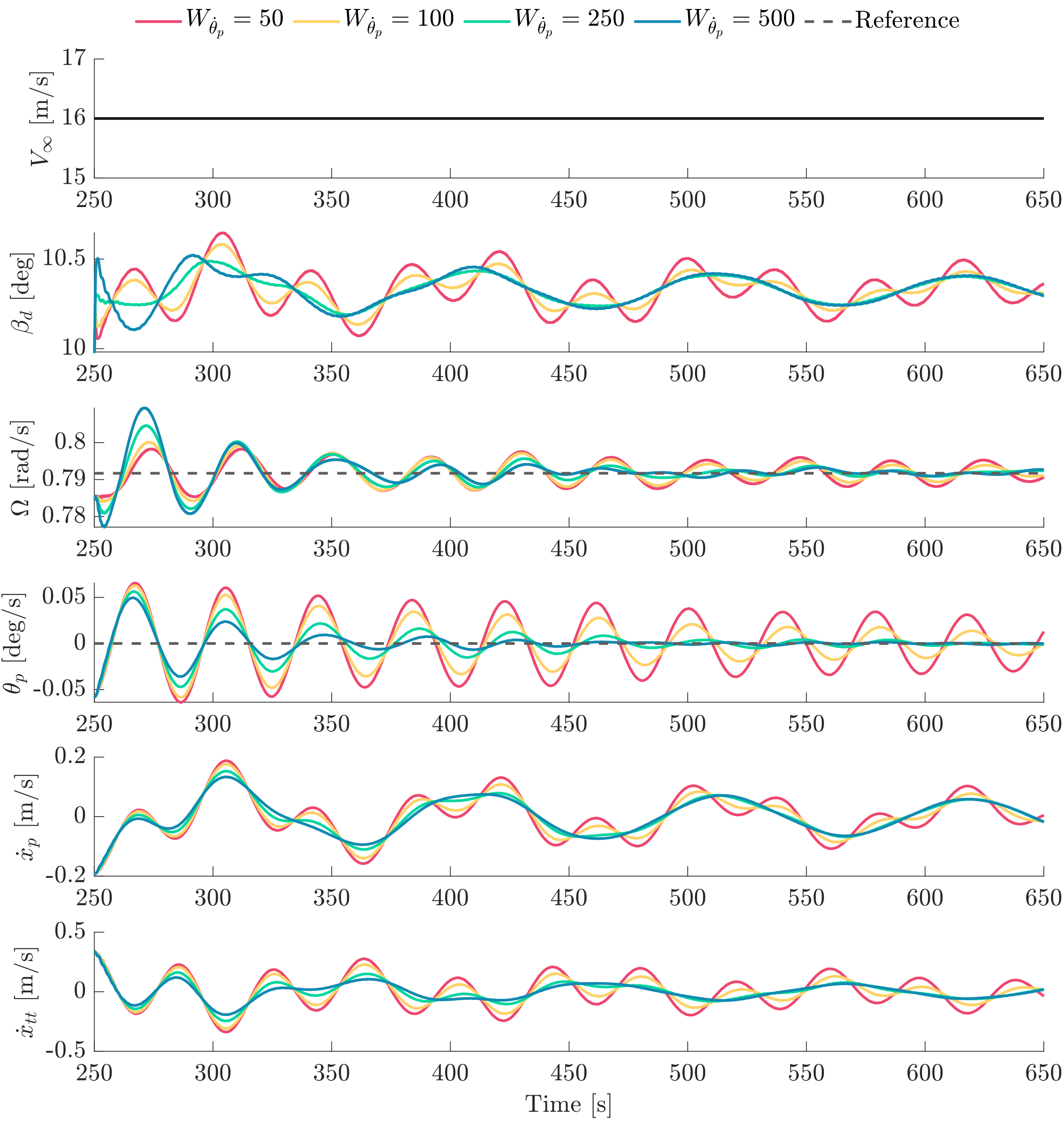

Figure 5.6: Tuning of platform pitch weight $W_{\dot\theta_p}$, under steady wind simulation of 16 m/s. The demanded blade pitch, the output variables (rotor speed and platform pitch velocity), and platform surge and tower-top velocities. The weight for rotor speed tracking is $W_\Omega = 1$, and the pitch rate penalty is $S_{\Delta u} = 1$, for all cases.

MPC controller tuning.

5.3.3 Controller tuning with coupled simulations

The preceding tuning results have shed light on the tuning process and the distinct impacts of controller elements. They've highlighted the substantial influence of the

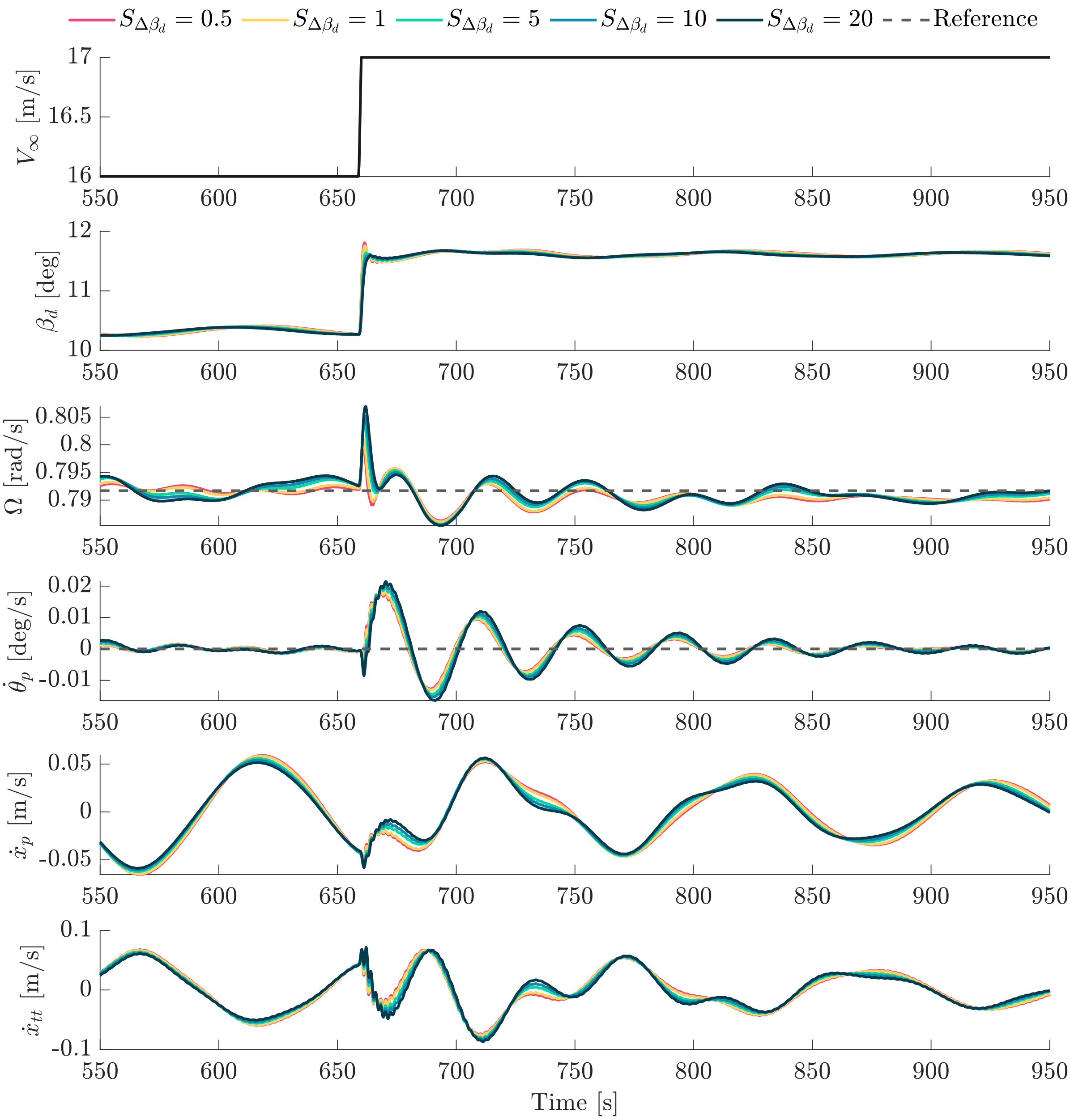

Figure 5.7: Tuning of blade pitch rate penalty $S_{\Delta u}$, under a 1 m/s step in wind, from 16 m/s. The demanded blade pitch, the output variables (rotor speed and platform pitch velocity), and platform surge and tower-top velocities. The weight for platform pitch motion minimisation is $W_{\dot{\theta}_p} = 500$, and for rotor speed tracking is $W_\Omega = 1$, for all cases.

regulated signals and whether they involve state and disturbance estimation or filtered disturbance knowledge. Furthermore, it becomes evident that certain weights may not be appropriately tuned using step-wind simulations. As such, tuning should mirror real-world conditions as closely as possible, encompassing state and disturbance estimation amid turbulent wind inflow. To achieve this, the ADKF is incorporated, as detailed in

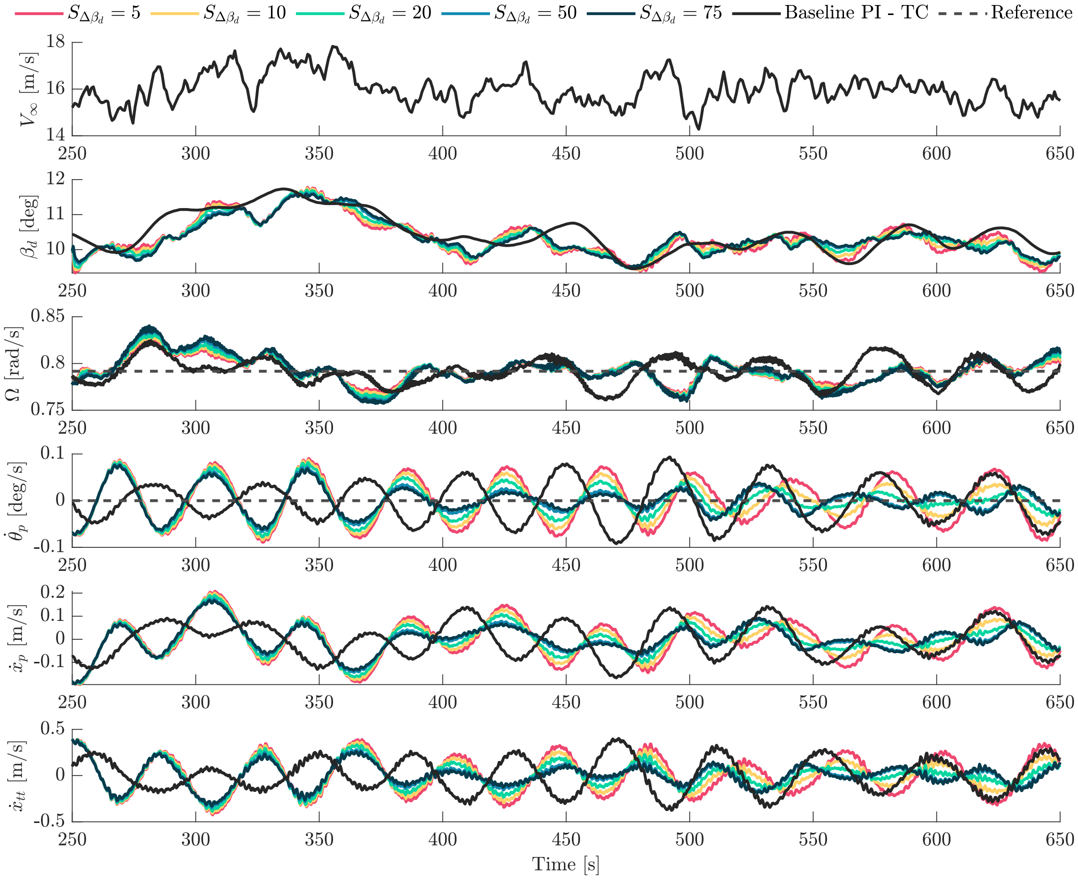

(a) Key indicators

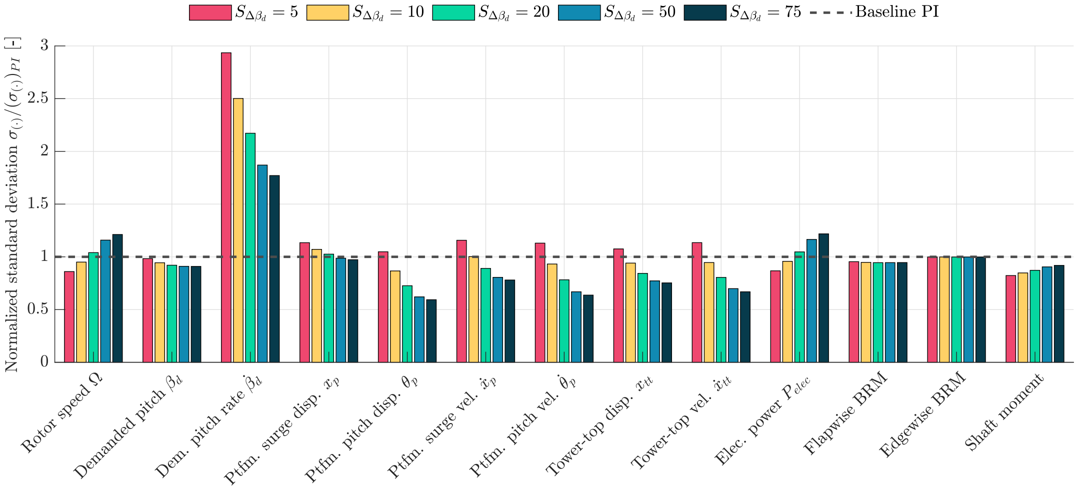

(b) Normalized standard deviation of key signals

Figure 5.8: Tuning of blade pitch rate penalty $S_{\Delta u}$, under turbulent wind simulation, with average wind speed 16 m/s and 4% TI. The weight for platform pitch motion minimisation is $W_{\dot{\theta}_p} = 500$, and for rotor speed tracking is $W_\Omega = 10$, for all cases.

subsection 5.1.1. This step enhances the tuning's realism and effectiveness for the MPC controller.

Three simultaneous cases are considered to tune $W_{\dot{\theta}_p}$ W_{Ω}, and $S_{\Delta u}$. Based on these results, the effect of including the generator torque as controller action is explored.

5.3.3.1 Tuning platform pitch velocity weight $W_{\dot{\theta}_p}$

The weight of rotor speed tracking and blade pitch rate penalty are set to 20 and 1000, respectively, to explore the tuning of the platform pitch velocity weight. Values between 50 and 2000 are used, and the resulting effects on the rotor speed and tower-top velocity oscillations are plotted in Figure 5.9 against the blade pitch rate. The bottom left point represents the largest weight $W_{\dot{\theta}_p} = 2000$, whereas the top-right corresponds to $W_{\dot{\theta}_p} = 50$. It can be extrapolated that the weight could be even further increased for larger marginal gains; however, the controller response is robust to variations in this weight under the given low-turbulence conditions, and no further work is done in this aspect.

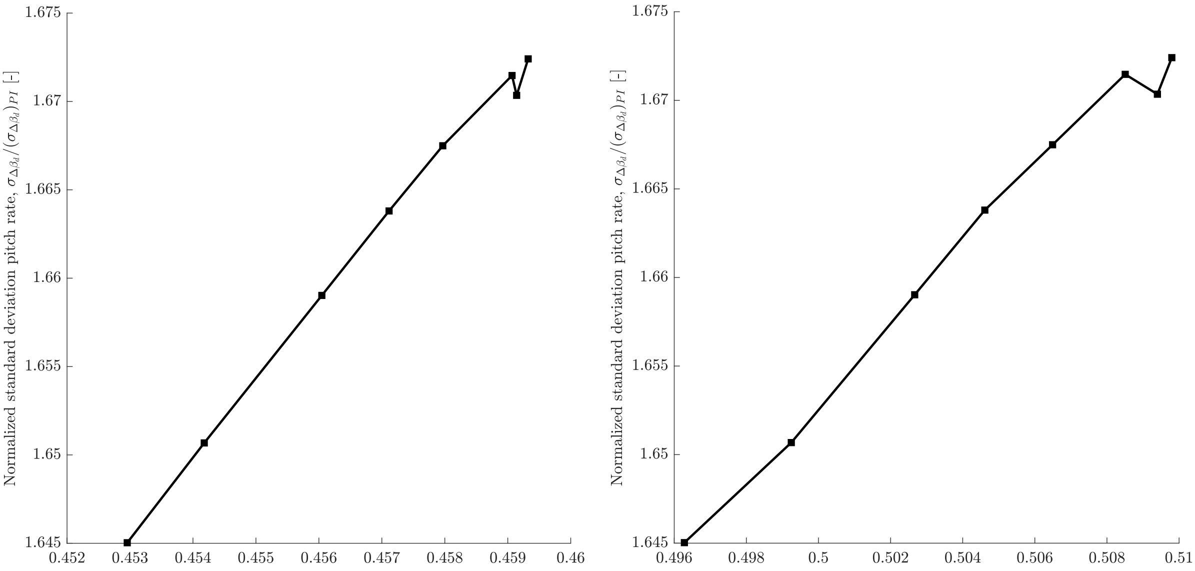

(a) Rotor speed variation against blade pitch rate

(b) Tower-top speed variation against blade pitch rate

Figure 5.9: Pareto front for tuning $W_{\dot{\theta}_p}$ with turbulent simulations at $\bar{V}_{\infty} = 16$ m/s and TI 4%. The normalized standard deviation of rotor speed and tower-top velocity is plotted against the blade pitch rate. The points towards the bottom left represent higher values of $W_{\dot{\theta}_p}$. The simulations correspond to $W_{\Omega} = 20$ and $S_{\Delta\beta_d} = 1000$.

5.3.3.2 Tuning rotor speed tracking weight W_{Ω}

The effect of changing the rotor speed weight W_{Ω} on the rotor speed, tower-top velocity and demanded pitch rate can be seen in Figure 5.10. The rotor speed variations

(Figure 5.10a) are increasingly minimised for values from $W_\Omega = 1$ to $W_\Omega = 20$, at the expense of higher blade pitch activity. The simulated values $W_\Omega = 10$ and $W_\Omega = 20$ result in the lowest rotor speed deviations, with minor differences in motions and loads. Higher values lead to a rapid decrease in performance.

Further analysis has been conducted in relation to other KPIs, as depicted in Figure 5.11. When increasing the values of W_Ω to 30, a notable rise in the flapwise BRM is observed, accompanied by a minor increase in the standard deviation of the shaft moment. In contrast, the motions at the platform and tower-top either remain relatively unaffected or even experience reductions in their amplitude.

For $W_\Omega = 40$, there is a significant escalation in the rotor speed standard deviation. However, this increase does not surpass that observed at $W_\Omega = 2$. This situation raises a plausible explanation for the amplified load – the substantial rise in the blade pitch rate velocity. This heightened velocity directly influences the unsteady aerodynamic load, a phenomenon simulated in HAWC2 through dynamic inflow and dynamic stall engineering models. Notably, the HAWC2 simulations employ the MHH Dynamic Stall model as outlined in [82] and linearized in [83]. This engineering model evaluates aerodynamic loads not solely based on the instantaneous angle of attack but also takes into account its rate of change. This rate of change is profoundly impacted by the penalty within the controller.

Comparing the results obtained with the lightest and heaviest weights, although rotor speed deviations are diminished for W_Ω equal to 40 (which directly influences the angle of attack), the rate of change of the blade pitch becomes three times higher. This circumstance elucidates the upsurge in flapwise BRM standard deviation, consequently augmenting the potential for greater fatigue loads.

In essence, this analysis underscores the potential efficacy of manipulating variables that govern unsteady aerodynamic loading, both in achieving performance enhancements and, at the very least, in averting deterioration.

5.3.3.3 Tuning blade pitch rate penalty $S_{\Delta u}$

Several values for the blade pitch rate penalty are tested, and the results shown in Figure 5.12 and Figure 5.13. Lower values of $S_{\Delta\beta_d}$ can yield unstable behaviour and enhanced motions. The Pareto fronts show however the important trade-off between rotor speed tracking and platform motion minimisation. Whereas decreasing the penalty yields limited motions at the tower-top, the rotor speed oscillations increase quickly from $S_{\Delta\beta_d} = 1000$ to 500, highlighting the sensitivity in that case. The penalty weight $S_{\Delta\beta_d} = 1500$ seems to provide the best trade-off between rotor speed tracking and tower-top motion.

Increasing the penalty quickly causes the blade pitch rate to decrease, and a marginal improvement in the flapwise BRM is observed, possibly caused by the reduction of unsteady aerodynamic loads linked to smaller changes in blade pitch rate, as explored for the rotor speed weight tuning in the previous section.

To perform a more comprehensive analysis of the substantial impact caused by $S_{\Delta\beta_d} = 500$ on the system's response, the time series of both rotor speed and demanded

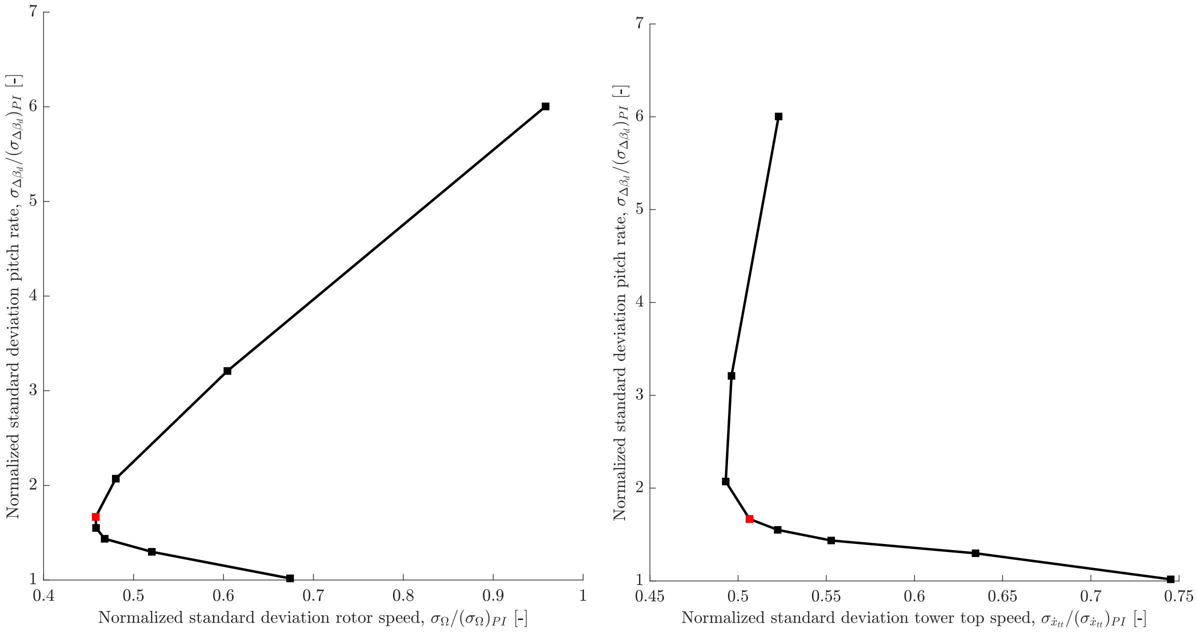

(a) Rotor speed variation against blade pitch rate

(b) Tower-top speed variation against blade pitch rate

Figure 5.10: Pareto front for tuning W_Ω with turbulent simulations at $\bar{V}_\infty = 16$ m/s and TI 4%. The normalised standard deviation of rotor speed and tower-top velocity is plotted against the blade pitch rate. The red square corresponds to $W_\Omega = 20$, the point at the top right to $W_\Omega = 50$, whereas the lowest point to $W_\Omega = 1$. The simulations are done with $W_{\dot{\theta}_p} = 500$ and $S_{\Delta\beta_d} = 1000$.

blade pitch are presented in Figure 5.14. Within the context of this particular penalty setting, an intriguing trend emerges after $t = 450$ s, marked by a heightened pitch actuation and the emergence of oscillations with considerable amplitude in the rotor speed signal. This phenomenon could potentially be attributed to the sudden wind speed drop occurring just before this time point, compounded by a notable reduction in the blade pitch angle, which could be triggering the platform pitch instability. It is worth noting that for wind speed $V_\infty = 14$ m/s the pole-zero map showed RHPZ (see Figure 3.7), that is, stability issues become more evident near rated wind speeds.

A similar effect is also noticeable in the baseline controller; however, in this instance, the pitch actuation lags behind the stable configurations established by the MPC. Consequently, a significant reduction in rotor speed is succeeded by substantial oscillations. To examine the frequency response of the *unstable* MPC setup, the Power Spectral Density (PSD) of the signals is explored, as depicted in Figure 5.15 for rotor speed and Figure 5.16 for flapwise BRM.

The analysis reveals that the dominant frequency aligns with approximately ~ 0.08 Hz, a value significantly distant from the symmetric natural frequencies of the platform as well as the $1P$ frequency. In the flapwise BRM response, a minor peak is evident for all other penalty settings, hinting at the possibility of the controller introducing this

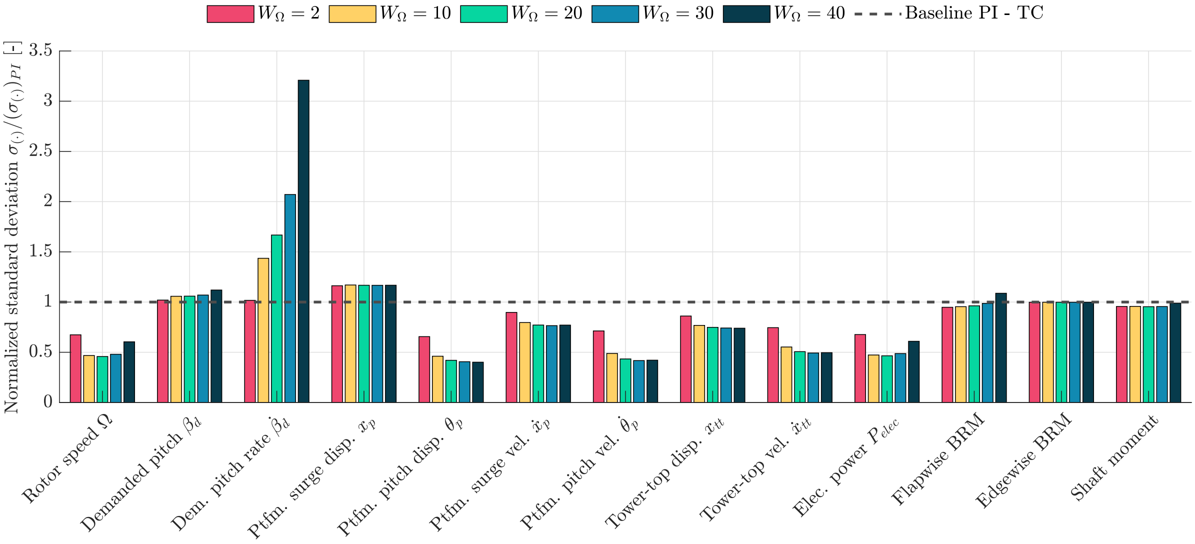

Figure 5.11: Tuning of rotor speed tracking W_Ω, under turbulent wind simulation, with average wind speed 16 m/s and 4% TI. The normalised standard deviation of relevant signals is shown for several weighting values. The weight for platform pitch motion minimisation is $W_{\dot{\theta}_p} = 500$, and the penalty to blade pitch rate is $S_{\Delta\beta_d} = 1000$, for all cases.

frequency. However, due to its relatively small magnitude, a conclusive determination is challenging. This frequency peak is absent in the platform response. Nevertheless, it becomes prominent for both the flapwise BRM and rotor speed responses at $S_{\Delta\beta_d} = 500$, only to nearly vanish at $S_{\Delta\beta_d} = 1000$. This observation suggests that, for $\bar{V}_\infty = 16$ m/s, a stable controller can only be achieved with $S_{\Delta\beta_d} > 500$. It is worth noting that a future exploration could involve determining the minimum allowable penalty that guarantees a stable controller. However, as previously noted, the most favourable trade-offs conveniently avoid such stability limitations, making this analysis unnecessary.

The blade pitch rate standard deviation is consistently higher than the baseline, even for the larger cases; however, it decreases significantly between $S_{\Delta\beta_d} = 500$ and 1000. The PSD shown in Figure 5.17 shows the comparison between the four MPC tuning cases and the baseline for a large frequency range, comprising the natural frequencies of the platform and 1P. The baseline controller reacts only to frequencies below 0.05 Hz, as the bandwidth has been reduced to avoid instability issues. On the other hand, the greedier MPC strongly reacts at a frequency of approximately 0.08 Hz, which is most likely the frequency introduced by the controller feedback loop. The increasing penalty damps out such frequency and shifts it towards lower frequencies. However, the power contained in the demanded pitch reaction is clearly larger for any MPC tuning than for the baseline case, especially around the pitch frequency. Further increasing the penalty beyond the optimum point, roughly found at $S_{\Delta\beta_d} = 1500$, leads to worsening power quality and platform motions since the controller is not able to react fast enough to the changing disturbances.

It is clear that low penalties can have a major negative impact in some channels

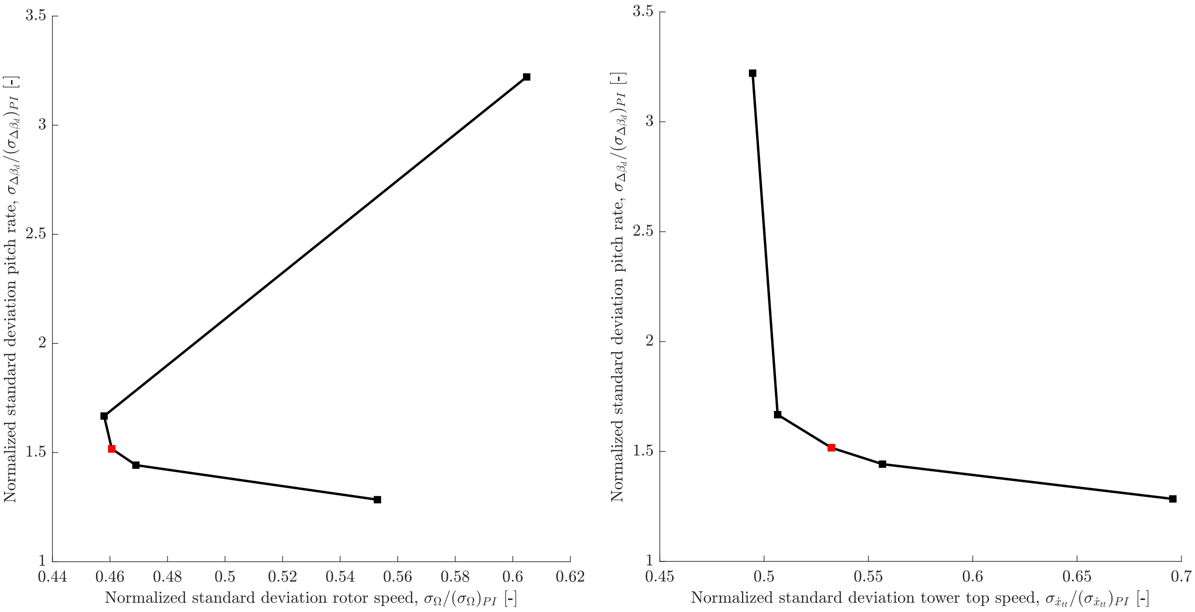

(a) Rotor speed variation against blade pitch rate

(b) Tower-top speed variation against blade pitch rate

Figure 5.12: Pareto front for tuning $S_{\Delta\beta_d}$ with turbulent simulations at $\bar{V}_\infty = 16$ m/s and TI 4%. The normalised standard deviation of rotor speed and tower-top velocity is plotted against the blade pitch rate. The red square corresponds to $S_{\Delta\beta_d} = 1500$, the point at the top right to $S_{\Delta\beta_d} = 500$, whereas the lowest point to $S_{\Delta\beta_d} = 5000$. The simulations are done with $W_{\dot{\theta}_p} = 500$ and $W_\Omega = 20$.

despite improving the response of, for instance, the platform motions. This result clearly contradicts the resulting tuning showed in Figure 5.7, for a step-wind simulation with perfect state and disturbance knowledge, where values of the penalty as low as 0.5 provided a stable response. It can be understood that the tuning procedure should be performed using turbulent simulations and considering the impact on the full dynamics of the system.

5.3.3.4 Tuning generator torque rate penalty $S_{\Delta Q_g}$

The addition of generator torque to the controlled variables has the potential to improve the response. It does, however add an additional tuning parameter, the penalty $S_{\Delta Q_g}$. To test the effects of this penalty on the rotor speed tracking and the platform pitch motions, a set of controller gains based on the previous analysis is selected, as shown in Table 5.1. Figure 5.18 shows the main simulation results for several $S_{\Delta Q_g}$ penalties. As could be expected, decreasing the penalty increases the generator torque activity, which clearly follows the same trend as the blade pitch. This is due to having as objectives the minimisation of rotor speed deviation from rated value and platform pitch velocity. Both generator torque and blade pitch have the same effect; if the generator torque magnitude increases, the rotor will decelerate, analogously to an increase in blade pitch. However,

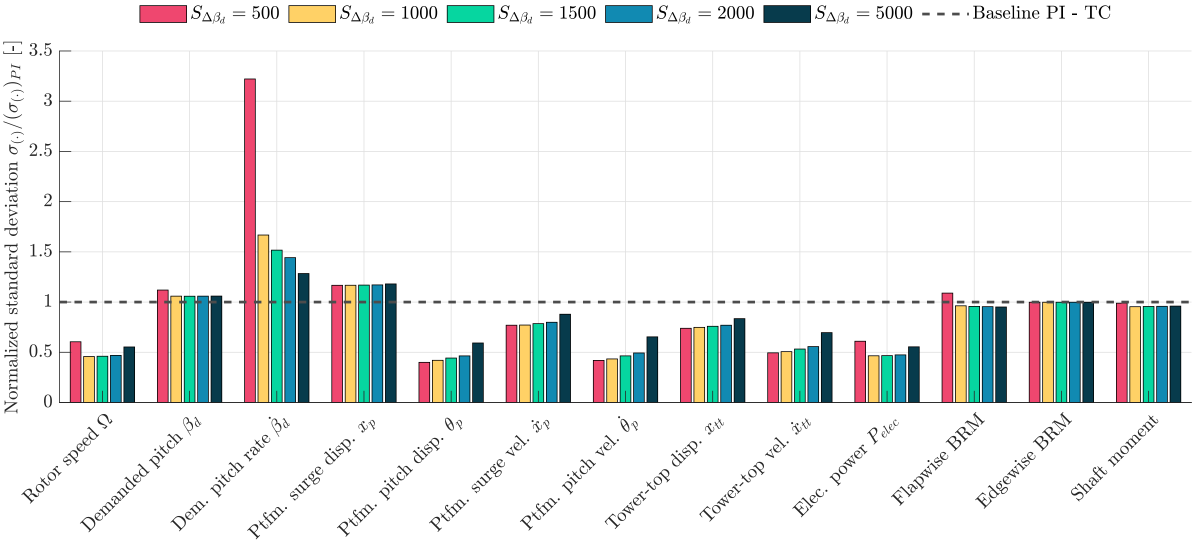

Figure 5.13: Tuning of blade pitch rate penalty $S_{\Delta\beta_d}$, under turbulent wind simulation, with average wind speed 16 m/s and 4% TI. The normalised standard deviation of relevant signals is shown for several weighting values. The weight for platform pitch motion minimisation is $W_{\dot{\theta}_p} = 500$, and the weight for rotor speed tracking is $W_\Omega = 20$, for all cases.

since there is not dynamic inflow effect included in the reduced order model, nor actuator delays, the controller is not able to capture the time-lag/delay of these actions.

Table 5.1: Set of UMPC controller parameters to test the effect of generator torque rate penalty

Receding horizon N	Ptfm. pitch vel. $W_{\dot{\theta}_p}$	Rotor speed W_Ω	Blade pitch rate $S_{\Delta\beta_d}$
500	500	20	2000

The main impact of adding the generator torque is an increase in the shaft standard deviation, which can be seen in Figure 5.19, whereas marginal gains are obtained in the other signals, indicating that torque control without constant power objective has limited achievements as compared to pitch control. To showcase that, a sensitivity to the blade pitch rate penalty is shown in Figure 5.20, with a constant value of generator torque rate penalty of $S_{\Delta Q_g} = 1e - 08$. It is clear that increasing the penalty to pitch actuation leads to higher torque actuation and, thus, larger shaft moment oscillations and standard deviation. It is also apparent that controlling the motions through larger generator torque rates is less effective since the platform pitch oscillations and rotor speed deviation increase. On the other hand, the flapwise BRM loads slightly decrease with lower blade pitch actuation.

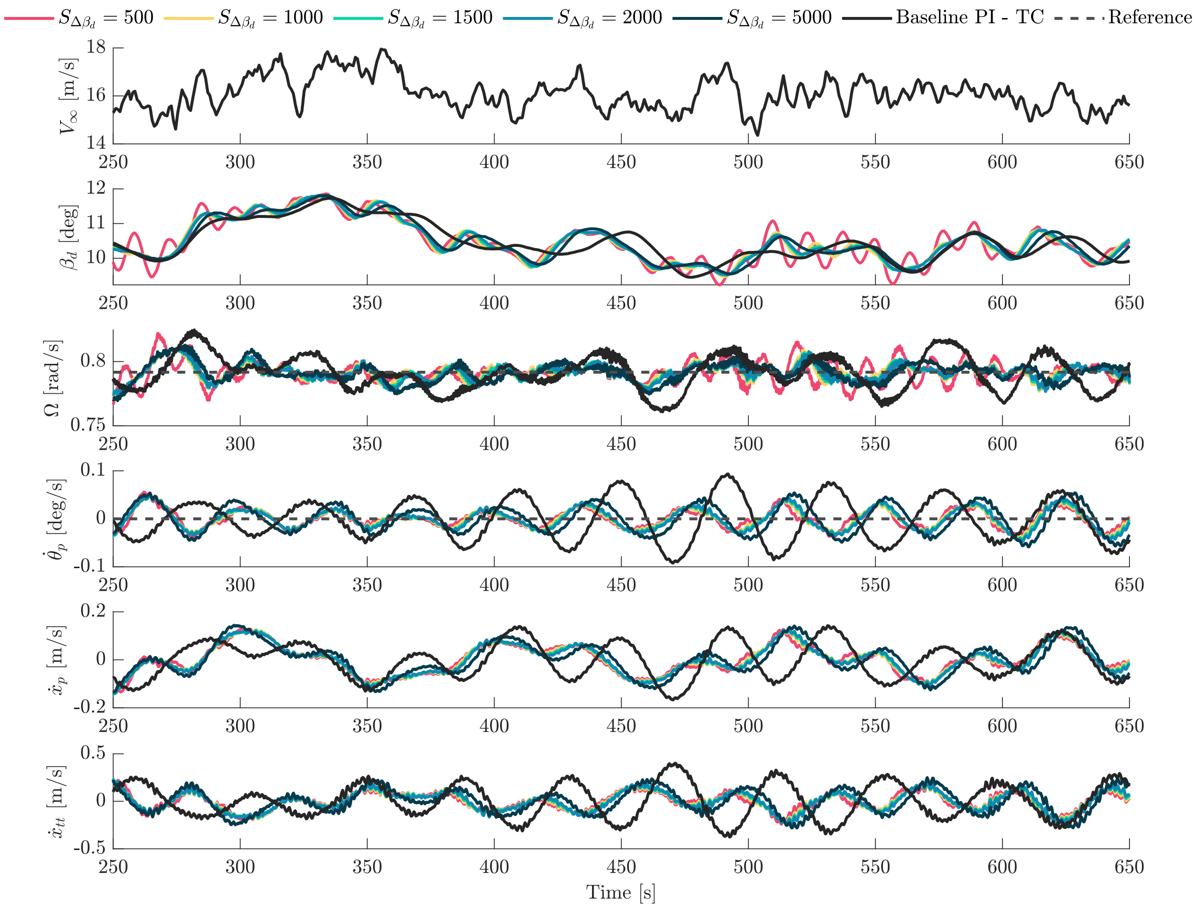

Figure 5.14: Tuning of blade pitch rate penalty $S_{\Delta\beta_d}$, under turbulent wind simulation, with average wind speed 16 m/s and 4% TI. The wind speed, rotor speed and demanded blade pitch are shown for several weighting values. The weight for platform pitch motion minimisation is $W_{\dot{\theta}_p} = 500$, and the weight for rotor speed tracking is $W_\Omega = 20$. The red dashed line represents the rated rotor speed value.

5.4 Tuning at higher TI and 14 m/s

During the load analysis displayed in section 6.2, the tuning was found to be unstable at $\bar{V}_\infty = 14$ m/s with $TI = 10\%$. For that reason, a set of simulations with different penalties is launched to understand whether better tuning is able to achieve better performance or whether model limitations explain the poorer results at that wind speed.

A simultaneous swept over blade pitch rate penalties and platform pitch weight motion is considered first. The fine-tuning of the blade pitch rate penalty is depicted in Figure 5.21. The optimal penalty range lies within 2000 and 3000, with the former leading to slightly higher pitch actuation but reduced tower top motions and rotor speed fluctuations, combined with improved power quality, but a marginal worsening of flapwise BRM, as shown in Figure 5.22. For the next fine-tuning steps $S_{\Delta\beta_d} = 2000$ is considered.

Figure 5.23 illustrates how a lower penalty choice, such as 1500, leads to enhanced

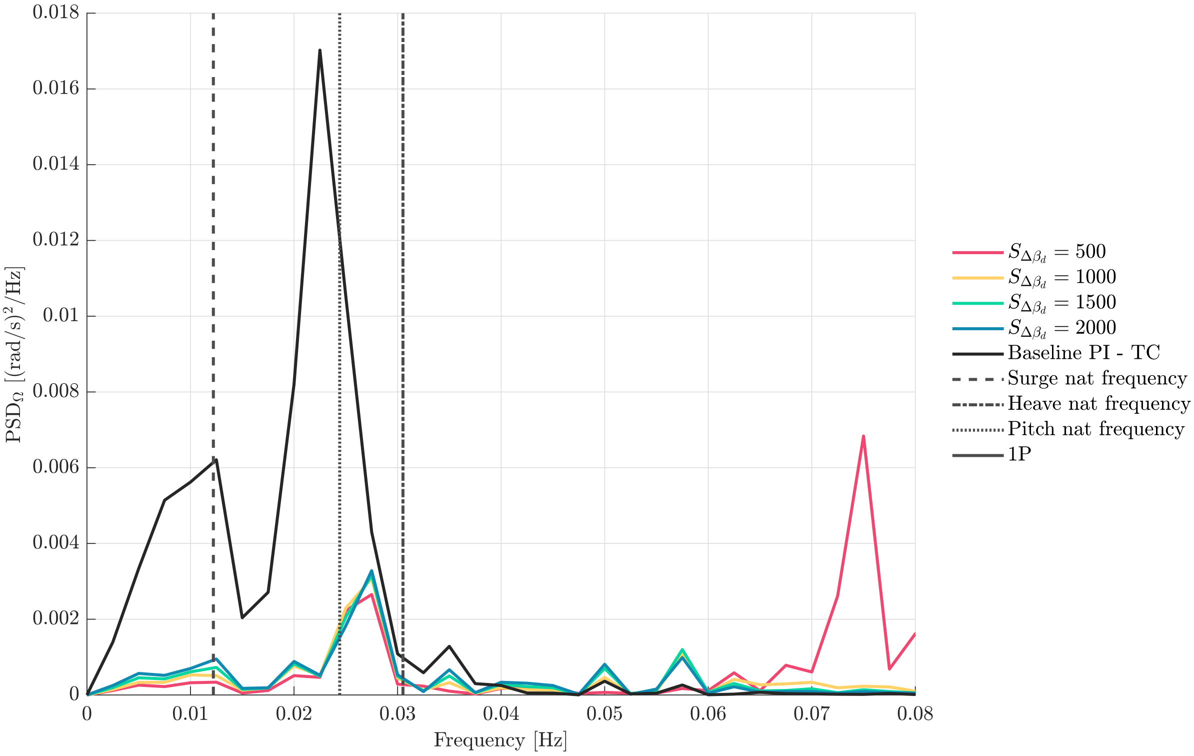

Figure 5.15: Power Spectral Density (PSD) of rotor speed signal for several values of $S_{\Delta\beta_d}$, under turbulent wind simulation, with average wind speed 16 m/s and 4% TI. The weight for platform pitch motion minimisation is $W_{\dot{\theta}_p} = 500$, and the weight for rotor speed tracking is $W_\Omega = 20$.

rotor speed fluctuations. Inspecting the time series qualitatively it is seen that the high frequency oscillations in rotor speed are translated to the platform motions and the demanded blade pitch angle.

The platform pitch weight fine-tuning is shown in Figure 5.24. Analogously to Figure 5.9, further increasing the weight (for the range explored) yields performance improvements in terms of both platform motions, rotor speed fluctuations and electrical power output. The maximum value $W_{\dot{\theta}_p} = 10000$ is taken to explore the rotor speed weight fine-tuning.

The same procedure is followed to obtain the Pareto fronts in Figure 5.25 for several rotor speed weights. The values are compared with Figure 5.10, enabling a comparison of the tuning procedure for different wind conditions. It is clear that the trade-off is significantly more limited for the higher turbulence intensity case, where a small offset in the weight with respect to the optimal value can notably worsen the performance. Consequently, the optimal weight selection seems to be intrinsically linked to the wind atmospheric conditions. Furthermore, the stability of the FOWT is harder to achieve near rated wind speeds, which was expected from the classic PI control approach.

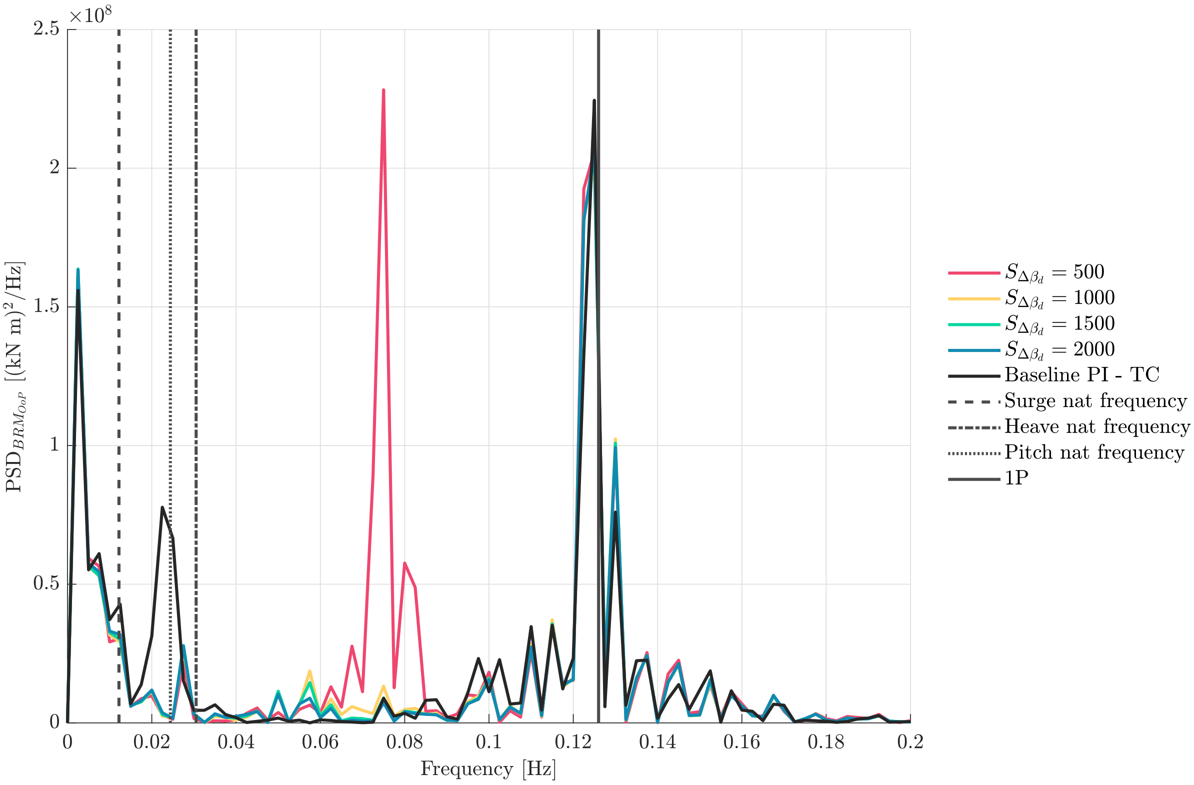

Figure 5.16: Power Spectral Density (PSD) of flapwise BRM signal for several values of $S_{\Delta\beta_d}$, under turbulent wind simulation, with average wind speed 16 m/s and 4% TI. The weight for platform pitch motion minimisation is $W_{\dot{\theta}_p} = 500$, and the weight for rotor speed tracking is $W_\Omega = 20$.

5.5 Final remarks

This chapter explored the derivation and implementation of the fully coupled MPC. The stationary Kalman filter was discarded due to the non-existence of a stabilising solution to the DARE. Instead, the DKF is used to overcome such limitations. It is proven that an augmented Kalman filter provides not only adequate estimation of the wind disturbance but also improvements in the prediction of measurable and unmeasurable states. Then, the derivation of an unconstrained MPC is shown, with emphasis on the tuning procedure. It is evident that using steady or step-wind simulations does not provide effective weights and penalties and can potentially induce undesired oscillations, especially in the rotor speed. Furthermore, the observer needs to be used during the tuning procedure to fine-tune the controller weights. The platform pitch velocity weight $W_{\dot{\theta}_p}$, plays a less relevant role, whereas the fine-tuning of the rotor speed weight and the blade pitch rate penalty can be used to significantly improve the response when using turbulent wind simulations in the tuning procedure.

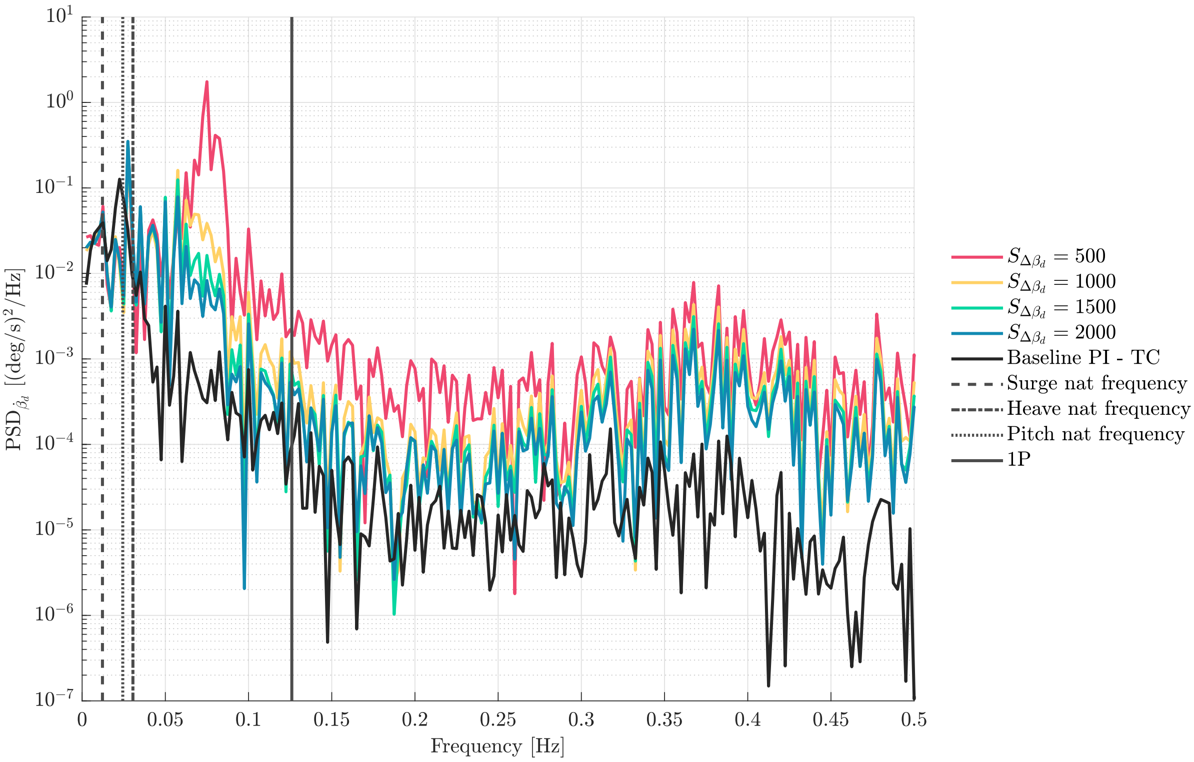

Figure 5.17: Power Spectral Density (PSD) of demanded blade pitch rate signal for several values of $S_{\Delta\beta_d}$, under turbulent wind simulation, with average wind speed 16 m/s and 4% TI. The weight for platform pitch motion minimisation is $W_{\dot{\theta}_p} = 500$, and the weight for rotor speed tracking is $W_{\Omega} = 20$.

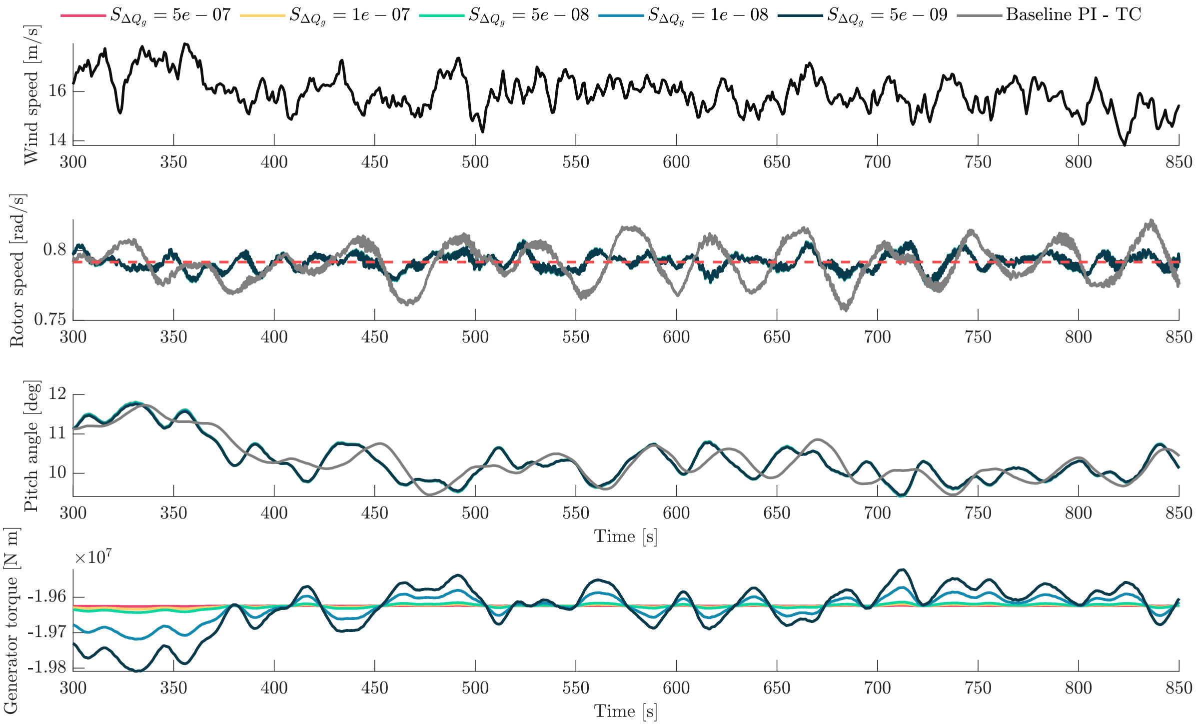

Figure 5.18: Tuning of generator torque rate penalty $S_{\Delta Q_g}$, under turbulent wind simulation, with average wind speed 16 m/s and 4% TI. The rotor speed, demanded blade pitch and generator torque are shown for several weighting values. The weight for platform pitch motion minimisation is $W_{\dot{\theta}_p} = 500$, for rotor speed tracking is $W_{\Omega} = 20$, and the blade pitch rate penalty is $S_{\Delta \beta_d} = 2000$, for all cases. The red dashed line represents the rated rotor speed value.

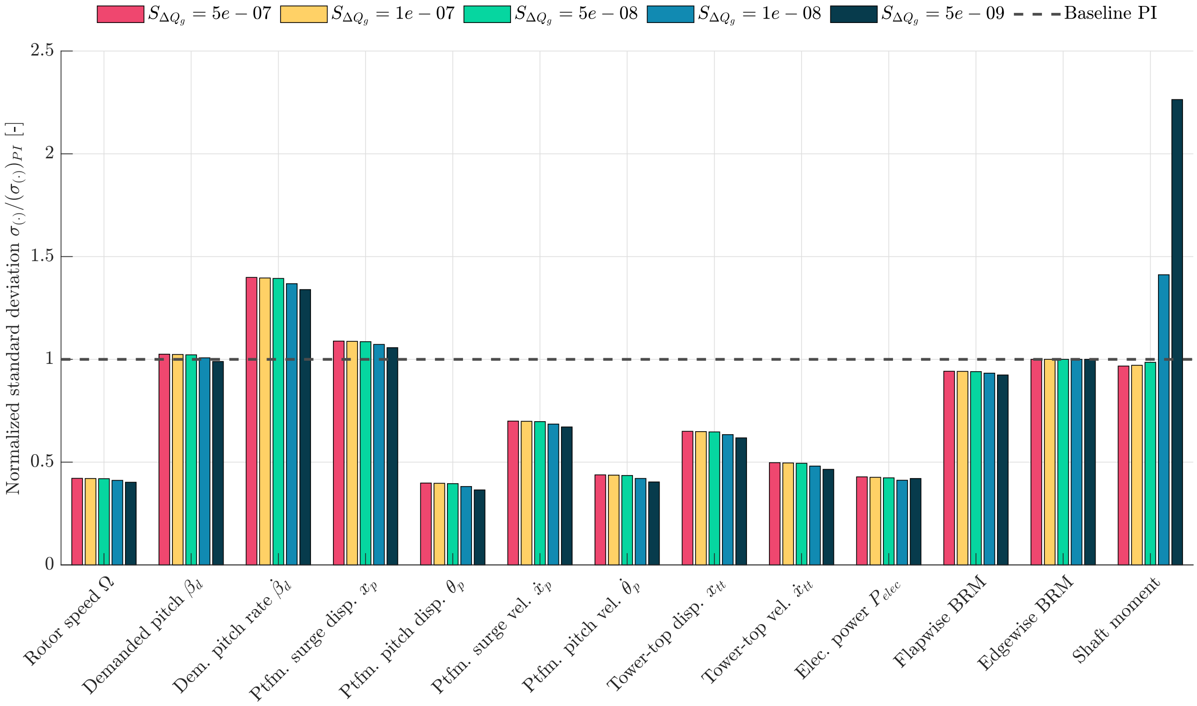

Figure 5.19: Tuning of generator torque rate penalty $S_{\Delta Q_g}$, under turbulent wind simulation, with average wind speed 16 m/s and 4% TI. The standard deviation of the most relevant signals is normalised with the baseline PI controller with torque compensation. The weight for platform pitch motion minimisation is $W_{\dot{\theta}_p} = 500$, for rotor speed tracking is $W_\Omega = 20$, and the blade pitch rate penalty is $S_{\Delta \beta_d} = 2000$, for all cases.

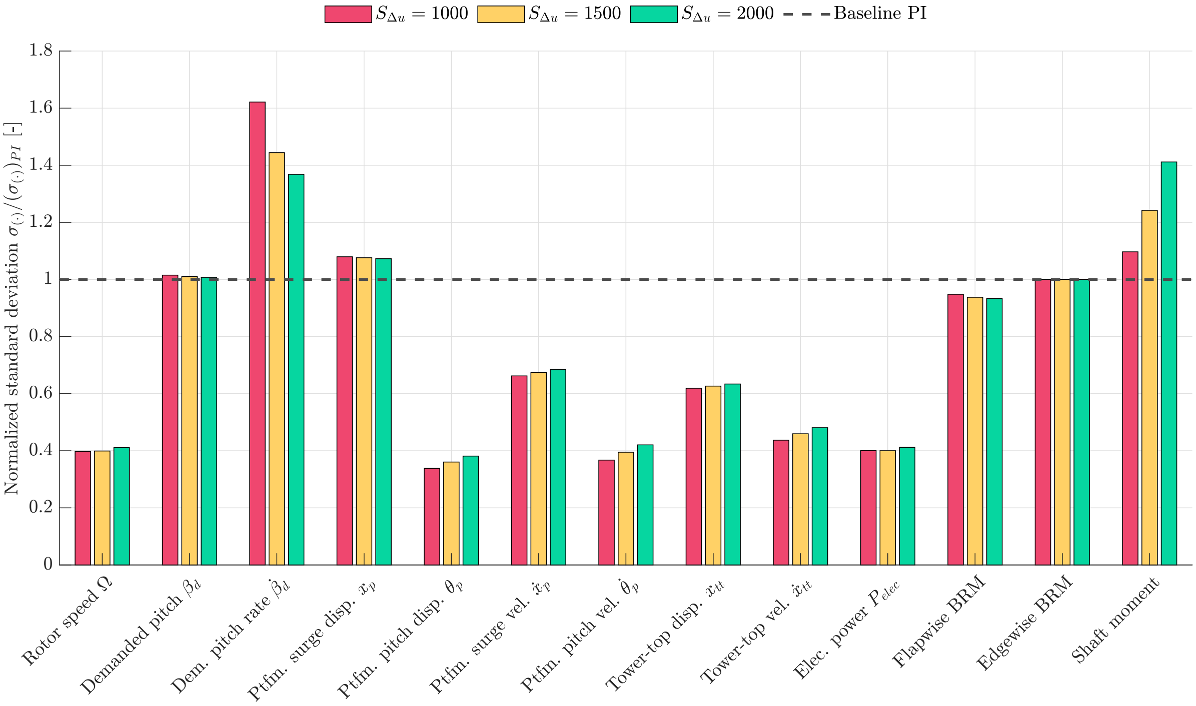

Figure 5.20: Tuning of blade pitch rate penalty $S_{\Delta\beta_d}$, under turbulent wind simulation, with average wind speed 16 m/s and 4% TI. The standard deviation of the most relevant signals is normalised with the baseline PI controller with torque compensation. The weight for platform pitch motion minimisation is $W_{\dot{\theta}_p} = 500$, for rotor speed tracking is $W_\Omega = 20$, and the generator torque rate penalty is $S_{\Delta Q_g} = 1e-8$, for all cases.

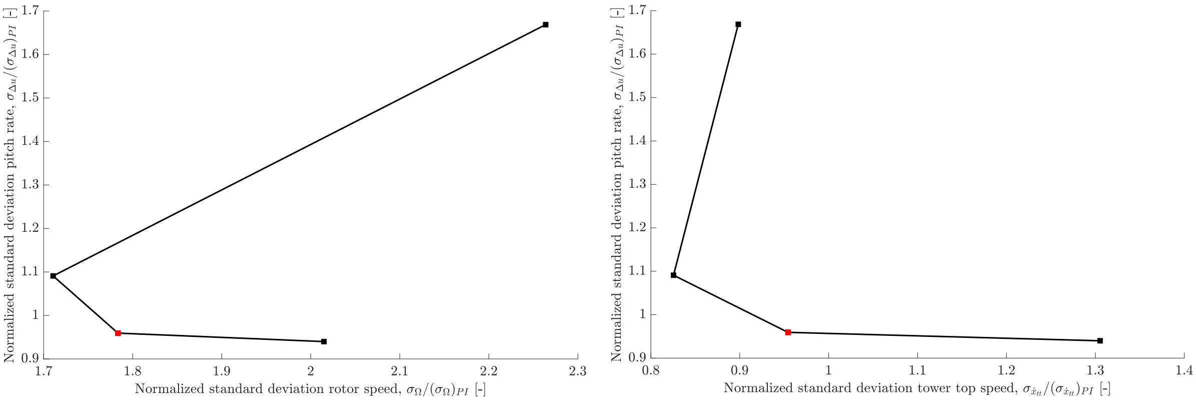

(a) Rotor speed variation against blade pitch rate

(b) Tower-top speed variation against blade pitch rate

Figure 5.21: Pareto front for tuning $S_{\Delta\beta_d}$ with turbulent simulations at $\bar{V}_\infty = 14$ m/s and TI 10%. The normalised standard deviation of rotor speed and tower-top velocity is plotted against the blade pitch rate. The red square corresponds to $S_{\Delta\beta_d} = 3000$, the point at the top right to $S_{\Delta\beta_d} = 500$, whereas the lowest point to $S_{\Delta\beta_d} = 5000$. The simulations are done with $W_{\dot{\theta}_p} = 500$ and $W_\Omega = 20$.

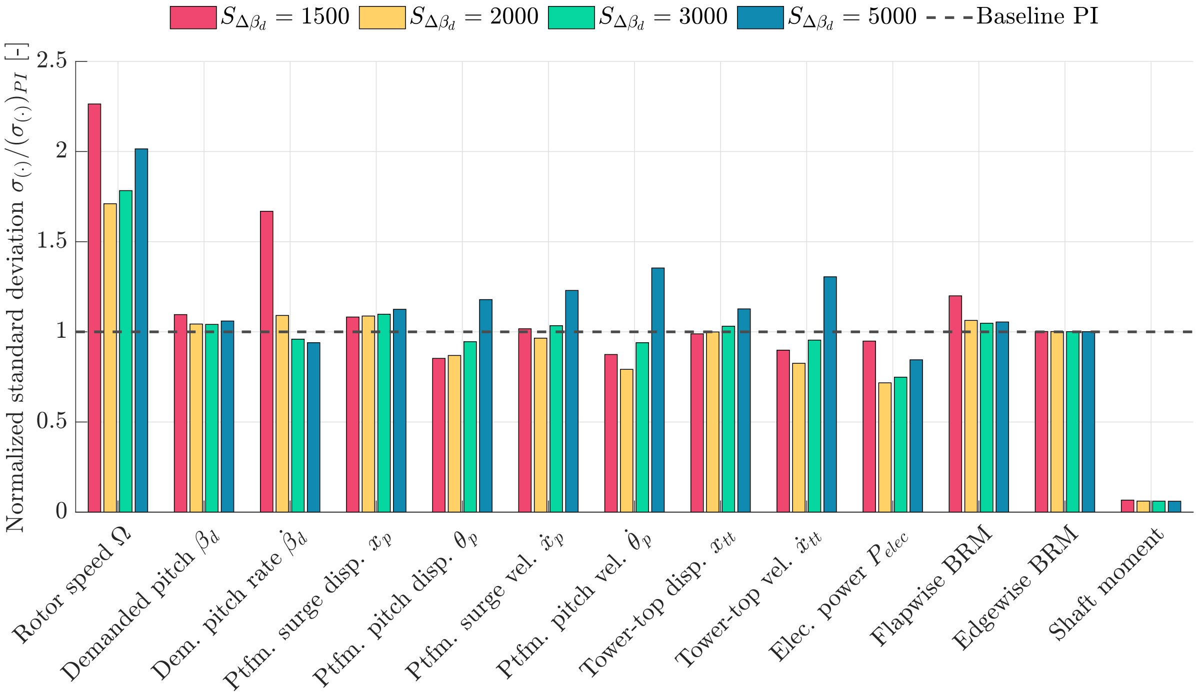

Figure 5.22: Tuning of blade pitch rate penalty $S_{\Delta\beta_d}$, under turbulent wind simulation, with average wind speed 14 m/s and 10% TI. The normalised standard deviation of relevant signals are shown for several weighting values. The weight for platform pitch motion minimisation is $W_{\dot{\theta}_p} = 500$, and the weight for rotor speed tracking is $W_{\Omega} = 20$, for all cases.

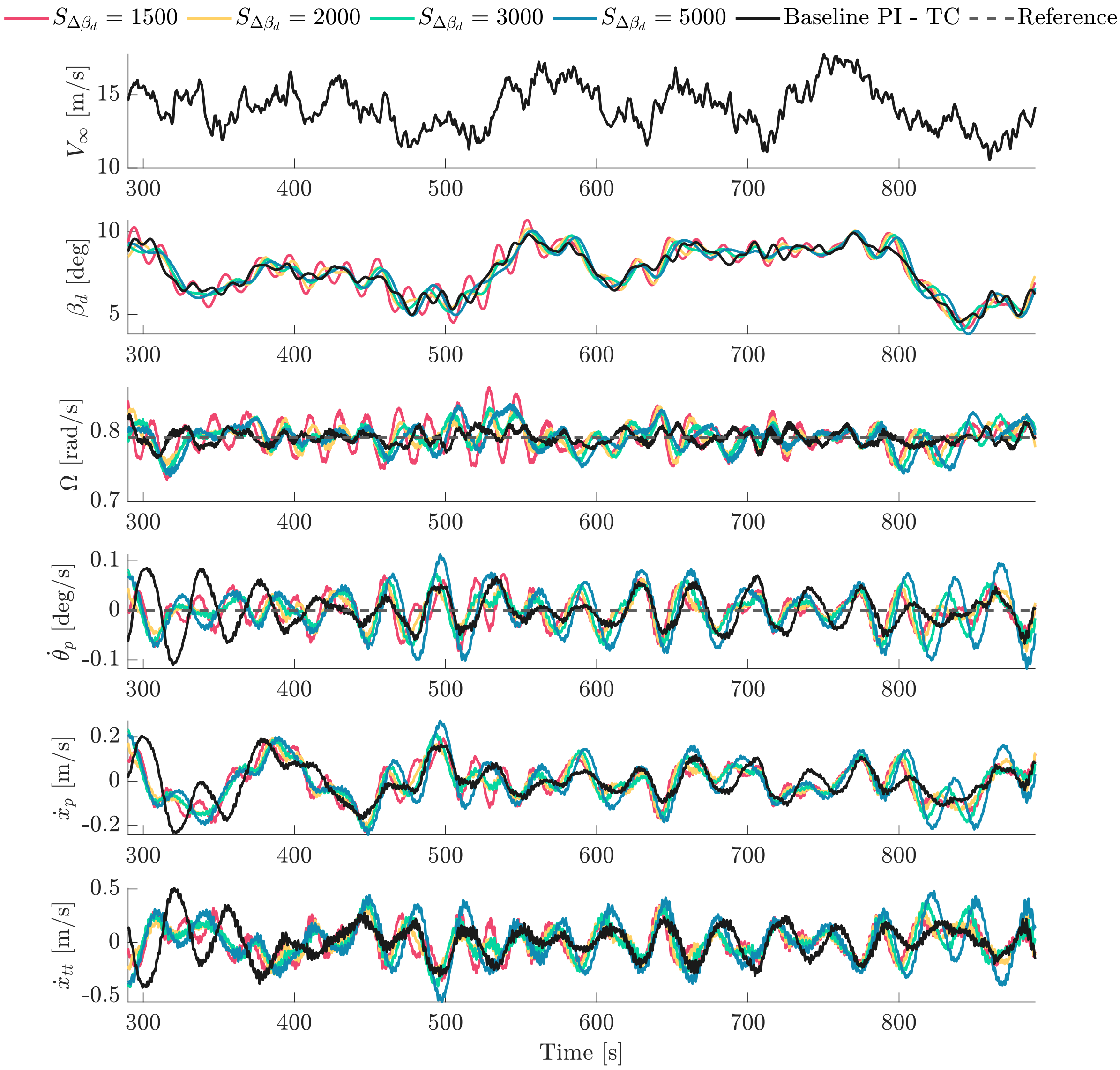

Figure 5.23: Tuning of blade pitch rate penalty $S_{\Delta\beta_d}$, under turbulent wind simulation, with average wind speed 14 m/s and 10% TI. The wind speed, rotor speed and demanded blade pitch are shown for several weighting values. The weight for platform pitch motion minimisation is $W_{\dot{\theta}_p} = 500$, and the weight for rotor speed tracking is $W_\Omega = 20$. The red dashed line represents the rated rotor speed value.

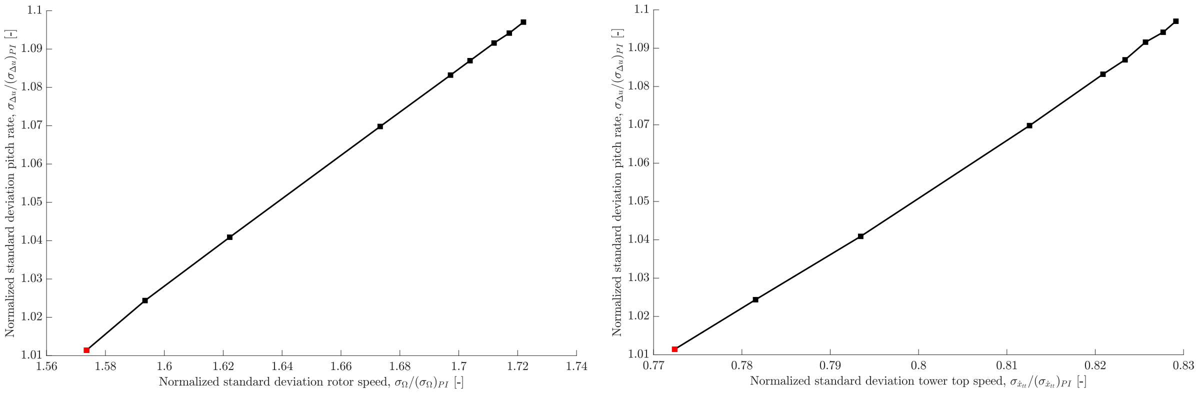

(a) Rotor speed variation against blade pitch rate

(b) Tower-top speed variation against blade pitch rate

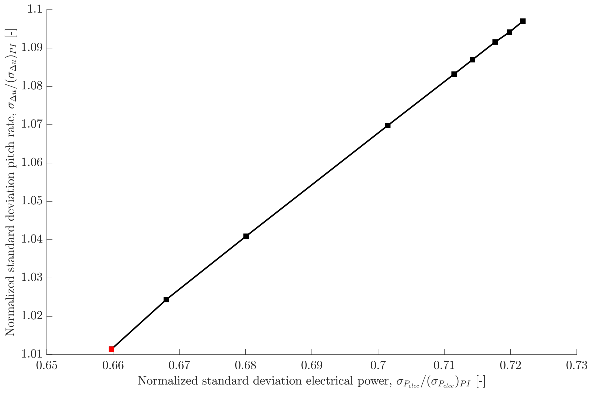

(c) Electrical power output variation against blade pitch rate

Figure 5.24: Pareto front for tuning $W_{\dot{\theta}_p}$ with turbulent simulations at $\bar{V}_{\infty} = 14$ m/s and TI 10%. The normalised standard deviation of rotor speed, tower-top velocity and electrical power output is plotted against the blade pitch rate. The red square corresponds to $W_{\dot{\theta}_p} = 10000$, the point at the top right to $W_{\dot{\theta}_p} = 100$. The simulations are done with $W_{\Omega} = 20$ and $S_{\Delta\beta_d} = 2000$.

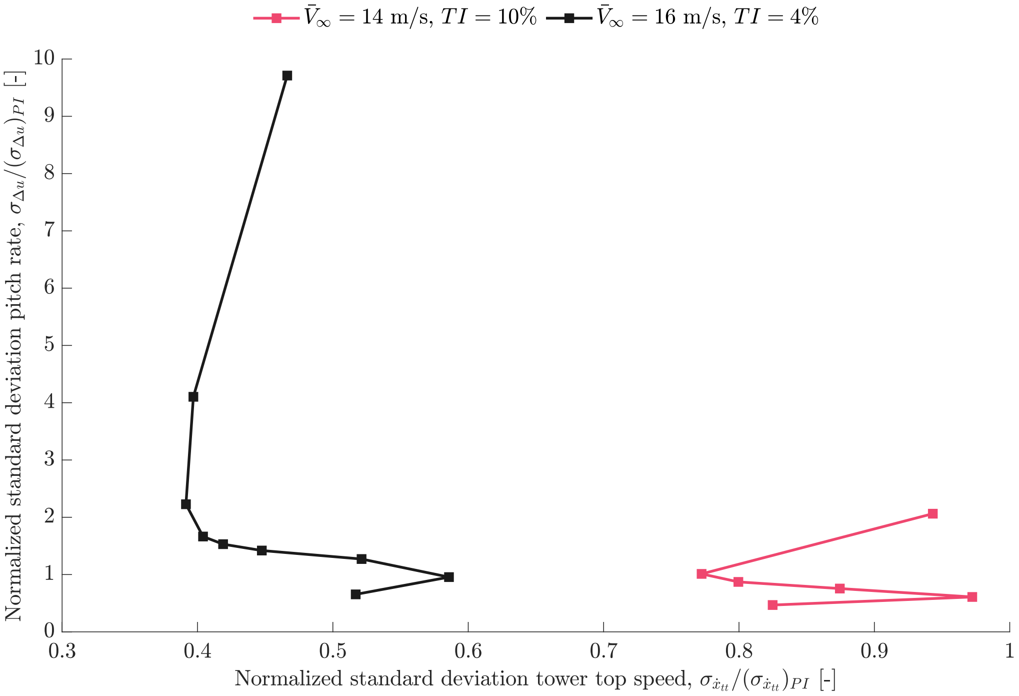

(a) Tower-top speed variation against blade pitch rate

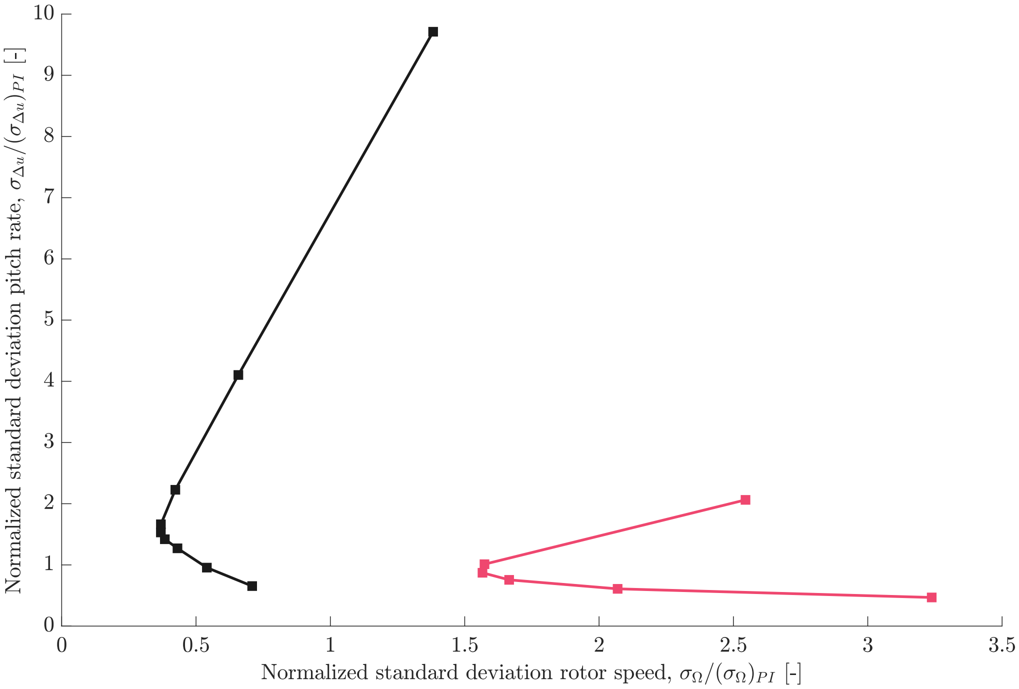

(b) Rotor speed variation against blade pitch rate

Figure 5.25: Pareto front for tuning W_Ω with turbulent simulations at $\bar{V}_\infty = 14$ m/s and TI 10%, compared with $\bar{V}_\infty = 16$ m/s and TI 4%. Normalised standard deviation of rotor speed and tower-top velocity is plotted against the blade pitch rate.

CHAPTER 6

Results

6.1 Simulation set-up

For the implementation of the controller logic, MATLAB is employed due to its versatility and smooth compatibility with HAWC2. The linear MPC is developed from scratch in MATLAB, bypassing the utilisation of pre-existing toolboxes. This methodology enables the refinement of algorithms and a more profound understanding of the underlying concepts.

Considering the dynamics of the HAWC2 simulation, an initial ramp-up phase is introduced to mitigate initial irregularities. As the linear MPC relies on a linearised model that holds within a specific operational range, the simulations commence with the conventional DTUWEC controller to ensure stability. Subsequently, the wind speed is gradually adjusted over a period of 200 seconds. Following this, a 15-second interval is allocated for the fundamental PI controller before transitioning to the linear MPC.

To derive meaningful insights, a focused time frame of 600 seconds is selected, commencing at 290 seconds and extending to 890 seconds. This interval effectively avoids any impact stemming from the initial ramp-up and the controller switch, ensuring a robust data analysis.

6.1.1 Tuning parameters

The UMPC is tuned based on the procedure outlined in section 5.3. Based on the results obtained, the tuning in Table 6.1 is proposed to be used in the load analysis. Since the first iteration of turbulent simulations showed an instability issue at $\bar{V}_\infty = 14$ m/s, the blade pitch rate penalty is increased to $S_{\Delta\beta_d} = 3000$ based on the tuning procedure outlined in section 5.3, although it was later found to not be the most optimal tuning, as shown in section 5.4.

Table 6.1: Tuning parameters for Unconstrained MPC, used for load analysis.

Receding horizon, N	Ptfm. pitch vel. $W_{\dot{\theta}_p}$	Rotor speed W_Ω	Blade pitch rate $S_{\Delta\beta_d}$
500	500	20	1500

The baseline PI controller with torque compensation is tuned according to [66]. A summary of the key controller parameters is provided in Table 6.2. It is important to bear in mind that the comparison of certain KPIs will not be evident. The generator torque is kept constant in the linear MPC, whereas the baseline uses the generator torque to address the tower-top velocity, thus leading to rather large variations in parameters such as the electric power output or the shaft torsion moment.

On the other hand, the torque compensation controller proved capable of minimising platform motions and improving rotor speed tracking, thus it is used such that the new controller is benchmark against a controller with better performance in platform motion minimisation.

Table 6.2: Baseline controller tuning parameters, based on [66].

Blade pitch controller	
Pole placement frequency	0.05 Hz
Pole placement damping	0.7
k_P at 0 degrees	0.9188 rad/(rad/s)
k_I at 0 degrees	0.2683 rad/rad
Linear gain scheduling gain	11.611 deg
Quadratic gain scheduling gain	709.685 deg^2
Torque compensation feedback loop	
k_{Px}, compensation gain	$-4.508 \cdot 10^6$ N · m/(m/s)
Linear gain scheduling gain	0.020 1/deg
Quadratic gain scheduling gain	0.001 1/deg^2

6.2 Load analysis with TI 10%

The Design Load Cases (DLC) 1.1 and 1.2 from IEC 61400-1 are employed to compare the performance of the UMPC. However, the TI is set at 10%, below the standard-defined 14% for class B (see Table 3.2). There are two main reasons behind this choice,

- the model predictive controller is not scheduled; therefore, the results for higher TI will be biased by the use of a model suited for a narrow range of wind speeds,
- the baseline controller response tends to result in extreme overshoot, particularly noticeable in the power output.

Hence, it is believed that a more reliable comparison can be obtained at $TI = 10\%$. Additionally, TI in offshore locations usually proves lower than at onshore sites [84, 85], and typically TI inversely correlates with the average wind speed magnitude. However, this does not hold at very high wind speeds in offshore sites, since the wind-induced waves increase the *terrain roughness*, leading to higher turbulence. It is therefore clear that further assessment at higher TI levels will be needed.

The effects of wind shear and tower shadow are not accounted for in the simulations, similarly to [45], in order to simplify the analysis. Furthermore, no waves are considered, as the estimator was not validated beforehand for wave estimation, and the computational effort associated with the extended, lengthy simulations (45-minute simulations defined in IEC 61400-3 standard for offshore wind turbines) needed for meaningful statistics was not justified. This approach was also adopted in [34]. A sensitivity study on the impact of the aforementioned assumptions is provided in section 6.3.

The most pertinent KPIs are utilised to compare the UMPC with the baseline controller featuring torque compensation. The same turbulent wind fields are applied in both cases to facilitate a representative comparison unaffected by the limited number of seeds. The primary statistical parameters are calculated for each simulation seed, including mean, maximum, and minimum values, along with the standard deviation. Fatigue loads are determined using short-term Damage Equivalent Loads (DELs) through rainflow counting, applying the S-N curve with suitable Wöhler exponents, i.e. $m = 4$ for steel (shaft and tower) and $m = 10$ for composite materials (blades). Finally, extreme values and loads are computed based on the mean value of the absolute maximum for each channel. To accommodate the use of the mean in the extreme loads, a safety factor of 1.35 is incorporated into the resultant extreme load, followed by the IEC 61400-1 DLC 1.1 safety factor of 1.25.

6.2.1 Operation in turbulence

The rotor speed, blade pitch and blade pitch rate are shown in Figure 6.1. The performance is significantly better in terms of rotor speed tracking for all wind speeds, except at $\bar{V}_\infty = 14$ m/s, where large overshoots and oscillations are observed. The main cause might be the used of a model linearized at a single wind speed, which is not able to match accurately the aerodynamic loading under gusts due to the large changes in torque and thrust derivatives, as shown in Figure 3.4 and Figure 3.5, respectively. Additionally, the thrust curve peaks at the rated wind speed, $V_{rated} = 10.59$ m/s, leading to larger platform motions for mean wind speeds close to the rated value.

The effect of rotor speed variations can be directly seen in the electrical power output of the UMPC-case, whereas the resulting power is less evident for the torque compensation controller, since the generator torque is used to affect the platform dynamics. From the comparison in Figure 6.2 it is clear that the power quality is greatly improved by using MPC as compared to the baseline. The mean value of UMPC follows perfectly the rated power, as expected for full-load operation, but that is not the case for the baseline controller, where its mean value is lower consistently for all wind speeds considered, therefore an improved AEP is expected by using MPC. Additionally, it over and undershoots for all wind-speeds, reaching up to 18 MW at $\bar{V}_\infty = 24$ m/s. The worst performance of the UMPC regarding this KPI is attained at $\bar{V}_\infty = 14$ m/s, as expected from the rotor speed analysis. The standard deviation is however significantly lower than for the baseline, thus much better power quality is obtained.

One of the main objectives of the controller is to limit the platform motions, especially the pitch motion that is responsible for instability issues. In Figure 6.3, the velocities (left) and displacements (right) of symmetric motions are displayed. All motions are reduced by the model-predictive controller. The performance improvement is especially noticeable in the tower-top velocity, which peaks at about $\bar{V}_\infty = 22$ m/s. For the MPC case, the lowest maximum values and standard deviation occur at $\bar{V}_\infty = 16$ m/s, the wind speed for which the controller has been tuned. This may indicate that further improvements can be achieved for other wind speeds if the weights are tuned for those cases.

The use of constant generator torque should evidently lead to reduced motions in the non-symmetric motions, namely sway, roll, and yaw. The sway is negligible under the

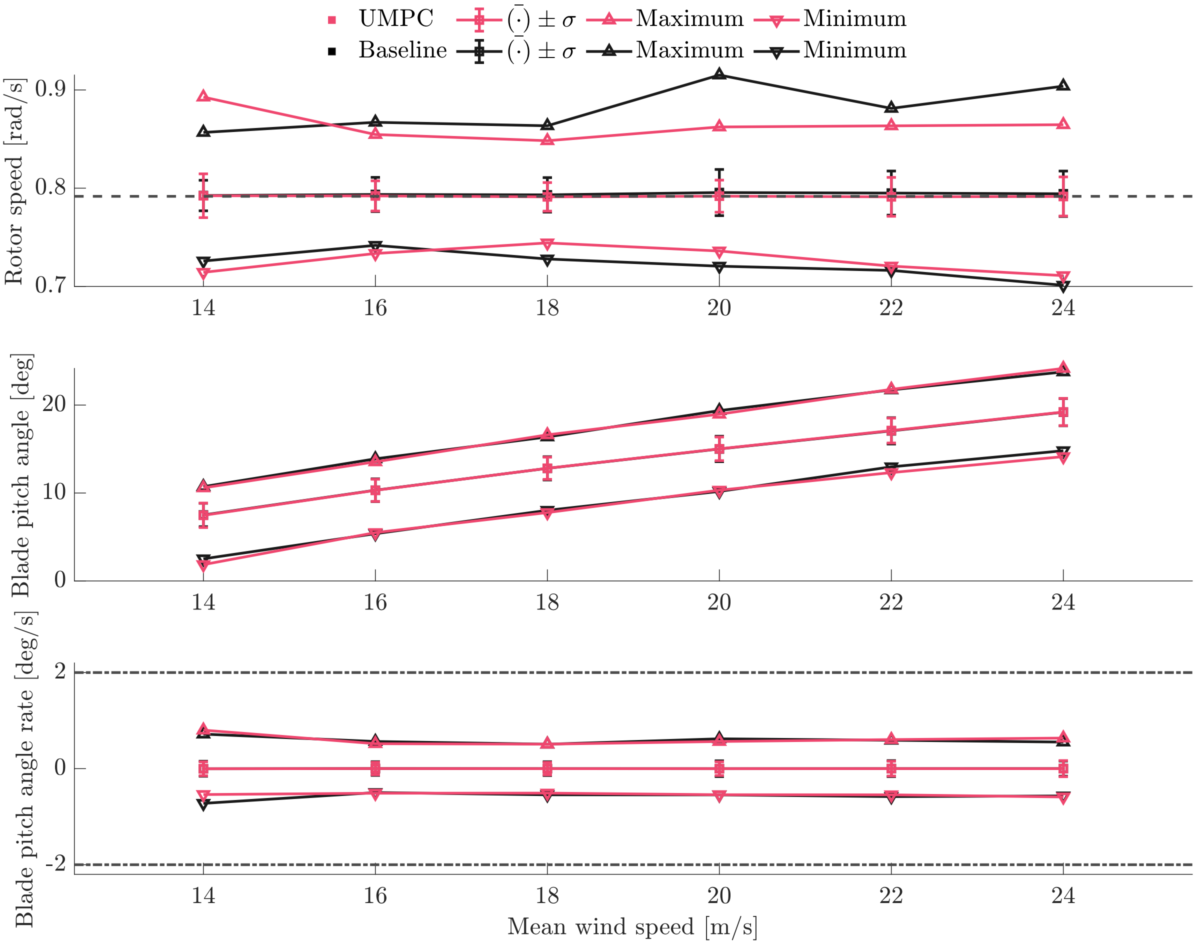

Figure 6.1: Statistical analysis of rotor speed, demanded blade pitch and demanded blade pitch rate for above rated wind speeds, under turbulent wind simulations $TI = 10\%$. The dashed line corresponds to the rated rotor speed, and the dot-dashed line to the actuator limits.

simulation conditions, whereas roll and yaw velocities and displacements are shown in Figure 6.4. The roll velocity and displacement are much lower using MPC than using the baseline controller, since the generator torque does not dynamically excite such motions. On the other hand, under unidirectional wind without waves, the yaw motion is only excited by the v' and w' turbulent components of the wind-field, as well as the heave-roll-yaw hydrodynamic coupling. In the current work, the yaw motion has not change with respect to the baseline controller, Probably a weak hydrodynamic coupling and a high yaw stiffness, which leads to a higher natural frequency (0.092Hz [70]) explain these results.

It can be expected that either the controller developments considering the generator torque actuation, or wind-wave misalignment would lead to enhanced non-symmetric motions, and therefore it is important to consider their extent, and potentially tackling them through their inclusion in the model and the objective function, however, this

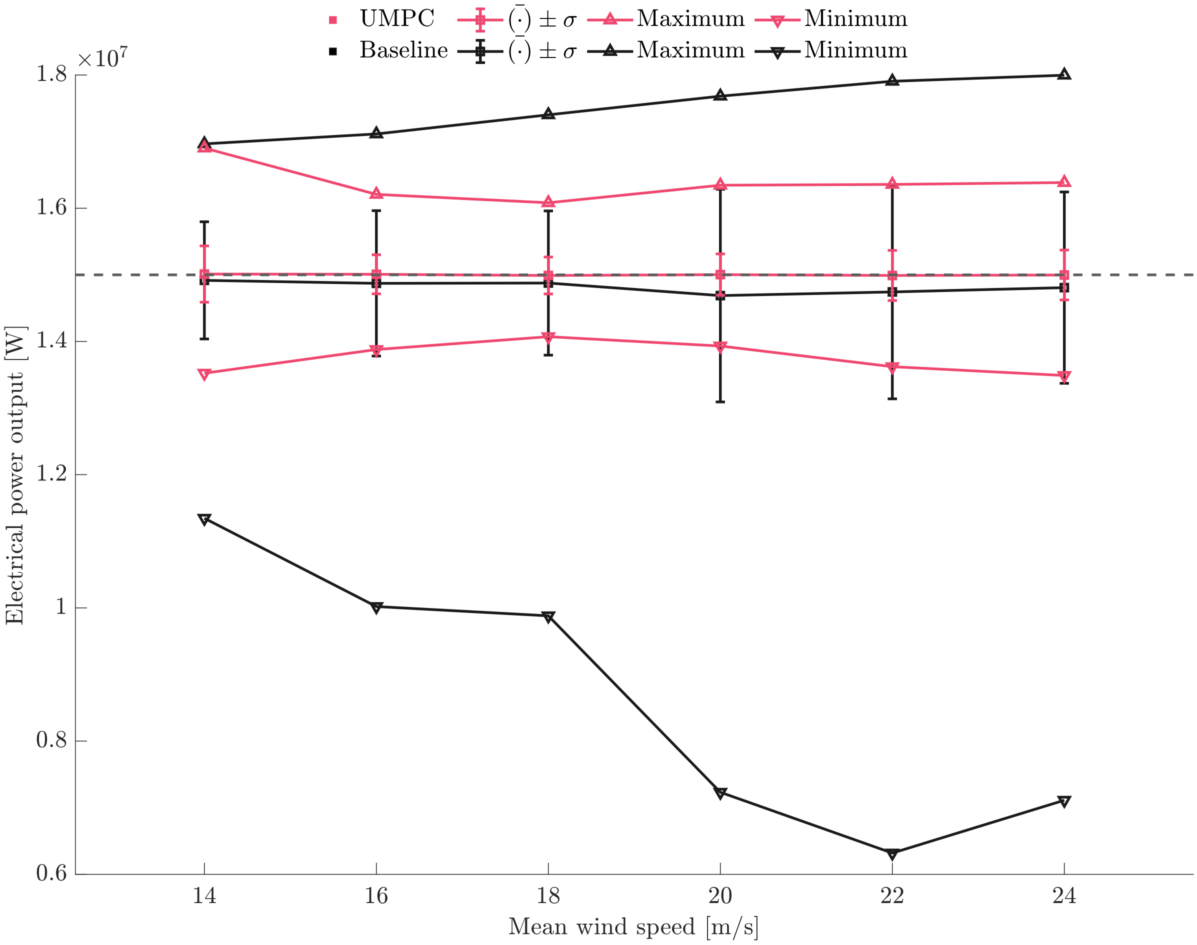

Figure 6.2: Statistical analysis of electrical power output for above rated wind speeds, under turbulent wind simulations $TI = 10\%$. The dashed line corresponds to the rated electrical power.

aspect falls out of the scope of the current thesis.

6.2.2 Load analysis

The statistical analysis of the load channels considered, edgewise and flapwise BRM, tower-base fore-aft and side-side moments, and shaft torsion are shown in Figure 6.5.

The BRMs are not significantly affected by the use of MPC. This is mainly due to considering the rotor as a point actuation in the reduced-order model. Therefore, the controller does not consider the motion of the blades, nor the loads acting individually on each of them. The small changes are mainly due to the effect of rotor and collective blade pitch on such loads. The in-plane (edgewise) BRM is mainly driven by the gravity force, and thus, the loads remain almost exactly the same for both controllers. As it was outlined in the literature review, tackling load alleviation of BRM likely requires a more advanced reduced order model, and the use of Non-linear MPC combined with IPC.

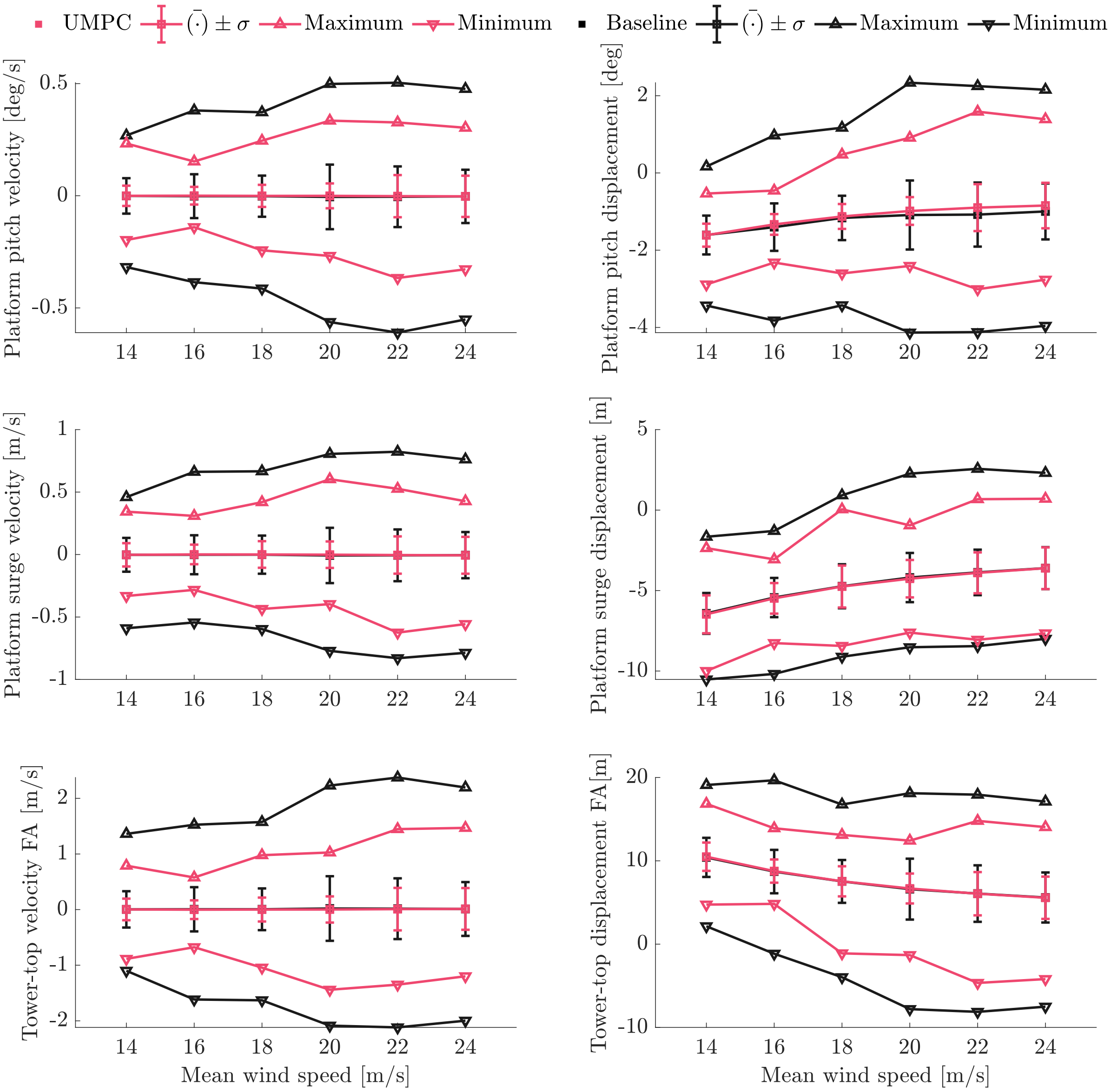

Figure 6.3: Statistical analysis of symmetrical motions (surge, pitch and tower-top FA), under turbulent wind simulations $TI = 10\%$.

The tower-base moments (TbM) are shown to change with the use of MPC. The mean values coincide, but the standard deviation is much lower for the MPC-case. One of the possible causes is the great reduction in the platform motions. This motion reduction limits the moment-arm causing gravity moments due to pitch and roll displacements.

The aerodynamic torque and thrust force remain fairly similar, as it can be observed in Figure 6.6. The slight increase in the maximum and standard deviation values of thrust, and marginal improvements in the aerodynamic torque, would not explain the performance improvement.

The shaft moment shows the largest change as compared to the baseline, caused by

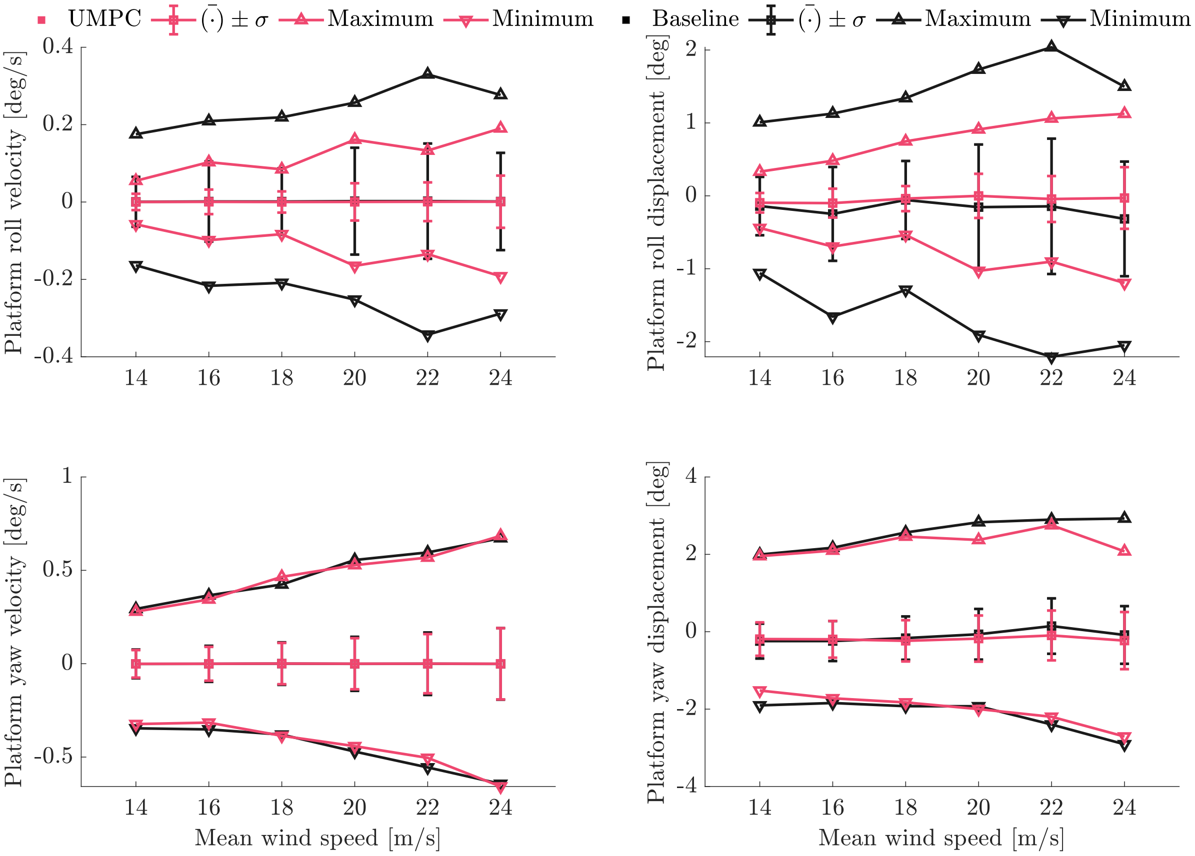

Figure 6.4: Statistical analysis of non-symmetrical motions (roll and yaw), under turbulent wind simulations $TI = 10\%$.

keeping constant generator torque throughout the operation, in contrast to continuous changes in the baseline controller. Furthermore, limited oscillations in the rotor speed can be linked to a reduction in the shaft torsion, due to the reduced relative changes in aerodynamic torque with respect to the generator torque, driving the shaft torsional loading.

The load analysis can be extended by considering both fatigue and extreme loads. The fatigue loads are considered through short-term DELs and shown in Figure 6.7. The flapwise and edgewise fatigue are similar for the baseline controller and MPC case, which could be expected based on previous results.

On the other hand, tower-base fore-aft and side-side moments' short-term DELs are consistently improved with respect to the reference controller. As mentioned earlier, the platform motion minimisation is likely the main driver of such improvement. Furthermore, reduction in generator torque oscillations are highly beneficial in terms of tower base side-side fatigue. Reduced short-term DELs will likely result in a significant life-time fatigue load reduction, that coupled with the power capture improvement, would yield a LCoE reduction. Quantifying it would require further analysis, available design data, and consideration of the whole operation range.

Following the fatigue load analysis, the extreme values are computed at each wind

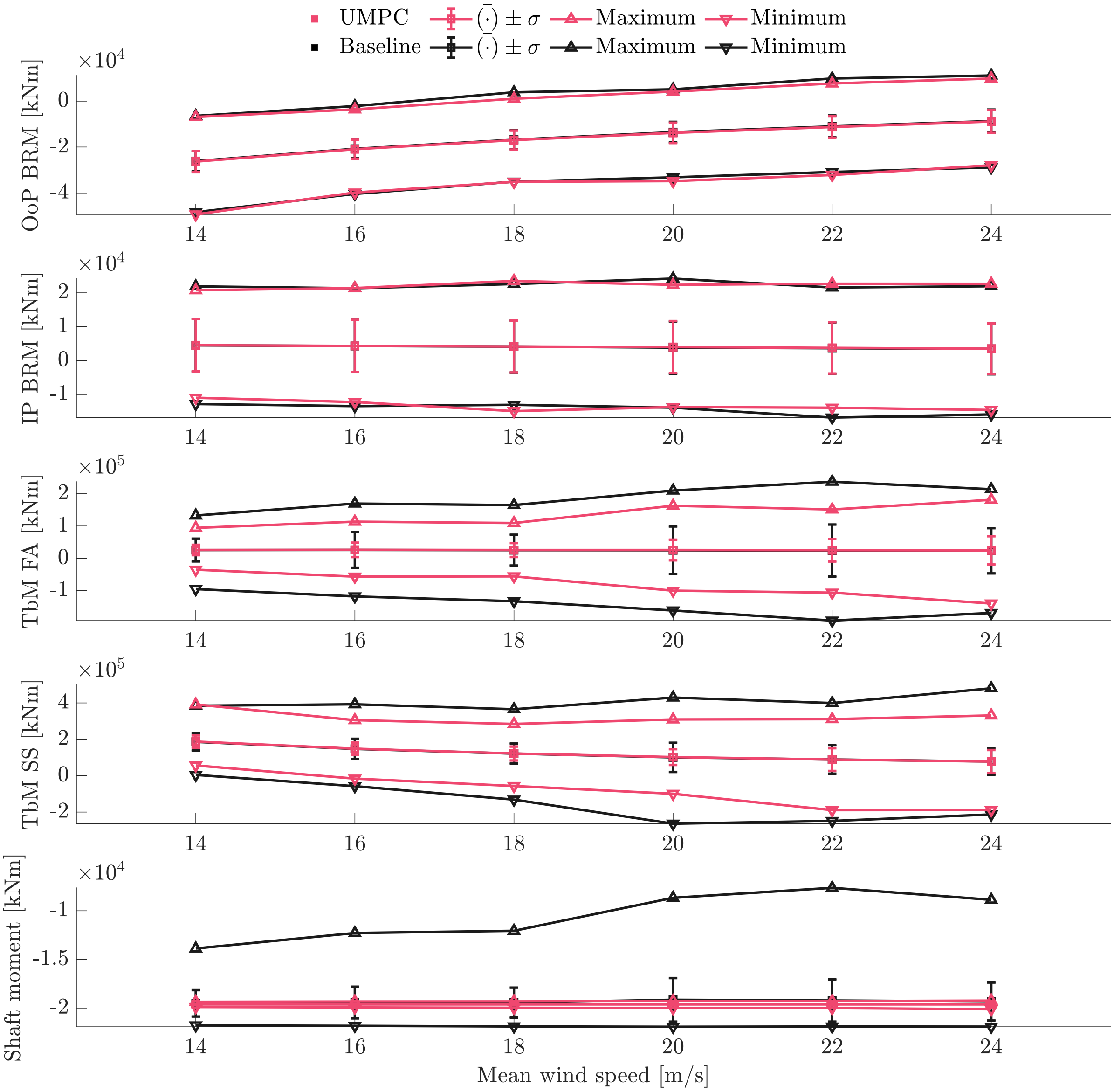

Figure 6.5: Statistical analysis of load channels for above rated wind speeds, under turbulent wind simulations $TI = 10\%$.

speed for the most relevant channels. Then, they are normalised with the baseline PI controller with torque compensation. Some of the operational variables and the aerodynamic loads are shown in Figure 6.8.

The rotor speed extreme value is taken as the largest positive value. Marginal improvements with respect to the baseline are attained for wind speeds beyond 16 m/s, however a larger maximum value appears at $\bar{V}_\infty = 14$ m/s, which is not translated into larger electrical power output, due to the constant generator torque approach.

The demanded pitch rate presents peaks at $\bar{V}_\infty = 14$ m/s and $\bar{V}_\infty = 24$ m/s. This could be further addressed by improving the re-tuning in the former, and re-tuning for the

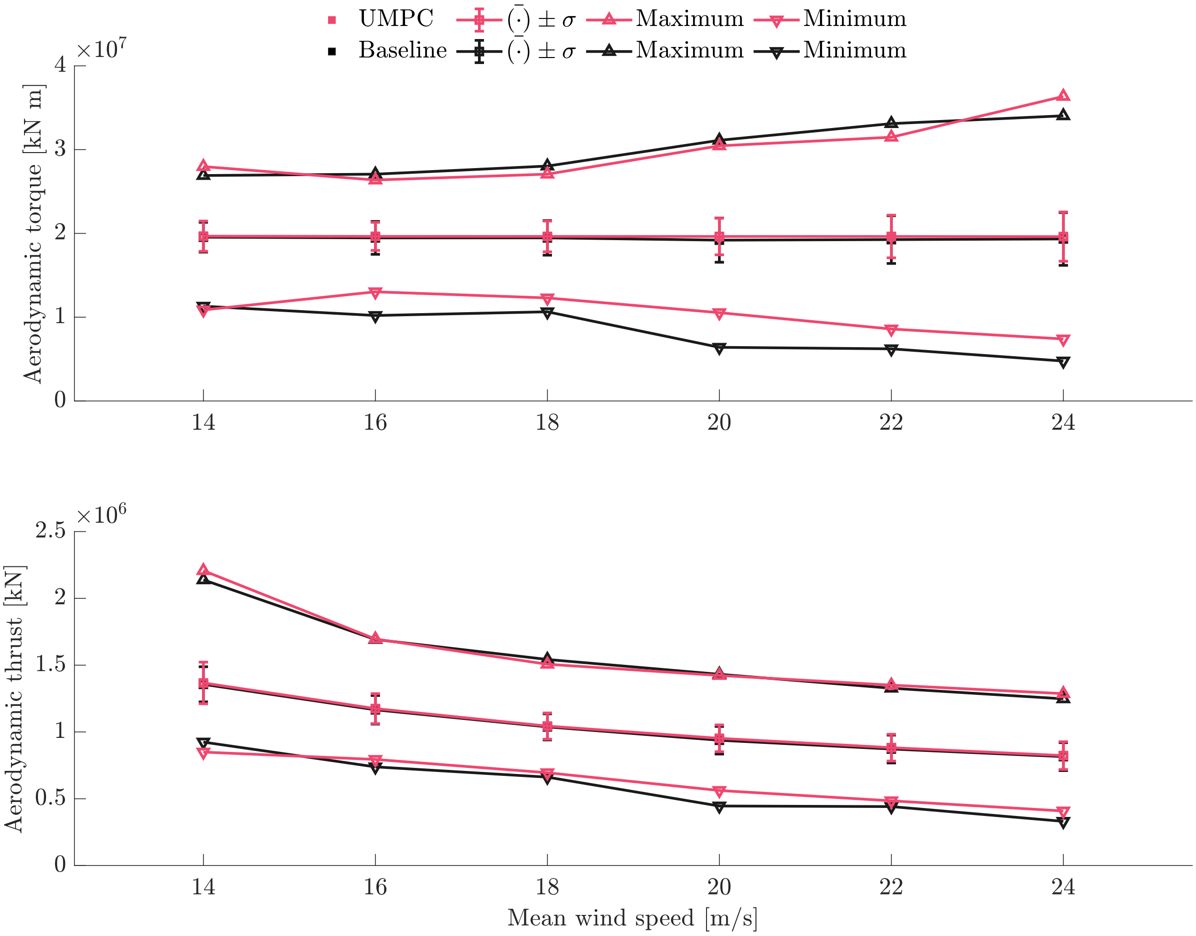

Figure 6.6: Statistical analysis of aerodynamic load channels for above rated wind speeds, under turbulent wind simulations $TI = 10\%$.

latter wind speed. The wind speeds between 16 m/s and 20 m/s show a reduced extreme value, which justifies the decision of not including hard constraints for the analysis, since the demanded pitch rate is always well below the limits.

The maximum aerodynamic loads show an analogous trend to the demanded pitch rate, which again agrees with the unsteady aerodynamic loading hypothesis presented in the tuning procedure. Further analysis of the aerodynamic channels, such as axial and tangential induction, angle of attack, lift and drag coefficients at different span-wise locations could shed light in the importance of dynamic stall and dynamic inflow in the extreme loads during operation at different wind speeds for the analysed controllers. However, due to time limitations, this aspect falls out of the scope of the thesis.

The extreme values of the platform and tower-top velocities are shown in Figure 6.9. All the channels except the yaw velocity show great improvements with respect to the baseline. The platform surge velocity is particularly reduced for all wind speeds, despite not being directly tackled by the controller. Considering the reduction in platform pitch motion, such improvement could originate from the strong coupling of pitch and surge. Additionally, the baseline controller was found to trigger, shortly, platform pitch

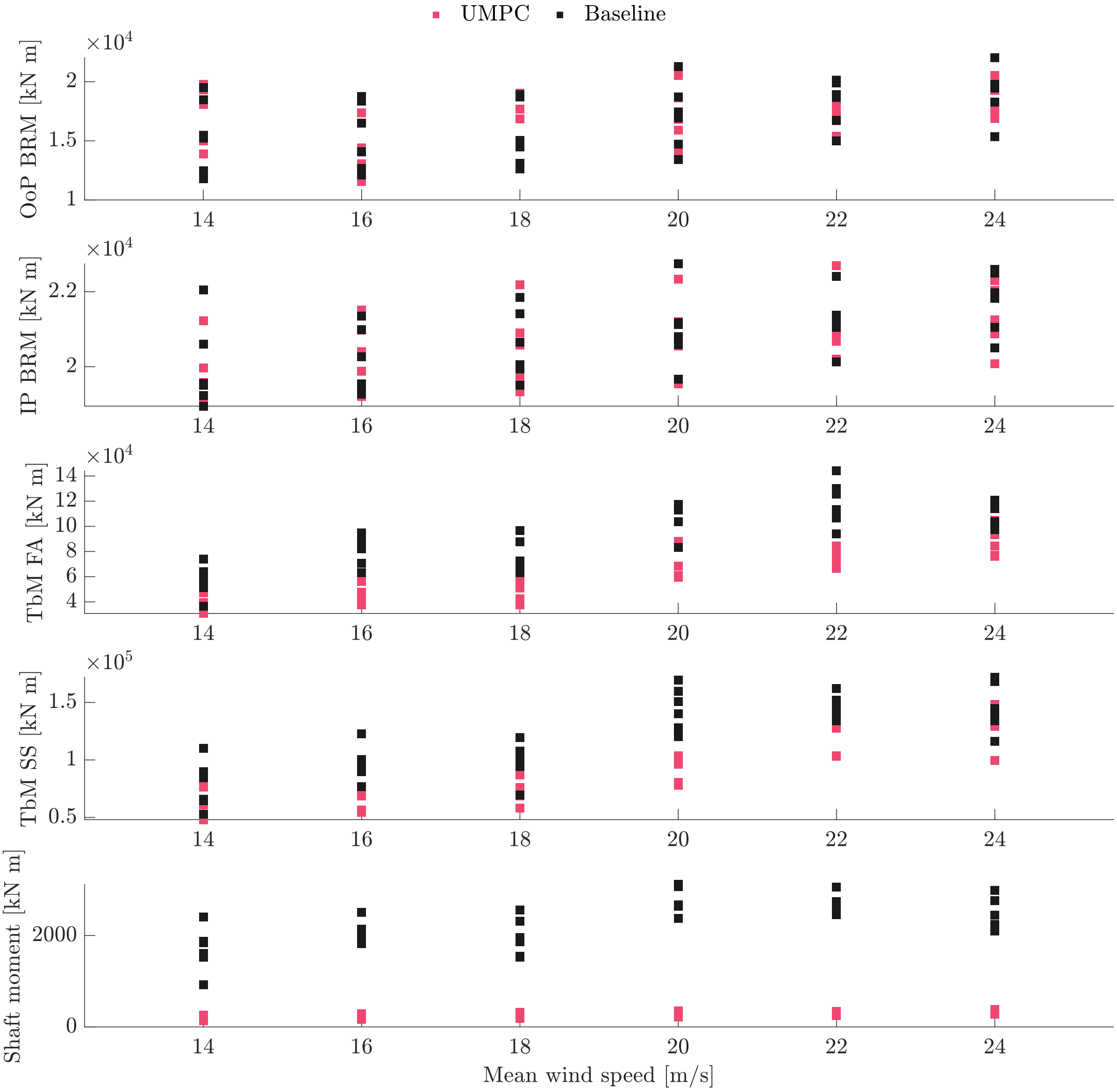

Figure 6.7: Short-term DELs of load channels for above rated wind speeds, under turbulent wind simulations $TI = 10\%$.

instability near rated wind speeds, which significantly affects the extreme values.

Consistent reduction in platform pitch maximum velocity is observed, especially at $\bar{V}_\infty = 16$ m/s. These improvements directly drive reduction in the tower-top motion. The roll and yaw motions follow the trends found in the statistical analysis, with major reduction for roll and not significant changes in yaw. These improvements should not be taken for granted, and further analysed with active wave disturbances. Although it is not analysed in this project, the mooring line loads are expected to be significantly reduced by the motion reduction. This aspect could be further studied, since the optimal mooring line design is of high importance to drive the floating wind energy costs down.

Finally, the extreme values of the load channels per wind speed are shown in Fig-

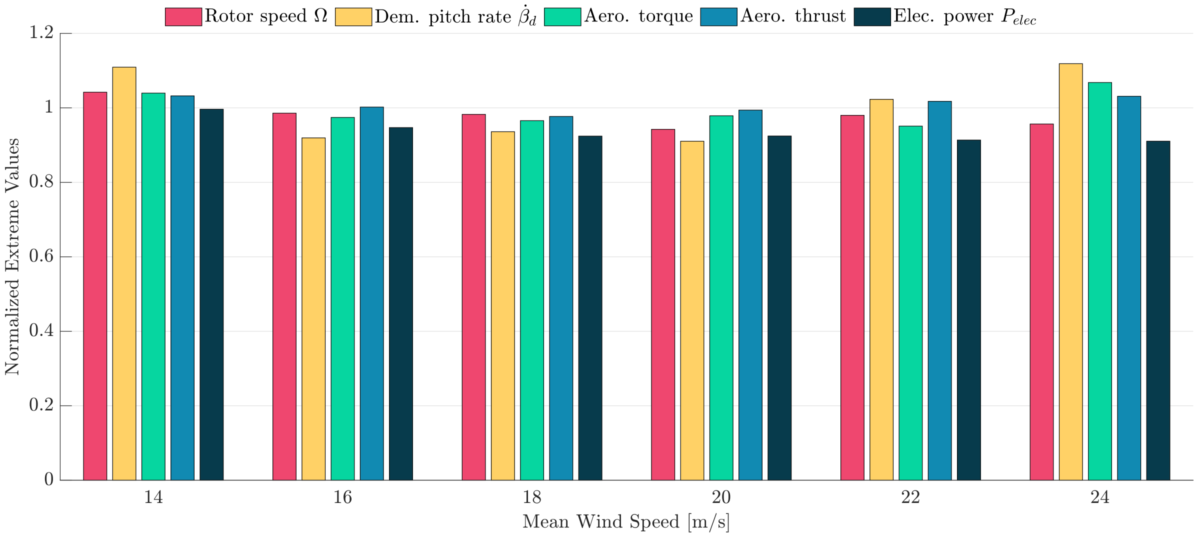

Figure 6.8: Normalised extreme values of rotor speed, demanded blade pitch rate, electrical power and aerodynamic load channels for above rated wind speeds, under turbulent wind simulations $TI = 10\%$.

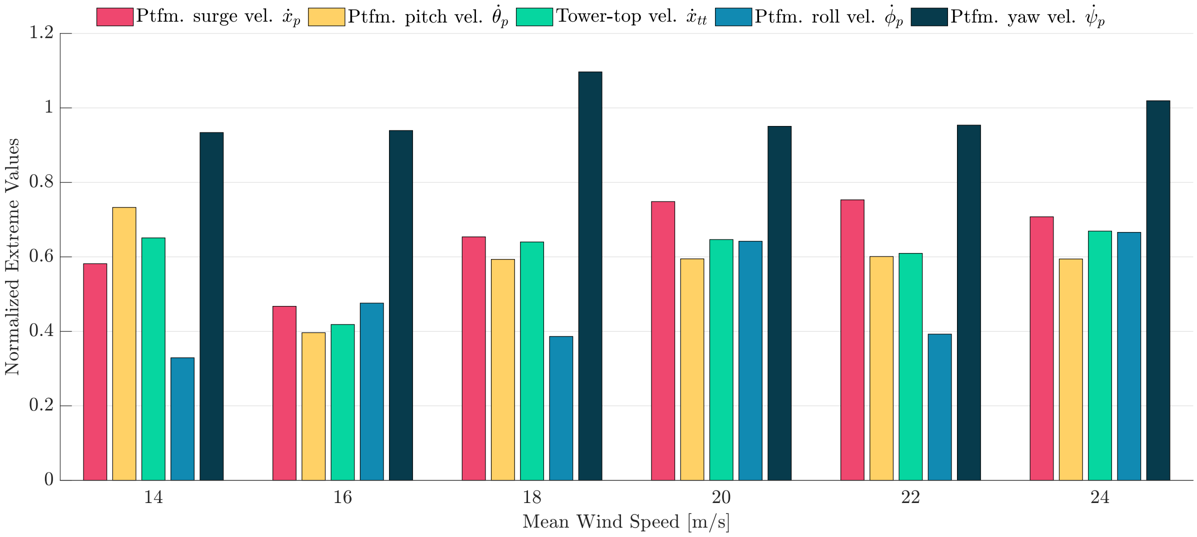

Figure 6.9: Normalised extreme values of platform and tower-top velocity channels for above rated wind speeds, under turbulent wind simulations $TI = 10\%$.

ure 6.10. The BRMs are fairly similar to the baseline for all wind speeds, which is consistent with the findings in the literature. It seems evident that further MPC developments would be needed to tackle the blade loads, however, this may negatively influence the power quality and the platform motions if the trade-offs are not treated carefully during the tuning procedure. On the other hand, the reduction in tower-base fore-aft moment is significant for all wind speeds considered, whereas an increase in the side-side case is observed at $\bar{V}_\infty = 14$ m/s, which could be driven by a higher rotor speed overshoot and maximum aerodynamic torque. Since the roll motion is greatly reduced, especially at that wind speed, it is not considered to drive the relative increase. The shaft moment is consistent with the relative difference between the maximum generator torque set for the baseline controller, and the constant rated generator torque set for the MPC case.

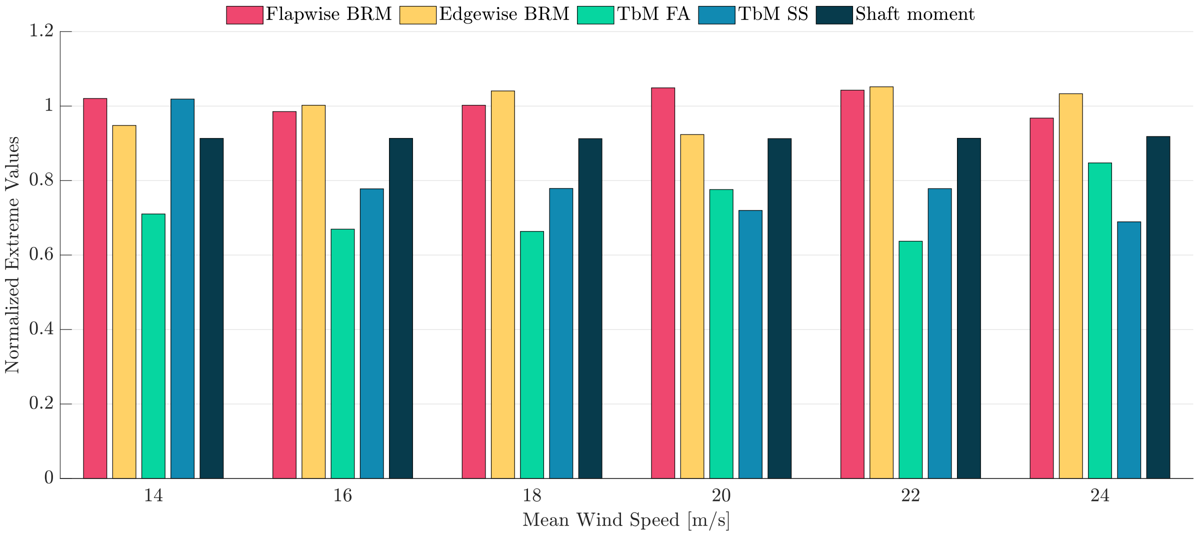

Figure 6.10: Normalised extreme values of relevant load channels for above rated wind speeds, under turbulent wind simulations $TI = 10\%$.

Design considerations require the absolute extreme loads, independently of wind speed. A comparison is displayed in Figure 6.11. The values are consistent with the previous analysis. The controller is able to significantly limit the tower-base and shaft moments, while maintaining similar extreme loads on the blades. Taking into account the great improvements in platform motions and power quality it is evident that MPC can tackle several objectives simultaneously, and improve the control of floating wind turbines for above rated wind speeds.

6.3 On the effect of met-ocean conditions and additional aerodynamic effects

The previous load calculations conveyed a series of assumptions such as neglecting wind shear, tower shadow effects, drag on the nacelle and tower, and, even more importantly, waves. The former effects are not included in the reduced order model, and the wave loads are not estimated, since the extended Kalman filter would require further development and validation.

To explore the effect of this assumptions on the controller performance, two sets of six random simulations are run in HAWC2 and compared. Firstly, the tower shadow effect is included through a potential flow formulation included in HAWC2, the drag force on the nacelle and tower is also evaluated in the model and wind shear is added in the wind field generation using the IEC standard power law with 0.2 exponent for fatigue loads.

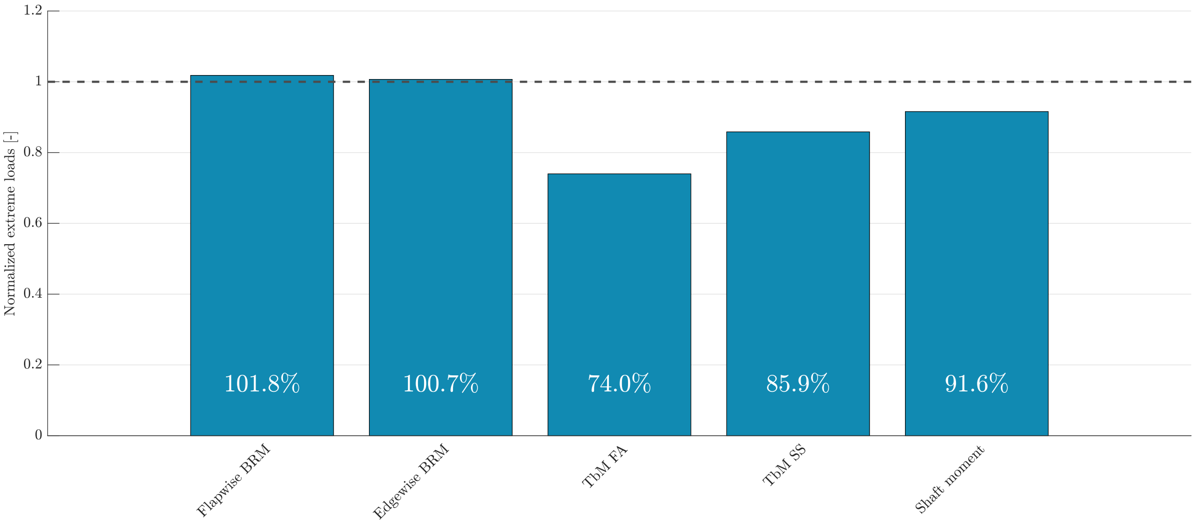

Figure 6.11: Normalised extreme absolute values of relevant load channels for above rated wind speed, under turbulent wind simulations $TI = 10\%$

Then, the second set of simulations considers irregular waves as well. They are generated using a JONSWAP spectrum [67], with significant wave height $H_s = 2$ m, peak-wave period $T_p = 6$ s and peakedness factor $\gamma = 3.3$. The wind speed and turbulence is chosen again as $\bar{V}_\infty = 16$ m/s, and $TI = 10\%$, based on the best observed performance.

The simulations are shown in Figure 6.12. The MPC results are normalised with the corresponding simulations for a baseline controller. The normalised standard deviation results (top figure) show that rotor speed tracking performance deteriorates significantly, most likely due to wind shear, although drag and tower shadow effects may play a minor role. Further deterioration is seen when waves are added to the simulations. Though the platform motions are relatively worsened, the performance is still significantly better than the baseline controller. Minor effects are seen on the demanded pitch and out-of-plane loads.

The extreme values (bottom figure) illustrate interesting trends. The maximum rotor speed overshoot is slightly larger compared to the counter-part baseline simulations when including the aforementioned effects. Similarly, the demanded pitch rate increases, particularly when waves are added. On the other hand, platform surge and pitch velocities are largely affected by wind shear, but not by waves. Although this may seem counter intuitive, the waves are fairly mild, and likely the enhanced shear compromises the capabilities of the extended Kalman filter to estimate the wind speed, leading to under-predictions (not shown here for conciseness). In fact, that would directly explain the lower maximum blade pitch angle, thus resulting in significantly higher relative maximum out-of-plane loads.

The presented analysis leads to proposing the further development of the extended Kalman filter to properly estimate the wind speed under realistic conditions. Therefore, it is necessary to improve the aerodynamic modelling of the rotor. Wave estimation must be considered as well, since it is expected to play a major role under more severe wave conditions.

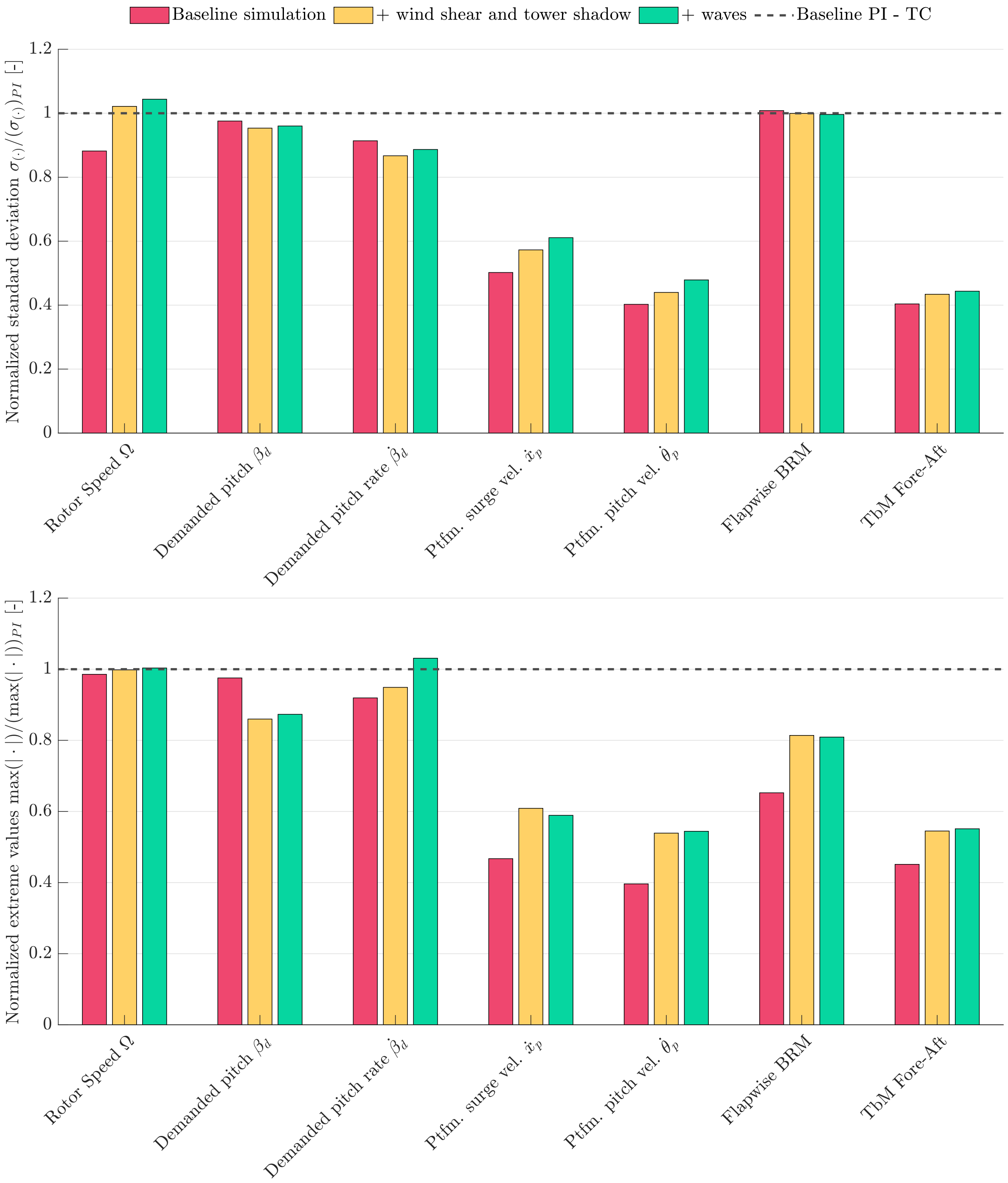

Figure 6.12: Comparison of relevant channels for $\bar{V}_\infty = 16$ m/s with $TI = 10\%$ when including additional met-ocean conditions: (top) normalised standard deviation, and (bottom) normalised extreme values. Added wind shear with power law, exponent 0.2; added waves follow JONSWAP spectrum, $H_s = 2$ m, $T_p = 6$ s and $\gamma = 3.3$.

CHAPTER 7

Conclusions

7.1 Discussion

The thesis project has addressed some of the main challenges floating offshore wind energy is facing. A review of low-order modelling approaches was provided, with the focus set on the control-oriented models. The use of first-principles was exemplified by two existing models, and, based on said models, the derivation of a slightly more complex model has been presented.

The two models used for validation considered two DOFs for the platform, namely surge and pitch, aiming at capturing the symmetric motions of the floating platform. Additionally, both contained the rotor speed DOF regarding the rotor. The existing simplified model assumed a rigid tower, whereas the extended model added flexibility to it. The mathematical representation of such models was linearised to fit control design purposes, resulting in a convenient state-space formulation, presented in section 2.3 and section 2.4.

To validate the models, the higher fidelity hydro-servo-aero-elastic code HAWC2 was used. A model of the WindCrete SB, combined with the IEA-15MW RWT has been simulated in both open-loop and closed-loop configurations. Firstly, the key parameters were presented, and various methods to compute structural and hydrodynamic characteristics of the FOWT were compared. Then, closed-loop simulations were employed to compute the aerodynamic gradients needed for the linear models, using a finite difference approach. The robustness of this method has been evaluated by performing a sensitivity analysis on the involved parameters, shown in Figure 3.6. The main observation is the expected effects of the highly non-linear aerodynamics in the computation of the derivatives under different operating conditions, especially in terms of aerodynamic thrust force. Such derivatives showed variations of more than 5% for a 0.5 m/s change in wind speed.

The reduced order models were simulated under identical wind conditions to the HAWC2 model, resulting in a good match in terms of frequency of the response and overshoot amplitude, particularly for the platform pitch motion and the rotor speed, and a less degree of accuracy for the platform surge and the tower-top motion, as shown in Figure 3.11. However, it was found that further tuning the model parameters, specifically the mooring line stiffness and viscous damping terms, can yield a better agreement. It was presumed that the model is suited for platform pitch motion minimisation and rotor speed tracking, the driving controller objectives for the model-based controller formulated.

The use of MPC to improve the FOWT performance has been considered in the literature, however conflicting trade-offs are observed in the results. For instance, minimising the platform motions generally leads to higher level of demanded blade pitch, which in turn can result in actuator wear. However, a tuning procedure to address said conflicts for FOWT has not been presented to the knowledge of the author. In order to shed light in the development of such method, a simple linear MPC is developed, based on the linear models.

The model predictive controller consists of an observer, in the form of an augmented dynamic Kalman filter, and a regulator, the objective function to be solved to compute the optimal control actions. The augmented dynamic Kalman filter has been evaluated with HAWC2 simulations, validating the estimation of both unmeasured states and wind inflow. The wind speed trends were correctly captured. The estimation of wave loads has not been addressed. Afterwards, the objective function terms used in the thesis were presented, followed by the derivation of the least-squares problem in matrix form. Based on said derivation, several tuning parameters are identified, namely the receding horizon length, the platform pitch and rotor speed weights, and the blade pitch rate penalty.

Computing an optimal set of tuning parameters is not a self-evident task. In [80, 81] two different approaches were proposed, based on the KPIs sensitivity to the weights and computing Pareto fronts by means of several coupled simulations, respectively. The approaches were applied to onshore wind turbines. In this work, time series of platform motions and rotor speed have been employed to identify unstable performance, and thus limiting weights. Pareto fronts were computed to define the optimal range of weights by comparing the standard deviation of tower-top motion, rotor speed and demanded blade pitch rate. Finally, the load fluctuations are also analysed to inform the tuning choice.

These procedure showed several relevant findings. The use of steady or step-wind simulations seems to result in fairly low values of blade pitch rate penalty and rotor speed tracking weight, while resulting in a satisfactory response. However, turbulent wind simulations with low TI (4%) showed that larger penalties are needed to tackle platform motions in said scenario. Furthermore, the estimator plays a major role in the results. In fact, the optimal tuning points towards high penalty values, $S_{\Delta\beta_d} \approx 1500$, since lower values, $S_{\Delta\beta_d} \approx 500$, triggered instability in the rotor speed response. In contrast, simulations without a Kalman filter under steady, step and turbulent wind showed good performance for $S_{\Delta\beta_d}$ well below 500. Additionally, a coupling between large demanded blade pitch rate fluctuations and increasing flapwise BRM has been identified, which once again sets again a lower bound to the allowable actuation penalty. This effect is most likely associated to dynamic stall, though further analysis is required to validate this conclusion.

Furthermore, it has been found that the TI plays a relevant role in the optimal fine-tuning of MPC weights and penalties, especially near the rated wind speed. An average wind speed of 14 m/s was considered, and an equivalent tuning procedure was applied at a higher TI of 10%. A comparison of the Pareto fronts showed significant changes. The shape shows, qualitatively, a clear reduction in the stability of the system. A relatively small offset in the weight will result in a large performance deterioration, in contrast to the lower turbulence case. This issue has been identified through the load analysis, and resulted in a wind-speed specific tuning at 14 m/s, clearly indicating that *weight-scheduling* is necessary to further optimise the performance of linear MPC.

Based on these findings, the tuning of the controller for the subsequent load analysis is performed under turbulent wind simulations with TI 4% between 16 and 24 m/s, and TI 10% at 14 m/s. A parallel compensation PI controller, based on torque compensation is used as a baseline to assess the newly developed controller performance. The load analysis is based on DLCs 1.1 and 1.2 of IEC 61400-1 for extreme and fatigue loads. Due to the lack of augmented dynamic Kalman filter validation for wave load estimation, the sea-state conditions are not included. Furthermore, the TI is set at 10% below the one corresponding to the wind turbine class, mainly driven by a poor performance of the baseline controller in several KPIs for high turbulence conditions.

The load analysis results, in section 6.2, showcase the great improvements that can be achieved by linear MPC in terms of power, load alleviation and platform motion minimisation. The tuning of the controller focuses specially on the latter, which couples most of the floating wind turbine performance indicators. The platform pitch instability is one of the main challenges on the operation, and tackling this issue with the use of a de-tuned PI controller, or the addition of a feedback loop to the tower-top velocity seems limited to the extent explored.

The use of linear MPC with a simplified model yields clear benefits above rated-wind speeds. The rotor speed oscillations and the overshoot are consistently lower, for wind-speed simulations from 16 to 24 m/s. Coupled with the use of constant generator torque, in contrast to the baseline controller, a significant decrease in electrical power oscillations and overshoots is reached. Furthermore, the mean power output is kept at the rated power level, 15 MW, throughout the explored wind speeds, in contrast to a lower mean power production of the baseline, directly improving the AEP of the WTG when using MPC.

The platform motions are minimised, specially in the pitch DOF, which is the main objective of the controller, explicitly stated in the objective function. The performance improvement is evident at mean wind speeds between 14 and 20 m/s, however the oscillations increase at very high wind speeds. The possible reason behind this is the use of the same MPC tuning throughout the studied operating range. The surge performance is also improved, which could be expected by the existing coupling between platform pitch and surge, leading to an overall reduction in the tower-top fore-aft velocity, which enables the controller to better track the rotor speed oscillations due to the smaller changes in rotor effective wind speed.

Additionally, the antisymmetric motions of the platform, roll and yaw, were compared for the two controllers. The yaw motion showed no improvements, since the simulations did not consider wind misalignment, therefore the observed motions originate from the generator torque and antisymmetric loading, such as blade gravity, and coupling effects between roll and side-side motions of the platform and tower respectively. The roll velocity and displacements are significantly reduced by the controller. The use of constant generator torque is the main driver of this improvement, in contrast with the use of generator torque actuation above rated wind speeds by the baseline controller.

The blade-root, tower-base and shaft moments are analysed to understand whether lower fatigue and extreme loads can be attained by using linear MPC without clearly defining the load-alleviation goal in the objective function. The BRMs show the same trends and practically the same values, as compared to the baseline. The edgewise remains fairly constant, as expected since the main driver is the gravity load. On the other hand, the flapwise BRM is affected by the axial loading, mainly the aerodynamic thrust force acting on the rotor, and a marginal deterioration of its extreme value has been quantified.

Finally, several effects that were not included in the load case analysis have been included to provide a set of priorities in the further development of the controller. The effect of wind shear has been found to drive significant changes in rotor speed and platform motion performance, as well as a significant effect on the extreme values of platform velocities, flapwise BRM and tower-base moment in fore-aft direction. The simulated waves show a clear impact in platform motion fluctuations and the extreme value of demanded blade pitch rate. Therefore, it is expected that further developing the model will allow performance increase under real-world conditions, by means of adequately estimating wind and wave disturbances, and accurately formulating predictions used in the computation of the optimal control problem.

7.2 Further development and validation road-map

This project dealt with the derivation and implementation of reduced order models and a MPC. The first aspect of it proved more complicated than expected, especially attempting the development of a new model using flexible multi-body dynamics and analytical mechanics. The model was partly developed and documented as part of the thesis project, but not completed. Further work could either attempt to finish such model, or derive a model coupling all platform degrees of freedom, in order to tackle the roll-yaw lock instability, or platform motion minimisation.

The development of MPC has been divided into two parts: the estimator and the regulator. The estimator can potentially be extended to estimate wave loads, which in turn should greatly benefit the regulator activity under wave excitation. Additionally, it was found that further work is needed to properly estimate the wind speed when wind shear is present.

The regulator has been developed to address the MIMO problem, however, the lack of hard constraints limited the utilisation of generator torque together with blade pitch. It is possible to further develop the MPC to include such constraints. Furthermore, this would allow to implement the derivation performed for constant power approach, although not shown here for conciseness.

Additionally, coupled MATLAB-HAWC2 simulations were required to analyse the controller performance. To that purpose two separate tool-boxes have been developed, shown in Figure 7.1 and Figure 7.2. These tools have proven very valuable in addressing the thesis' goals. However, further development can elevate the applicability and ease the development of further improved model-based controllers. To that purpose, a series of proposed developments are listed in each diagram.

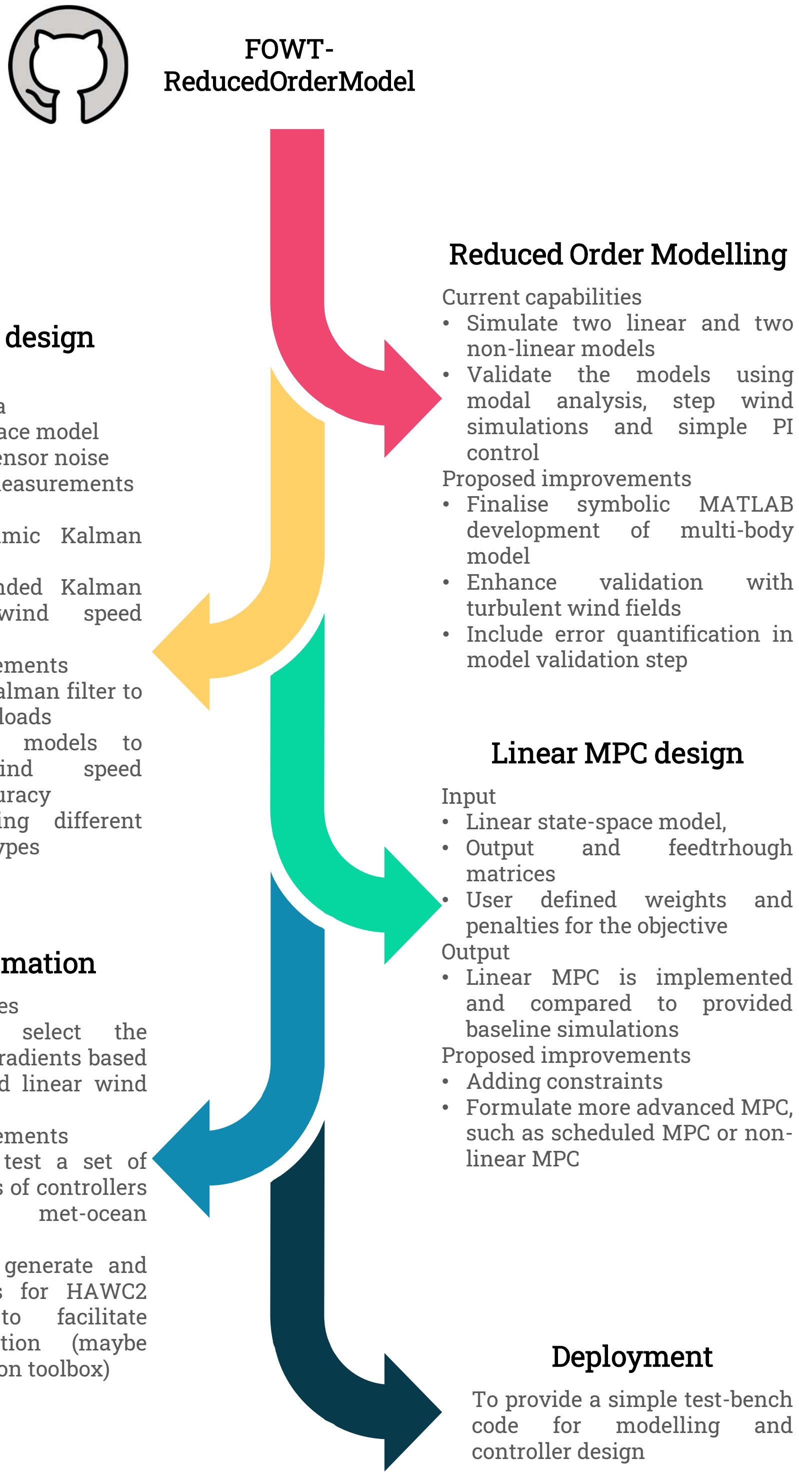

Reduced Order Modelling

Current capabilities
- Simulate two linear and two non-linear models
- Validate the models using modal analysis, step wind simulations and simple PI control

Proposed improvements
- Finalise symbolic MATLAB development of multi-body model
- Enhance validation with turbulent wind fields
- Include error quantification in model validation step

Estimator design

Input
- Simulation data
- Linear state-space model
- User-defined sensor noise
- User-defined measurements

Output
- Validate Dynamic Kalman Filter
- Validate Extended Kalman Filter for wind speed estimation

Proposed improvements
- Augmenting Kalman filter to estimate wave loads
- Validate new models to increase wind speed estimation accuracy
- Consider adding different Kalman filter types

Linear MPC design

Input
- Linear state-space model,
- Output and feedtrhough matrices
- User defined weights and penalties for the objective

Output
- Linear MPC is implemented and compared to provided baseline simulations

Proposed improvements
- Adding constraints
- Formulate more advanced MPC, such as scheduled MPC or non-linear MPC

Code automation

Current capabilities
- Automatically select the aerodynamic gradients based on user-defined linear wind speed

Proposed improvements
- Automatically test a set of gains / weights of controllers for different met-ocean conditions
- Automatically generate and run HTC files for HAWC2 simulations to facilitate model validation (maybe linking to Python toolbox)

Deployment

To provide a simple test-bench code for modelling and controller design

Figure 7.1: Proposed development road-map for self-developed GitHub repository *FOWT-ReducedOrderModel*

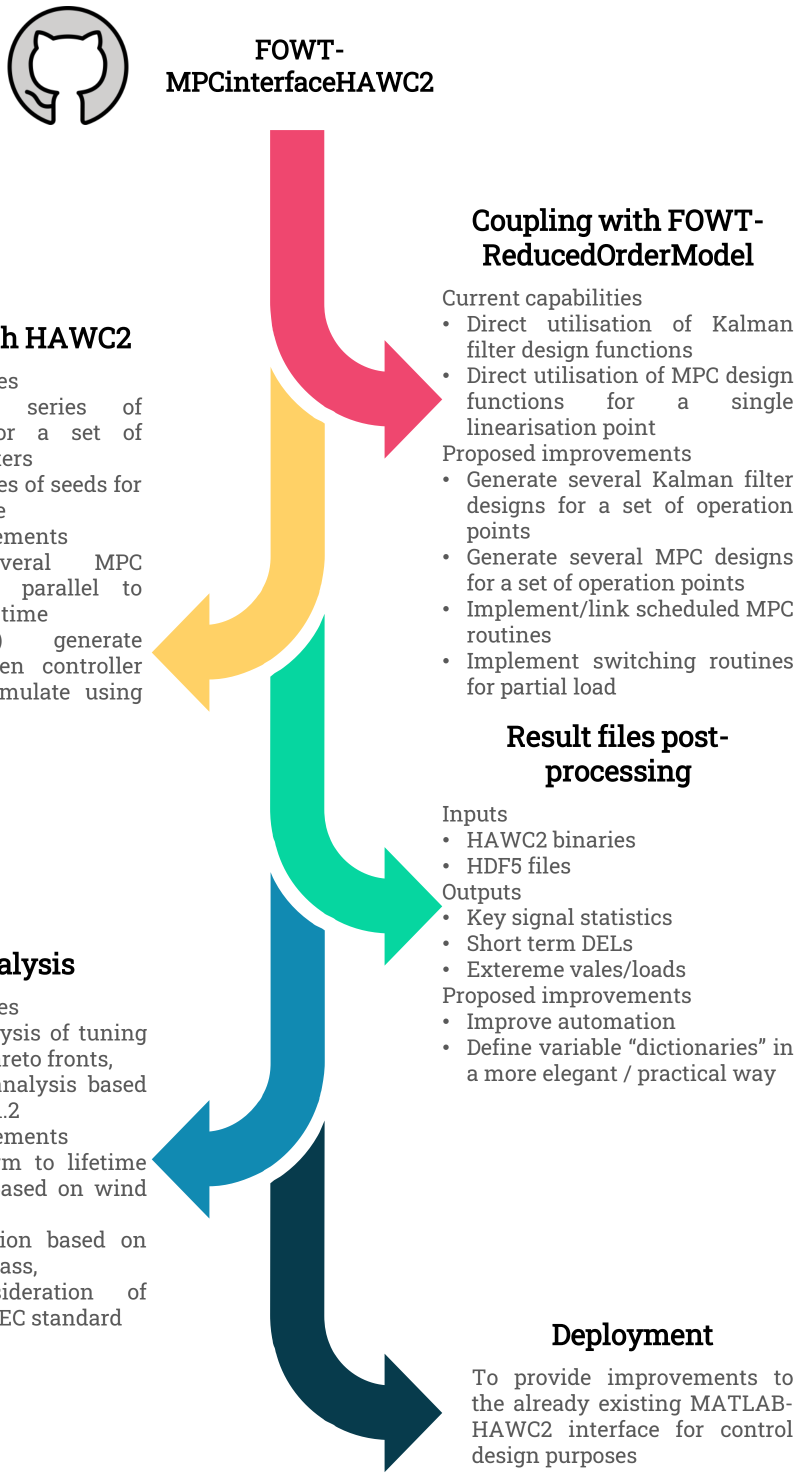

FOWT-MPCinterfaceHAWC2

Coupling with FOWT-ReducedOrderModel

Current capabilities
- Direct utilisation of Kalman filter design functions
- Direct utilisation of MPC design functions for a single linearisation point

Proposed improvements
- Generate several Kalman filter designs for a set of operation points
- Generate several MPC designs for a set of operation points
- Implement/link scheduled MPC routines
- Implement switching routines for partial load

Coupling with HAWC2

Current capabilities
- Simulate in series of simulations for a set of tuning parameters
- Simulate a series of seeds for a given HTC file

Proposed improvements
- Simulate several MPC controllers in parallel to reduce waiting time
- (Automatically) generate DLL from given controller and tune / simulate using HAWC2

Result files post-processing

Inputs
- HAWC2 binaries
- HDF5 files

Outputs
- Key signal statistics
- Short term DELs
- Extereme vales/loads

Proposed improvements
- Improve automation
- Define variable “dictionaries” in a more elegant / practical way

Load analysis

Current capabilities
- Statistical analysis of tuning sets through Pareto fronts,
- (Partly) Load analysis based on DLC 1.1 and 1.2

Proposed improvements
- From short-term to lifetime fatigue loads based on wind turbine class,
- AEP computation based on wind turbine class,
- Further consideration of offshore wind IEC standard

Deployment

To provide improvements to the already existing MATLAB-HAWC2 interface for control design purposes

Figure 7.2: Proposed development road-map for self-developed GitHub repository *FOWT-MPCinterfaceHAWC2*

Bibliography

[1] K. Calvin, D. Dasgupta, G. Krinner, A. Mukherji, P. W. Thorne, C. Trisos, J. Romero, P. Aldunce, K. Barrett, G. Blanco, W. W. Cheung, S. Connors, F. Denton, A. Diongue-Niang, D. Dodman, M. Garschagen, O. Geden, B. Hayward, C. Jones, F. Jotzo, T. Krug, R. Lasco, Y.-Y. Lee, V. Masson-Delmotte, M. Meinshausen, K. Mintenbeck, A. Mokssit, F. E. Otto, M. Pathak, A. Pirani, E. Poloczanska, H.-O. Pörtner, A. Revi, D. C. Roberts, J. Roy, A. C. Ruane, J. Skea, P. R. Shukla, R. Slade, A. Slangen, Y. Sokona, A. A. Sörensson, M. Tignor, D. van Vuuren, Y.-M. Wei, H. Winkler, P. Zhai, Z. Zommers, J.-C. Hourcade, F. X. Johnson, S. Pachauri, N. P. Simpson, C. Singh, A. Thomas, E. Totin, A. Alegría, K. Armour, B. Bednar-Friedl, K. Blok, G. Cissé, F. Dentener, S. Eriksen, E. Fischer, G. Garner, C. Guivarch, M. Haasnoot, G. Hansen, M. Hauser, E. Hawkins, T. Hermans, R. Kopp, N. Leprince-Ringuet, J. Lewis, D. Ley, C. Ludden, L. Niamir, Z. Nicholls, S. Some, S. Szopa, B. Trewin, K.-I. van der Wijst, G. Winter, M. Witting, A. Birt, and M. Ha, "Climate Change 2023: Synthesis Report," Intergovernmental Panel on Climate Change, Tech. Rep., 7 2023. [Online]. Available: https://www.ipcc.ch/report/ar6/syr/

[2] E. Foote, "Circumstances affecting the heat of the Sun's rays," *The American Journal of Science and Arts, 2nd Series*, vol. XXII, no. LXVI, pp. 382–383, 11 1856.

[3] H. T. Ngo, M. Guèze, J. Agard Trinidad, A. Arneth, P. Balvanera, K. Brauman, R. Watson, I. Baste, A. Larigauderie, P. Leadley, U. Pascual, B. Baptiste, S. Demissew, L. Dziba, G. Erpul, A. Fazel, M. Fischer, A. María Hernández, M. Karki, V. Mathur, T. Pataridze, I. Sousa Pinto, M. Stenseke, K. Török, B. Vilá, M. Carneiro da Cunha, G. Mace, and H. Mooney, "Summary for policymakers of the global assessment report on biodiversity and ecosystem services of the Intergovernmental Science-Policy Platform on Biodiversity and Ecosystem Services," IPBES, Tech. Rep., 2019.

[4] IPCC, "Summary for PolicyMakers. In: Global Warming of 1.5ºC. An IPCC Special Report on the impacts of global warming of 1.5ºC above pre-industrial levels and related global greenhouse gas emission pathways, in the context of strengthening the global response to the threat of climate change, sustainable development, and efforts to eradicate poverty," IPCC, Tech. Rep., 2018. [Online]. Available: https://www.cambridge.org/core/product/identifier/9781009157940%23prf2/type/book_part

[5] World Meteorological Organization, "Global Annual to Decadal Climate Update," Tech. Rep., 2023.

[6] P. M. Forster, C. J. Smith, T. Walsh, W. F. Lamb, R. Lamboll, M. Hauser, A. Ribes, D. Rosen, N. Gillett, M. D. Palmer, J. Rogelj, K. von Schuckmann, S. I. Seneviratne, B. Trewin, X. Zhang, M. Allen, R. Andrew, A. Birt, A. Borger, T. Boyer, J. A.

Broersma, L. Cheng, F. Dentener, P. Friedlingstein, J. M. Gutiérrez, J. Gütschow, B. Hall, M. Ishii, S. Jenkins, X. Lan, J.-Y. Lee, C. Morice, C. Kadow, J. Kennedy, R. Killick, J. C. Minx, V. Naik, G. P. Peters, A. Pirani, J. Pongratz, C.-F. Schleussner, S. Szopa, P. Thorne, R. Rohde, M. Rojas Corradi, D. Schumacher, R. Vose, K. Zickfeld, V. Masson-Delmotte, and P. Zhai, "Indicators of Global Climate Change 2022: annual update of large-scale indicators of the state of the climate system and human influence," *Earth System Science Data*, vol. 15, no. 6, pp. 2295–2327, 6 2023.

[7] B. H. Jørgensen, H. Holttinen, IEA Wind Operating Agents, and IEA Wind Secretariat, "IEA Wind TCP Annual Report 2019," International Energy Agency, Tech. Rep., 8 2020.

[8] B. H. Jørgensen and H. Holttinen, "IEA Wind TCP Annual Report 2020," International Energy Agency, Tech. Rep., 8 2021.

[9] B. H. Jørgensen, H. Holttinen, IEA Wind TCP ExCo Member, and IE Wind TCP Operating Agents, "IEA Wind TCP Annual Report 2021," International Energy Agency, Tech. Rep., 2022.

[10] Oersted, "Deeper water, stronger winds. How floating offshore wind can be scaled," *White Paper*, 10 2022. [Online]. Available: orsted.com/floating

[11] Blue H Engineering, "Historical development," 2023.

[12] D. Stockhouse, M. Phadnis, A. Henry, N. Abbas, M. Sinner, M. Pusch, and L. Y Pao, "Sink or Swim: A Tutorial on the Control of Floating Wind Turbines," *IEEE Control Systems Letters presented at 2023 American Control Conference (ACC)*, 6 2023.

[13] R. Chitteth Ramachandran, C. Desmond, F. Judge, J. J. Serraris, and J. Murphy, "Floating wind turbines: marine operations challenges and opportunities," *Wind Energy Science*, vol. 7, no. 2, pp. 903–924, 4 2022.

[14] T. Moan, Z. Gao, E. E. Bachynski, and A. R. Nejad, "Recent Advances in Integrated Response Analysis of Floating Wind Turbines in a Reliability Perspective," *Journal of Offshore Mechanics and Arctic Engineering*, vol. 142, no. 5, 10 2020.

[15] T. J. Larsen and T. D. Hanson, "A method to avoid negative damped low frequent tower vibrations for a floating, pitch controlled wind turbine," in *Journal of Physics: Conference Series*, vol. 75, no. 1. Institute of Physics Publishing, 6 2007.

[16] G. J. Van Der Veen, L. J. Couchman, and R. O. Bowyer, "Control of floating wind turbines," *American Control Conference Fairmont Queen Elizabeth*, 2012.

[17] J.-W. van Wingerden and G. van der Veen, "Floating wind turbine control," Delft University of Technology, Delft, Tech. Rep., 2022.

[18] F. Meng, W. H. Lio, A. Pegalajar-Jurado, F. Pierella, E. N. Hofschulte, A. G. Santaya, and H. Bredmose, “Experimental study of floating wind turbine control on a Tetra-sub floater with tower velocity feedback gain,” *Renewable Energy*, 1 2023. [Online]. Available: https://linkinghub.elsevier.com/retrieve/pii/S0960148123000824

[19] M. A. Lackner and M. A. Rotea, “Structural control of floating wind turbines,” *Mechatronics*, vol. 21, no. 4, pp. 704–719, 2011.

[20] H. Haslum, M. Marley, S. T. Navalkar, B. Skaare, N. Maljaars, and H. S. Andersen, “Roll–Yaw Lock: Aerodynamic Motion Instabilities of Floating Offshore Wind Turbines,” *Journal of Offshore Mechanics and Arctic Engineering*, vol. 144, no. 4, 8 2022.

[21] L. Y. Pao and K. E. Johnson, “Control of Wind Turbines: Approaches, challenges, and recent developments,” *IEEE Control Systems*, vol. 31, no. 2, pp. 44–62, 2011.

[22] J. M. Maciejowski, *Predictive Control with Constraints*, 1st ed. Pearson College Div, 2001.

[23] F. Sandner, “Reduced Model Design of a Floating Wind Turbine,” *Master Thesis, University of Stuttgart*, 7 2012.

[24] M. Soliman, O. P. Malik, and D. T. Westwick, “Multiple model multiple-input multiple-output predictive control for variable speed variable pitch wind energy conversion systems,” *IET Renewable Power Generation*, vol. 5, no. 2, pp. 124–136, 3 2011.

[25] L. Pustina, F. Biral, and J. Serafini, “A novel Nonlinear Model Predictive Controller for Power Maximization on Floating Offshore Wind Turbines,” *Journal of Physics: Conference Series*, vol. 2265, no. 4, p. 042002, 5 2022. [Online]. Available: https://iopscience.iop.org/article/10.1088/1742-6596/2265/4/042002

[26] M. A. Evans and W. H. Lio, “Computationally efficient model predictive control of complex wind turbine models,” *Wind Energy*, vol. 25, no. 4, pp. 735–746, 4 2022.

[27] F. L. Sandner, “Low-Order Modeling, Controller Design and Optimization of Floating Oshore Wind Turbines,” *PhD Thesis, University of Stuttgart*, 7 2018.

[28] Wai Hou Lio, J. Rossiter, and B. L. Jones, “A review on applications of model predictive control to wind turbines,” in *UKACC International Conference on Control (CONTROL) : Proceedings : 9th-11th July 2014 : Loughborough, U.K.*, 2014, pp. 673–678.

[29] D. Schlipf, P. Grau, S. Raach, R. Duraiski, J. Trierweiler, and P. W Cheng, “Comparison of Linear and Nonlinear Model Predictive Control of Wind Turbines Using LiDAR,” *2014 American Control Conference (ACC)*, pp. 3742–3747, 2014.

[30] D. Schlipf, F. Sandner, S. Raach, D. Matha, and P. W. Cheng, *Nonlinear Model Predictive Control of Floating Wind Turbines.* International Society of Offshore and Polar Engineers, 2013.

[31] S. Raach, D. Schlipf, F. Sandner, D. Matha, P. W. Cheng, S. Raach, D. Schlipf, F. Sandner, D. Matha, and P. W. Cheng, "Nonlinear Model Predictive Control of Floating Wind Turbines with Individual Pitch Control," in *Proceedings of the American Control Conference, Portland, USA*, 2014.

[32] S. Christiansen, S. M. Tabatabaeipour, T. Bak, and T. Knudsen, "Wave disturbance reduction of a floating wind turbine using a reference model-based predictive control," in *American Control Conference (ACC).* Washington, DC, USA: IEEE, 6 2013, pp. 2214–2219.

[33] R. Chaaban and C.-P. Fritzen, "Reducing blade fatigue and damping platform motions of floating wind turbines using model predictive control," in *Proceedings of the 9th International Conference on Structural Dynamics, EURODYN 2014*, A. Cunha, E. Caetano, P. Ribeiro, and G. Müller, Eds., Porto, Portugal, 2014, pp. 3581–3588.

[34] Y. Okada, K. Haneda, T. Chujo, and T. Ohtsuka, "Parameter-varying modeling and nonlinear model predictive control for floating offshore wind turbines," in *IFAC-PapersOnLine*, vol. 52, no. 16. Elsevier B.V., 9 2019, pp. 382–387.

[35] F. Lemmer, S. Raach, D. Schlipf, and W. Cheng, "PROSPECTS OF LINEAR MODEL PREDICTIVE CONTROL ON A 10 MW FLOATING WIND TURBINE," in *ASME 2015 34th International Conference on Ocean, Offshore and Arctic Engineering*, 2015.

[36] C. Gallego-Castillo, V. A. Riziotis, A. Cuerva, D. I. Manolas, and O. Lopez, "Model Predictive Control for Floating Offshore Wind Turbines. What do we need to know about the future wind," *The International Conference on Wind Energy Harvesting*, 3 2018.

[37] K. A. Shah, Y. Li, R. Nagamune, Y. Zhou, and W. Ur Rehman, "Platform motion minimization using model predictive control of a floating offshore wind turbine," *Theoretical and Applied Mechanics Letters*, vol. 11, no. 5, 7 2021.

[38] T. Wakui, A. Nagamura, and R. Yokoyama, "Stabilization of power output and platform motion of a floating offshore wind turbine-generator system using model predictive control based on previewed disturbances," *Renewable Energy*, vol. 173, pp. 105–127, 8 2021.

[39] G. Betti, M. Farina, G. A. Guagliardi, A. Marzorati, and R. Scattolini, "Development of a Control-Oriented Model of Floating Wind Turbines," in *IEEE Transactions on Control Systems Technology*, vol. 22, no. 1, 1 2014, pp. 69–82.

[40] “HAWC2 Aeroelastic Simulation Of Wind Turbines -.” [Online]. Available: https://www.hawc2.dk/

[41] “OpenFAST · GitHub.” [Online]. Available: https://github.com/OpenFAST

[42] Q. Hawari, T. Kim, C. Ward, and J. Fleming, “LQG control for hydrodynamic compensation on large floating wind turbines,” *Renewable Energy*, vol. 205, pp. 1–9, 3 2023.

[43] A. Ramirez, A. Mehrizi-Sani, D. Hussein, M. Matar, M. Abdel-Rahman, J. Jesus Chavez, A. Davoudi, and S. Kamalasadan, “Application of balanced realizations for model-order reduction of dynamic power system equivalents,” *IEEE Transactions on Power Delivery*, vol. 31, no. 5, pp. 2304–2312, 10 2016.

[44] I. B. Sønderby, “Low-order aeroelastic models of wind turbines for controller design,” Technical University of Denmark, Kongens Lyngby, Tech. Rep., 2013.

[45] L. C. Henriksen, N. K. Poulsen, and M. H. Hansen, “Model Predictive Control of Wind Turbines,” DTU, Lyngby, Tech. Rep., 2011. [Online]. Available: www.imm.dtu.dk

[46] G. Betti, M. Farina, A. Marzorati, and R. Scattolini, “Modeling and Control of a Floating Wind Turbine with Spar Buoy Platform,” in *2nd IEEE ENERGYCON Conference and Exhibition, 2012 / Advances in Energy Conversion Symp.* IEEE, 2012.

[47] M. Karimirad and T. Moan, “A simplified method for coupled analysis of floating offshore wind turbines,” *Marine Structures*, vol. 27, no. 1, pp. 45–63, 7 2012.

[48] A. R. Henderson and M. H. Patel, “On the modelling of a floating offshore wind turbine,” *Wind Energy*, vol. 6, no. 1, pp. 53–86, 2003.

[49] J. M. Jonkman and P. D. Sclavounos, “Development of Fully Coupled Aeroelastic and Hydrodynamic Models for Offshore Wind Turbines,” in *2006 ASME Wind Energy Symposium, Reno, Nevada*, Reno, Nevada, 1 2006. [Online]. Available: http://www.osti.gov/bridge

[50] J. M. Jonkman, “Dynamics Modeling and Loads Analysis of an Offshore Floating Wind Turbine,” *PhD Thesis, National Renewable Energy Laboratory*, 11 2007. [Online]. Available: http://www.osti.gov/bridge

[51] ——, “Dynamics of offshore floating wind turbines-model development and verification,” *Wind Energy*, vol. 12, no. 5, pp. 459–492, 2009.

[52] R. Lupton, “Frequency-domain modelling of floating wind turbines,” Cambridge University, Cambridge, Tech. Rep., 2014.

[53] E. E. Bachynski, “Design and Dynamic Analysis of Tension Leg Platform Wind Turbines,” Ph.D. dissertation, Norwegian University of Science and Technology, Trondheim, 2014.

[54] A. Pegalajar-Jurado, M. Borg, and H. Bredmose, “An efficient frequency-domain model for quick load analysis of floating offshore wind turbines,” *Wind Energy Science*, vol. 3, no. 2, pp. 693–712, 2018.

[55] J. R. Homer, “Physics-Based Control-Oriented Modelling for Floating Offshore Wind Turbines,” University of British Columbia, Vancouver, Tech. Rep., 2015.

[56] A. Fontanella, I. Bayati, and M. Belloli, “Linear coupled model for floating wind turbine control,” *Wind Engineering*, vol. 42, no. 2, pp. 115–127, 4 2018.

[57] J. R. Homer and R. Nagamune, “Control-Oriented Physics-Based Models for Floating Offshore Wind Turbines,” in *American Control Conference*, Chicago, 2015, pp. 3696–3701.

[58] P. Veers, C. L. Bottasso, L. Manuel, J. Naughton, L. Pao, J. Paquette, A. Robertson, M. Robinson, S. Ananthan, A. Barlas, A. Bianchini, H. Bredmose, S. G. Horcas, J. Keller, H. A. Madsen, J. Manwell, P. Moriarty, S. Nolet, and J. Rinker, “Grand Challenges in the Design, Manufacture, and Operation of Future Wind Turbine Systems,” *Wind Energy Science*, 2022. [Online]. Available: https://doi.org/10.5194/wes-2022-32

[59] T. J. Larsen and A. M. Hansen, “How 2 HAWC2, the user’s manual,” Risoe National Laboratory, Technical University of Denmark, Roskilde, Denmark, Tech. Rep., 5 2023.

[60] C. Grinderslev, S. González Horcas, and N. N. Sørensen, “Fluid–structure interaction simulations of a wind turbine rotor in complex flows, validated through field experiments,” *Wind Energy*, vol. 24, no. 12, pp. 1426–1442, 12 2021.

[61] J. A. Michelsen, “Basis 3D-a Platform for Development of Multiblock PDE Solvers-release,” Technical University of Denmark, Tech. Rep., 1992.

[62] ——, “Block structured multigrid solution of 2d and 3d elliptic pde’s,” Technical University of Denmark, Tech. Rep., 1994.

[63] N. N. Sørensen, “General purpose flow solver applied to flow over hills,” Risoe National laboratory, Roskilde, Tech. Rep., 1995.

[64] DTU, “EllipSys.”

[65] M. K. Al-Solihat and M. Nahon, “Flexible multibody dynamic modeling of a floating wind turbine,” *International Journal of Mechanical Sciences*, vol. 142-143, pp. 518–529, 7 2018.

[66] J. Zhang, “Control design and validation for floating wind turbines,” DTU Wind Energy Department, Roskilde, Tech. Rep., 2021. [Online]. Available: www.vindenergi.dtu.dk

[67] J. M. J. Journée and W. W. Massie, *Offshore Hydromechanics*, 1st ed. Delft: Delft University of Technology, 2001.

[68] E. Gaertner, J. Rinker, L. Sethuraman, F. Zahle, B. Anderson, G. Barter, N. Abbas, F. Meng, P. Bortolotti, W. Skrzypinski, G. Scott, R. Feil, H. Bredmose, K. Dykes, M. Shields, C. Allen, and A. Viselli, “Definition of the IEA Wind 15-Megawatt Offshore Reference Wind Turbine Technical Report,” IEA Wind, Tech. Rep., 2020. [Online]. Available: www.nrel.gov/publications.

[69] A. Campos, C. Molins, X. Gironella, and P. Trubat, “Spar concrete monolithic design for offshore wind turbines,” *Proceedings of the Institution of Civil Engineers: Maritime Engineering*, vol. 169, no. 2, pp. 49–63, 6 2016.

[70] M. Y. Mahfouz, M. Salari, S. Hernández, F. Vigara, C. Molins, P. Trubat, H. Bredmose, and A. Pegalajar-Jurado, “Public design and FAST models of the two 15MW floater-turbine concepts,” corewind, Tech. Rep., 2020. [Online]. Available: https://zenodo.org/record/4385727#.Y_jK6ybMIuU

[71] M. Youssef Mahfouz, C. Molins, P. Trubat, S. Hernández, F. Vigara, A. Pegalajar-Jurado, H. Bredmose, and M. Salari, “Response of the IEA Wind 15 MW-WindCrete and Activefloat floating wind turbines to wind and second-order waves,” *Wind Energy Science Discussions*, 2021. [Online]. Available: https://doi.org/10.5194/wes-2021-11

[72] IEAWindTask37, “IEA-15-240-RWT: 15MW reference wind turbine repository developed in conjunction with IEA Wind.” [Online]. Available: https://github.com/IEAWindTask37/IEA-15-240-RWT

[73] G. van der Veen, “Identification of wind energy systems,” Ph.D. dissertation, Technische Universiteit Delft, Delft, 2013.

[74] J. A. Frederik, B. M. Doekemeijer, S. P. Mulders, and J. W. van Wingerden, “The helix approach: Using dynamic individual pitch control to enhance wake mixing in wind farms,” *Wind Energy*, vol. 23, no. 8, pp. 1739–1751, 8 2020.

[75] K. Shaler, J. Jonkman, G. E. Barter, J. J. Kreeft, and J. P. Muller, “Loads assessment of a fixed-bottom offshore wind farm with wake steering,” *Wind Energy*, vol. 25, no. 9, pp. 1530–1554, 9 2022.

[76] B. Fischer and M. Shan, “A survey on control methods for the mitigation of tower loads,” Fraunhofer-Institute for Wind Energy and Energy Systems Technology. IWES, Tech. Rep., 9 2013. [Online]. Available: https://www.researchgate.net/publication/324247930

[77] F. Meng, W. H. Lio, and T. Barlas, “DTUWEC: An open-source DTU Wind Energy Controller with advanced industrial features,” in *Journal of Physics: Conference Series*, vol. 1618, no. 2. IOP Publishing Ltd, 9 2020.

[78] M. H. Hansen and L. C. Henriksen, “Basic DTU Wind Energy controller,” DTU Wind Energy Department, Roskilde, Tech. Rep., 2013.

[79] T. Kailath, A. H. Sayed, and B. Hassibi, *Linear estimation*, 2000.

[80] A. Jain, G. Schildbach, L. Fagiano, and M. Morari, “On the design and tuning of linear model predictive control for wind turbines,” *Renewable Energy*, vol. 80, pp. 664–673, 8 2015.

[81] P. F. Odgaard, L. F. Larsen, R. Wisniewski, and T. G. Hovgaard, “On using Pareto optimality to tune a linear model predictive controller for wind turbines,” *Renewable Energy*, vol. 87, pp. 884–891, 3 2016.

[82] J. G. Leishman, “Challenges in modeling the unsteady aerodynamics of wind turbines,” in *ASME 2002 Wind Energy Symposium, WIND2002*, 2002, pp. 141–167.

[83] M. Hansen, M. Gaunaa, and H. Aagaard Madsen, “A Beddoes-Leishman type dynamic stall model in state-space and indicial formulations,” Forskningscenter Risoe, Denmark, Tech. Rep., 2023.

[84] E. L. Petersen, N. G. Mortensen, L. Landberg, J. Højstrup, and H. P. Frank, “Wind power meteorology. Part I: climate and turbulence,” *Wind Energy*, vol. 1, no. 1, pp. 2–22, 9 1998.

[85] ——, “Wind power meteorology. Part II: siting and models,” *Wind Energy*, vol. 1, no. 2, pp. 55–72, 12 1998.